

**Dissertation**  
**submitted to the**  
**Combined Faculties for the Natural Sciences and for Mathematics**  
**of the Ruperto-Carola University of Heidelberg, Germany**  
**for the degree of**  
**Doctor of Natural Sciences**

Put forward by

**Lic. Física :**                    **Andrés Camilo Vásquez Torres**  
**born in:**                        **Valdivia, Chile**

**Oral examination: 23rd November 2011**



**Development of a breathing phantom for  
comparison of two breathing surrogates  
systems in 4DCT-imaging**

Referees: Prof. Dr. Uwe Oelfke  
Prof. Dr. Christian Karger



## Zusammenfassung

Die vierdimensionale Computertomographie (4D-CT) benötigt ein Monitorsignal für die Atmung. Verschiedene Systeme sind zur Zeit verfügbar, aber um diese Systeme unter realistischen Bedingungen zu testen, ist ein Phantom mit einem beweglichen Zielobjekt und einer verformbaren äußeren Kontur erforderlich. Ein anthropomorphes Phantom wurde entwickelt und getestet. Die Atmungsbewegung eines Probanden wurde zusammen mit einer synchronen und asynchronen Bewegungen eines Lungentumors reproduziert. Das Phantom besteht aus Gewebe-äquivalenten Materialien und ist daher auch für dosimetrische Studien einsetzbar. Mit Hilfe des Phantoms wurden ein optische Kamera-Systeme (GateCT, VisionRT Ltd.) und ein Atemgürtel mit einem Drucksensor (AZ-733V, Anzai Medical Co. Ltd) getestet und 4D-CTs (Somatom Sensation Open, Siemens AG) mit beiden Atmungssignalen rekonstruiert. Ein Vergleich beider rekonstruierten Tumortrajektorien zeigte signifikante Unterschiede. Diese konnten nicht durch sichtbare Unterschiede in den Atemkurven, wie zB. Baseline-drift, unterschiedliche Zeitauflösung oder größeres Rauschen, erklärt werden. Stattdessen wurde gezeigt, dass die unterschiedlichen Trajektorien von der Variabilität der Abtastintervalle und der Genauigkeit der Abtastfrequenz in der Datei der Atemkurve verursacht wurden. Wenn man die Atemkurve auf ein reguläres Abtastintervall interpoliert und die Abtastfrequenz auf einen genauen Wert setzt, stimmen die rekonstruierten Trajektorien für beide Monitorsysteme überein. Ein Vergleich mit der vorgegebenen Trajektorie ergab für die verwendete CT-Schichtdicke von 3 mm eine residuale Unsicherheit von maximal 3 mm. Diese Unsicherheit muss bei der Definition des Zielvolumens berücksichtigt werden. Die Untersuchungsergebnisse heben die Wichtigkeit der Überprüfung neuer klinischen Geräte hervor, besonders wenn sie zusammen mit Geräten anderer Hersteller betrieben werden. Mit dem neu entwickelten Phantom können klinische Workflows getestet und die Funktionsfähigkeit der verwendeten medizinischen Geräte sichergestellt werden.

## Summary

Four-dimensional Computed Tomography (4D-CT) requires a surrogate breathing signal. Several surrogate systems are available, but for a realistic testing of these systems, a phantom with a moving target and a deformable outer contour is required. An anthropomorphic phantom was developed and tested to simulate patient breathing as well as the synchronous or asynchronous movement of a lung tumour. The phantom consists of tissue-equivalent materials and can be also used for dosimetric measurements. Using the phantom, an optical camera system (GateCT, VisionRT Ltd) and a belt with an integrated pressure sensor (AZ-733V, Anzai) were simultaneously operated and 4D-CTs (Somatom Sensation Open, Siemens AG) were reconstructed from both breathing curves. Comparison of the reconstructed tumour trajectories revealed significant differences. Visible differences in the breathing curves such as baseline shifts, a lower temporal resolution and an increased noise level were found in one of the signals, however, it was shown that these factors were not the reason for the observed differences. Subsequent experiments demonstrated that the differences were caused by the variability of the sampling interval and the accuracy of the sampling rate value in the file of the breathing curve. Interpolation to regular sampling intervals and correction of the sampling rate in the header to the actual value removed the differences encountered. For the used CT-slice thickness of 3 mm, a comparison with the predefined trajectory revealed a residual uncertainty of up to 3 mm. This uncertainty has to be considered in the definition of the target volume. The results of this study underline the importance of testing new equipment thoroughly, especially if components of different manufacturers are combined. Using the newly developed phantom, clinical workflows can be tested and the functioning of the applied medical devices can be ensured.



# Table of contents

<b>1. Introduction</b>	<b>1</b>
1.1. Radiotherapy and imaging .....	1
1.2. Human breathing motion .....	3
1.3. Breathing compensation techniques .....	5
1.4. Fundamentals of computed tomography .....	6
1.4.1. Physical principle .....	7
1.4.2. 2D image reconstruction .....	9
1.4.3. Image visualization .....	10
1.4.4. Scan modes, parameters and 3D reconstruction .....	12
1.4.5. Time-resolved computed tomography .....	13
1.5. Thesis objective and structure .....	17
<b>2. External breathing monitoring systems</b> .....	<b>18</b>
2.1. AZ-733V .....	19
2.2. GateCT .....	22
2.3. Breathing data files format .....	28
2.4. Comparison of breathing monitor systems .....	30
2.4.1. Materials and methods .....	31
2.4.2. Results .....	32
<b>3. Breathing phantom development</b> .....	<b>34</b>
3.1. Design and construction .....	35
3.2. Breathing motion .....	38
3.3. Motion-Control Software .....	39
3.4. Dosimetry in the phantom .....	42
3.5. Imitating human breathing .....	43
3.5.1. Materials and methods .....	43
3.5.2. Results .....	44
<b>4. Generating 4D-CT images</b> .....	<b>46</b>
4.1. Materials and methods .....	46
4.1.1. Including the EBMS signal .....	46
4.1.2. Testing GateCT .....	47
4.1.3. Comparison of monitor signals .....	48

4.1.4.	Evaluation of sampling intervals and rates .....	50
4.1.5.	Influence of CT-couch movement on GateCT signal .....	51
4.1.6.	Comparison of 4D-CT reconstructions .....	52
4.1.6.1.	Analysis of tumour trajectory .....	52
4.1.6.2.	Modification of breathing signals' parameters .....	54
4.2.	Results .....	57
4.2.1.	Testing GateCT .....	57
4.2.2.	Comparison of monitor signals .....	58
4.2.3.	Evaluation of sampling intervals and rates .....	62
4.2.4.	Influence of CT-couch movement on GateCT signal .....	64
4.2.5.	Comparison of 4D-CT reconstructions .....	65
4.2.5.1.	Analysis of tumour trajectory .....	65
4.2.5.2.	Modification of breathing signals' parameters .....	66
<b>5.</b>	<b>Discussion .....</b>	<b>73</b>
5.1.	Comparison of external breathing monitoring systems .....	73
5.2.	Phantom capabilities .....	73
5.3.	Testing GateCT for use in 4D-CT imaging .....	74
5.4.	Comparison of 4D-CT reconstructions .....	74
5.5.	Clinical implications .....	77
<b>6.</b>	<b>Concluding remarks .....</b>	<b>79</b>
6.1.	Summary .....	79
6.2.	Outlook .....	79
6.2.1.	Gating a linear accelerator .....	80
6.2.2.	Study of external breathing monitoring systems and tumour motion correlation in patients .....	80
	<b>Bibliography .....</b>	<b>81</b>
	<b>Figure index .....</b>	<b>86</b>
	<b>Table index .....</b>	<b>88</b>
	<b>Acknowledgements .....</b>	<b>89</b>

## Introduction

### 1.1 Radiotherapy and Imaging

Cancer is the major cause of death in the world. Among all the different cancer types, lung and breast cancers had the highest incidence in 2008 in males and females, respectively (figure 1.1). It is expected that this number will continue being high (or growing even higher) as cancer affect largely the elderly. Population will get older in the next years as life expectancy rises and total fertility rate decreases worldwide (figure 1.2).

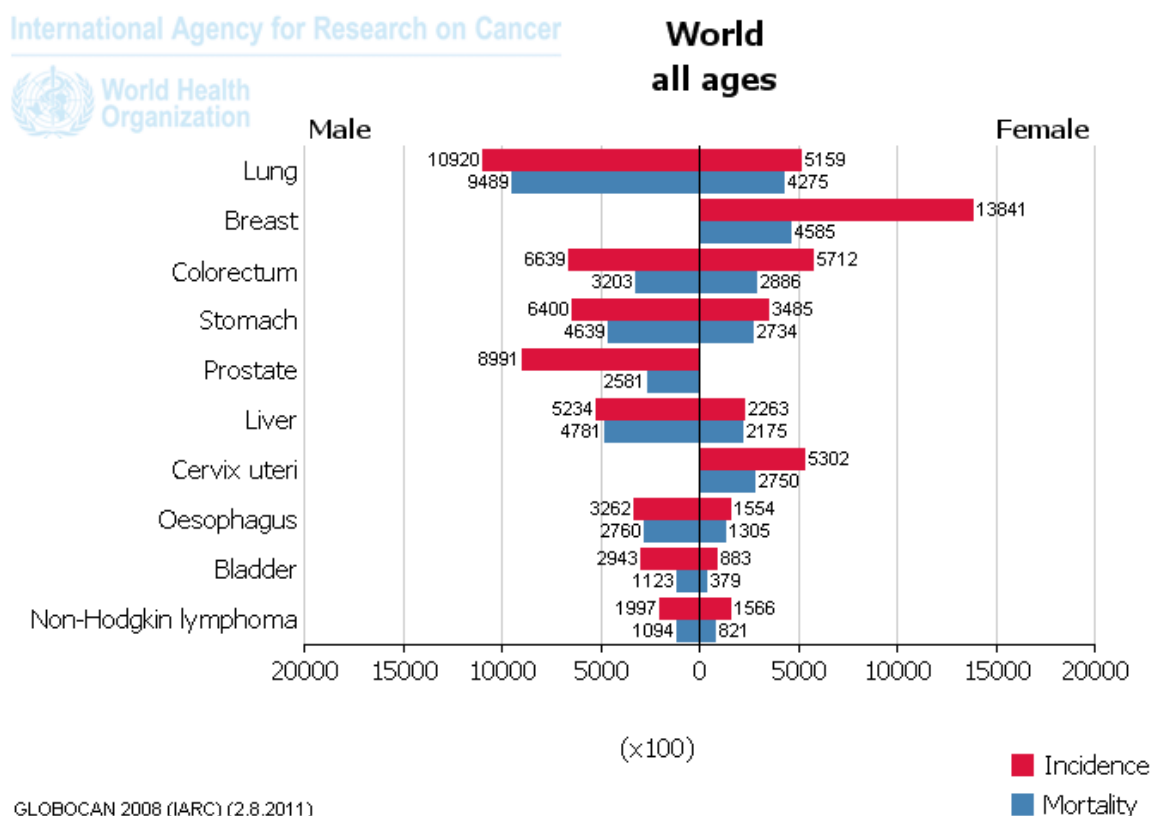


**Figure 1.1:** Incidence and mortality for both sexes worldwide. From Ferlay *et al.* GLOBOCAN 2008.

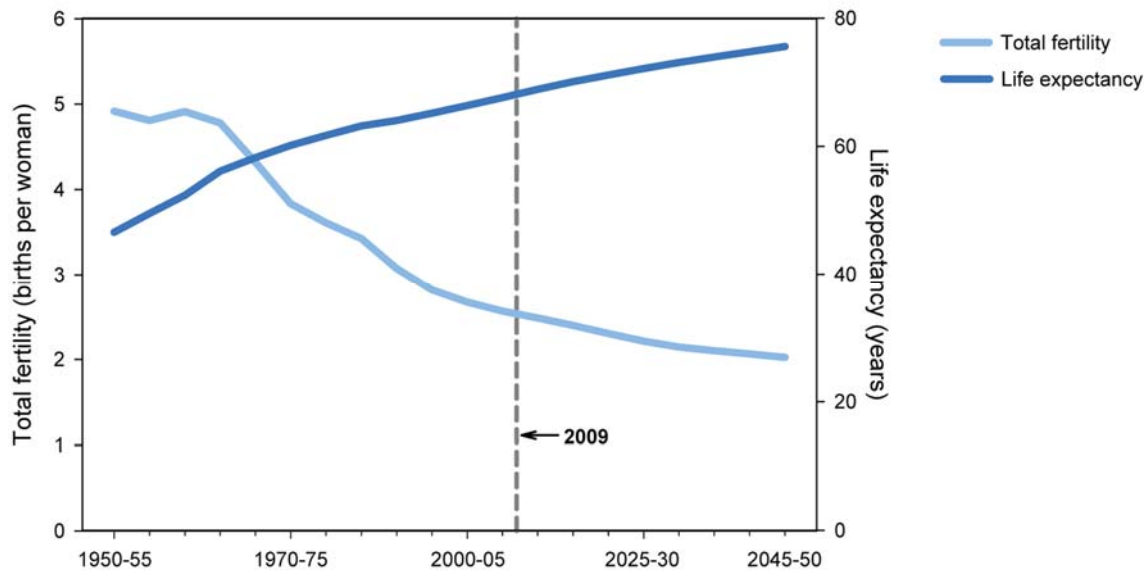


**Figure 1.2:** Worldwide total fertility rate and life expectancy at birth from year 1950-2050 (expected). From “World Population Ageing 2009”, United Nations (2010)

Cancer treatment can be separated in three main branches: Surgery, Chemotherapy and Radiotherapy. Being the second most effective technique, radiotherapy consists in the use of radiation to kill cancerous cells and it is often used in non operable tumours. Normally, the tumours are surrounded by healthy tissue and other organs. As radiation affects all cells without distinction, the delivery of radiation has to be performed with great care to lessen treatment toxicity or in other words to reduce the normal tissue complication probability (NTCP).

Tumour targeting incorporates margins around the tumour to ensure that the therapeutic beam always hits the target. This improves local tumour control, but also elevates the NTCP. Since its invention, Intensity Modulated Radiation Therapy (IMRT) has provided a better sparing of the healthy tissue without compromising local tumour control. IMRT though, requires suitable knowledge of the patient’s anatomy for treatment planning. X-Ray computed imaging (CT) imaging provides high resolution images of the patient anatomy and allows spatial detection of the tumour as well as its location relative to healthy tissues. The problem is that tumours located at the thorax (specifically lung and breast) change their locations due to breathing, making the targeting of the tumour more difficult and adding uncertainties to the treatment.

## 1.2 Human breathing motion

Breathing can be resumed as the process involved in the exchange of gases, more specifically oxygen ( $O_2$ ) and carbon dioxide ( $CO_2$ ) that takes place in the lungs. The inhaled air (containing about 20%  $O_2$ ) flows through the nose or mouth into by the pharynx, larynx and the trachea. Then the air continues to the bronchi, bronchioles, to finally arrive at the alveoli, which are embedded with capillaries. As the size of the structures gets smaller, the surface area covered by the capillaries gets larger, facilitating the diffusion of  $O_2$  and  $CO_2$  from the air into the blood and vice versa, respectively.

The lungs are surrounded by a membrane called pleural sac, which is filled with intrapleural fluid (figure 1.3). The outer lung wall is connected with the inside membrane of the pleural sac. At the same time the outer membrane of this sac is connected with the thoracic wall. When exhaling, the membranes are separated from each other and the pressure inside the pleural sac decreases proportionally to the lung pressure, producing a force that keeps the lungs from collapsing.

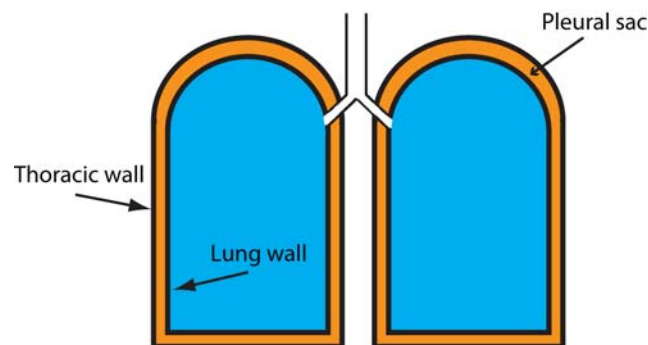


**Figure 1.3:** The pleural sac in-between the lungs and thoracic walls

The expansion and contraction of the lungs is the result of the action of several muscles. In normal breathing only the expansion is an active process. To initiate inhalation, the diaphragm travels downward pulling the bottom of the lungs, while the intercostals muscles elevate the ribs. Both movements result in an increase of chest cavity volume, a decrease of the internal pressure and the drawing of air into the lungs. Exhalation on the contrary is a passive process caused by the natural recoil of the lungs, the elasticity of the chest wall and the relaxation of the muscles. Only during heavy breathing does this process require muscle contraction.

The amount of air in the lungs and the rhythm of the breathing cycle can be controlled consciously (to a certain limit), however most of the time it is an unconscious process regulated through chemoreceptors and depends on the amount of oxygen, carbon dioxide and the arterial blood pH.

As shown by many studies, the breathing periodicity, amplitude and base line of patients can vary during a single imaging or treatment session (Vedam et al. 2003; George et al. 2005). Lung tumours can even present hysteresis in their trajectories (Seppenwoolde et al. 2002), making them more difficult to locate with precision (figure 1.4).

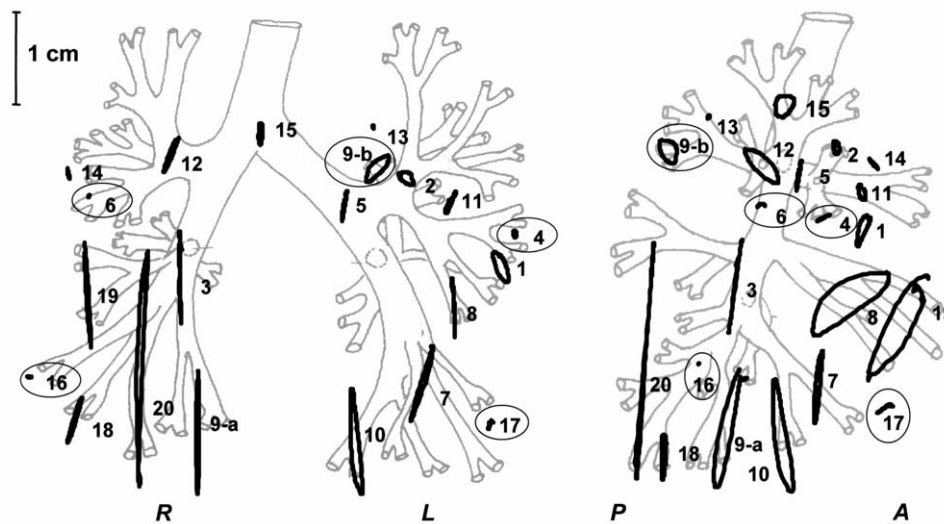


**Figure 1.4:** Projection of lung tumour trajectories measured with fluoroscopic images. E.g., tumour nr. 20 had a mean motion of  $24.6 \pm 3.8$  mm. Some trajectories show hysteresis during a complete breathing cycle From Seppenwoolde *et al.* (2002).

There have been models to predict breathing motion, but they are population based and are not exempt of error. As summarised by the AAPM task group 76 (Paul J. Keall et al. 2006): “A review of the respiratory motion literature leads to the following conclusion: There are no general patterns of respiratory behaviour that can be assumed for a particular patient prior to observation and treatment”.

Bortfeld et al 2004 studied the impact of breathing motion on radiotherapy. A blurring of the accumulated dose was found in their work. Under those circumstances, to ensure proper treatment delivery, a personalised study of patient breathing motion and its impact in the dose delivery has to be performed.

## 1.3 Breathing compensation techniques

Different methods exist to take into account the effects of breathing motion. For example in imaging, slow CT scanning (Lagerwaard et al. 2001), inhalation/exhalation breath-hold CT (Berson et al. 2004) and time-resolved-CT have been used (Ford et al. 2003).

In slow CT scanning, the average tumour and organ locations are obtained. The images provide the whole range of movement and the target delineation can be done accordingly, but averaging also produces blurring, affecting image quality.

Inhalation/exhalation breath-hold CT eliminates the blur and provides a sharper view of the thorax, but only represents a single state of the breathing cycle and requires an effort for voluntary control of the breathing, which may not be achievable by all patients. Also the tumour location during treatment may differ, if the treatment is performed during free breathing.

Another approach is prospective gating of the CT-Scanner, where the imaging beam will be turned on only when the respiratory movement meets certain criteria (e.g., in the end-inspiratory or -expiratory breathing phase). The additional information is provided by an external breathing monitoring system (see chapter 2). This technique allows patient free breathing, but additional time is required to gather enough CT information.

Time resolved-CT (sometimes respiration-correlated CT or 4D-CT) takes into account when a certain image was taken by using an external signal. This approach produces high quality images and has the advantage that tumour and organ movements can be observed during the whole breathing cycle. On the other hand, it depends heavily on the regularity and stability of the patient's respiration pattern. More details on this technique are given in subsection 1.4.5

Also for the case of radiation therapy there are techniques that take tumour motion explicitly into account. These are respiratory gating (using free breathing or breath-hold) and tumour tracking.

Respiratory gating (Kubo and Hill 1996; Ford et al. 2002) is similar to the prospective CT gating, where the breathing signal is provided by an external monitor system. When the signal enters a predetermined window, the therapeutic beam is turned on. The window is defined by two thresholds, which can be two amplitudes or two phases of the signal. Both breath-hold and free

breathing are possible with this technique (Korreman et al. 2005), but as expected treatment time delivery is extended. Breath-hold at the end-inspiratory phase is of special interest for breast cancer radiotherapy, due to the increment in distance between the target, the lungs, and heart, therefore diminishing the toxicity of the treatment (Sixel et al. 2001; Korreman et al. 2006).

Tumour tracking (Tacke et al. 2010; Bert et al. 2007), although technically more challenging, proposes to follow the tumour with the beam during treatment. To realise tumour tracking, complete information about the tumour trajectory is required during the whole treatment. Fluoroscopic images have been used to follow the tumour, but due to the low tumour contrast, usually metal implants are used as fiducial of the tumour movement (Murphy 2004). Implantable radiofrequency coils have also been used. Their advantage is that they are not associated with additional dose to the patient (Rau et al. 2008). Tracking can also be based on the movement of external breathing surrogates that do not need additional imaging dose or some sort of device implantation, but it requires special attention, due to changes in tumour-surrogate correlation (Hoisak et al. 2004), and for this motive they are usually combined with periodical X-ray imaging to check the stability of the correlation (Wong et al. 2007).

The following sections of this chapter will turn their focus on explaining imaging and imaging of moving anatomy.

## **1.4 Fundamentals of Computed Tomography**

As important as X-ray images has been in the past, X-ray computed tomography has played a major role in imaging diagnostic in the last decades. Since its practical implementation by G.N. Hounsfield in the seventies, the technique of this valuable tool has advanced with the years and nowadays, patients can be imaged within a few seconds, creating images with submillimetre resolution and for this reason CTs are used worldwide and in daily clinical routine. A historical review depicting the CT evolution can be found in ( Kalender 2006).

The physical principle behind the CT are briefly shown in sections 1.4.1, followed by an explanation of the reconstructions methods used to create the CT images in sections 1.4.2. The conventions and definitions for CT image visualization and the technical concepts behind CT

acquisitions are given briefly in section 1.4.3 and 1.4.4, respectively. Finally, section 1.4.5 will describe the technique called time-resolved computed tomography.

### 1.4.1 Physical principle

Since their discovery by W.C. Röntgen in 1895 X-rays have been used in medical devices due to their capability to provide information of the interior of objects, in this case patient's anatomy. Nowadays "hard" X-rays, produced with voltages ranging 80 to 140 kV, are used in CT imaging.

After travelling through an object, the intensity of X-rays is attenuated. If the object is homogenous, then the attenuation of the intensity  $I$  will depend on the value of the linear attenuation coefficient  $\mu$ , following the function

$$I(\mu) = I_0 e^{-\mu \cdot L} \tag{1.1}$$

where  $I_0$  is the original intensity of the X-ray beam and  $L$  the thickness of the object.

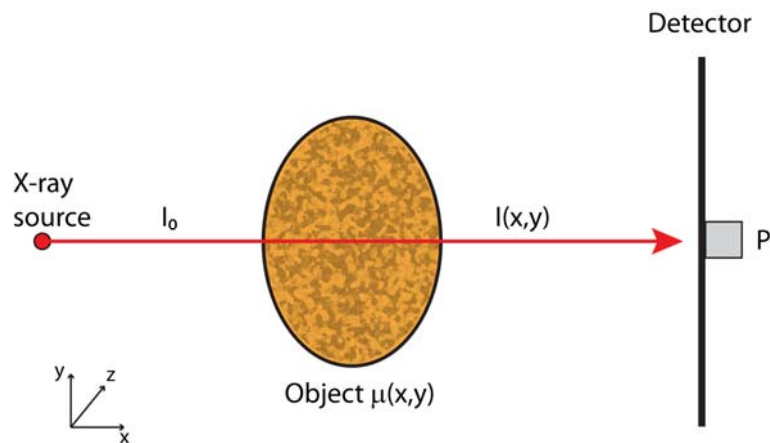


**Figure 1.5:** Projection value  $P$  produced by the X-ray beam intensity  $I$  is recorded at the detector and provides information of the attenuation values in the inhomogeneous object  $\mu$ .

On the other hand, if the object is inhomogeneous as in figure 1.5, then the intensity will depend on the different values of  $\mu$  along the along a line  $L$ . Therefore the intensity  $I$  of the beam after going through the object will be:

$$I(x, y) = I_0 e^{-\int \mu(x, y) dL} \quad (1.2)$$

At the CT detector, a projection function  $p$  can be defined as

$$p(L) = \ln\left(\frac{I_0}{I(L)}\right) = \int f(x, y) dL \quad (1.3)$$

making  $p(L)$  the integral of the CT values  $f(x, y)$  along a line  $L$ , where the CT image  $f(x, y)$  is an approximation to the true  $\mu(x, y)$  values. Now this process is similar to a normal X-ray image acquisition, where the final image is the sum of the attenuation values encountered in the object. The difference is that to produce a 3D image a tomographic principle is used. The CT adds new information by changing the orientation of the beam. Each new orientation  $\theta$  will provide different values for  $p$  (figure 1.6).

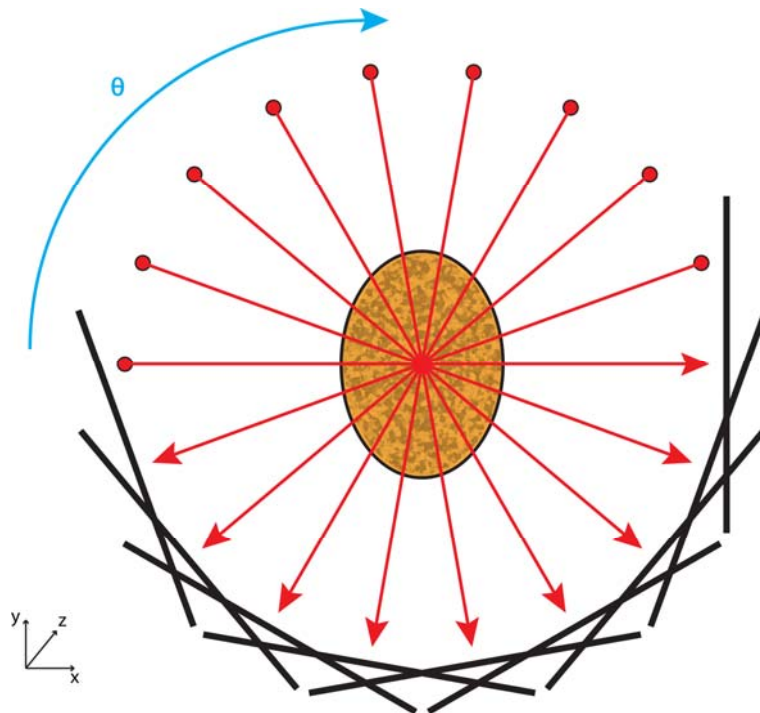


**Figure 1.6:** Each new orientation  $\theta$  adds new information about the object, which is later used in the image reconstruction process.

Now that we know the values of  $p$  received at the detector, we can ask the question of which values did the CT image  $f(x,y)$  have to have to produce such  $p$  value?

### 1.4.2 2D image reconstruction

To find this out, we can parameterise the line  $L$  as,

$$L : x \cos(\theta) + y \sin(\theta) = \rho \quad (1.4)$$

where  $\theta$  is the angle of the line with respect to abscissa-axis, and  $\rho$  the distance of line  $L$  to the origin. Then together with the Dirac's delta function  $\delta$ , we can rewrite equation 1.3 into

$$p(\theta, \rho) = \iint dx dy f(x, y) \delta(x \cos(\theta) + y \sin(\theta) - \rho) \quad (1.5)$$

Equation 1.5 can be interpreted as:  $p = Rf$ , where  $R$  is the Radon transform (Radon, 1917). If  $R^{-1}$  is found, then  $f$  can be "reconstructed" from  $p$ . We can start looking for  $R^{-1}$  by calculating the Fourier transform  $P$  of the function  $p$  with respect to  $\rho$ . This result in

$$P(\theta, \mathcal{G}) = \int d\rho p(\theta, \rho) e^{-2\pi i \mathcal{G} \rho} = \iint dx dy f(x, y) e^{-2\pi i \mathcal{G} (x \cos \theta + y \sin \theta)} \quad (1.6)$$

Now if we remember the 2-dimensional (2-D) Fourier transform  $F(u,v)$  of  $f(x,y)$ , namely

$$F(u, v) = \iint dx dy f(x, y) e^{-2\pi i (ux + vy)} \quad (1.7)$$

and if we use the change of variables

$$(u, v) = (\mathcal{G} \cos \theta, \mathcal{G} \sin \theta) \quad (1.8)$$

we can see from equation 1.7 and 1.6 that

$$F(\mathcal{G}\cos\theta, \mathcal{G}\sin\theta) = P(\theta, \mathcal{G}) \quad (1.9)$$

This is known as the Fourier slice theorem (Bracewell 1956) and means that the 2-D Fourier transform of the CT-image  $f(x,y)$  expressed in radial coordinates is equal to the Fourier transform of the projection function  $p(\theta, \rho)$  with respect to  $\rho$ . Now if we apply directly the inverse 2-D transform to equation 1.7 we obtain

$$f(x, y) = \iint dudv F(u, v) e^{2\pi i(ux+vy)} \quad (1.10)$$

Remembering the changes of variables 1.4, 1.8 and using equation 1.9, it finally results that the CT-image is

$$f(x, y) = \int_0^\pi d\theta \int_{-\infty}^\infty d\mathcal{G} |\mathcal{G}| P(\theta, \mathcal{G}) e^{2\pi i\mathcal{G}\rho} = \int_0^\pi d\theta k(\rho) * p(\theta, \rho) \quad (1.11)$$

a convolution of a reconstruction kernel  $k(\rho)$  with the projection data  $p(\theta, \rho)$ . The kernel acts as a filter for the projections values. Different reconstruction kernels are available to improve image sharpness, noise, etc. This algorithm is called filtered-back projection (FBP) and it is implemented in all CT-scanners. The name originates out of the fact that it projects the known (filtered) value  $p$  back into the image space. More information on the CT image reconstructions methods can be found elsewhere (Kalender 2005, p. 245).

### 1.4.3 Image visualization

The information obtained by the CT is visualised in terms of CT-values (sometimes CT-numbers). These values are expressed in Hounsfield Units (HU) (in honour to the inventor of the CT) and are defined as a linear function of the attenuation values or more exactly written

$$\text{CT value} = \frac{\mu - \mu_{water}}{\mu_{water}} \cdot 1000 \text{ HU} \quad (1.12)$$

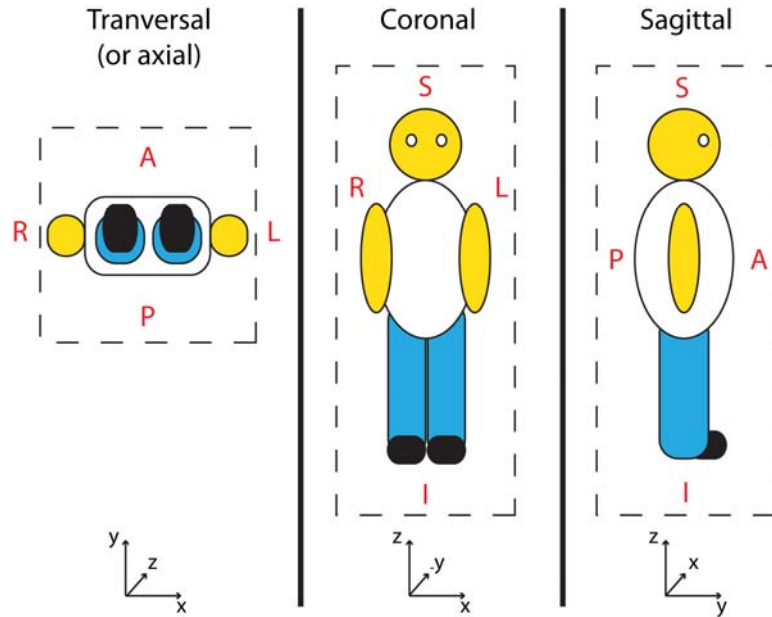


**Figure 1.7:** Visualization planes for the CT data. Directions are defined as anterior (A) – posterior (P), right (R) – left (L) and superior (S) – inferior (I). Transversal (or axial), Coronal and Sagittal orientations refer to the X/Y, Z/X and Z/Y planes, respectively.

Therefore any water-equivalent materials with  $\mu = \mu_{water}$  will have a CT number of 0 HU and air will have a CT number of -1000 HU (with:  $\mu_{air} \approx 0$ ). Lung tissue will have a CT-numbers ranging -500 to -1000 HU, soft tissue from -100 to 100 HU and bones will normally have values bigger than 200 HU. These values are displayed as grey-levels with a range from -1024 to 3071 HU. Due to the impossibility for the human eye to distinguish so many grey levels, a window of values is normally used. The window is defined by a centre value (C) and a width (W). Thus the range of the window will cover from  $C-W/2$  to  $C+W/2$  with values lower and higher displayed as black and white, respectively. Values in-between will be linearly mapped to grey-values ranging from black to white. Therefore different windows provide different tissue information. Table 1.1 shows two CT-number windows that will be used throughout this work.

**Table 1.1:** CT values for bone and lung windows in Hounsfield-Units (HU)

Window	Center (HU)	Width (HU)
Bone	40	400
Lung	-600	1200

CT reconstruction of a volume is done usually in axial slices, i.e., the whole scanned volume will consist of a stack of axial images. Coronal and sagittal orientations are also common for visualization and directions are defined as Anterior-Posterior (A-P), Right-Left (R-L) and Superior-Inferior (S-I) as seen in figure 1.7.

#### 1.4.4 Scan modes, parameters and 3D reconstruction

Normally a single rotation of the X-ray tube is not enough to cover the whole volume of interest (VOI), therefore this process must be repeated several times by moving the CT table (or couch) before each acquisition, until the whole VOI is covered. This technique is called step-and-shoot or sequential scanning and can be considered as the conventional scan mode in many facilities.

A faster mode to acquire CT-scan is with spiral scan. Here the X-ray tube will rotate continuously, whilst the couch moves with a steady velocity. From the patient's point of view, the X-ray tube will describe a spiral, hence the name of the technique. A-P movements are referred as Cranio-Caudal (C-C), when the patient's head enters the CT-bore before his/her feet.

Most of the CT parameters (Voltage, Tube current, slice collimation thickness, etc.) are the same for sequential and spiral scanning. Nevertheless the latter introduce a new one, the pitch or pitch value. The pitch value  $p$ ,

$$p = \frac{d}{M \cdot S} \quad (1.13)$$

is the ratio of  $d$  (the table movement within one CT full rotation) to the total slice collimation  $M \cdot S$  (with  $M$  the number of detector rows and  $S$  the slice collimation) and it is a dimensionless quantity. Small pitch values allow oversampling of data e.g., to reduce noise or motion artefacts, whereas bigger values allow faster scans.

The table movement can be written as  $d = v \cdot T_{rot}$ , where  $T_{rot}$  is the time required for one CT full rotation and  $v$  the table velocity. Therefore using equation 1.13, the table velocity can be described as

$$v = \frac{p \cdot M \cdot S}{T_{rot}} \quad (1.14)$$

Practical considerations determine the value of the couch velocity. Small velocities increase the dose to the patients, whereas high speeds can affect image quality.

Now returning to the reconstruction process, since the FBP algorithm requires 2-D geometry, additional steps are necessary to reconstruct spiral CTs. Virtual circles will be created from the spiral data through interpolation in the Z-direction and a normal FBP reconstruction can be applied to these virtual circles.

As CT scanner technology progressed, it was necessary to take the geometry of the X-ray beam into account in the reconstruction process. The first scanners (and up to 4 rows) could consider the beam as a collection of parallel rays. But to cover additional volume, modern scanners use cone beam geometry. Now that the X-rays were non-coplanar a different reconstruction progress was required. A 3-D FBP algorithm was developed by Feldkamp et al. (1984) to deal with the reconstruction under cone beam geometry, but it was quite time consuming. The Advanced Single-Slice algorithm from Kachelriess (a) et al. (2000) diminished the reconstruction times, by fitting a 180° segment of a circle to the spiral data. Then the cone beam data is resorted to this tilted circle and a standard 2-D reconstruction is performed on the tilted circle, creating tilted images. The final step requires resampling the tilted images into normal images in Cartesian coordinates.

#### 1.4.5 Time-resolved Computed Tomography

CT images are prone to distortions and artefacts, when movement is present (Balter et al 1996). Movements can be diminished with the cooperation of the patient, but internal organ motion or breathing can not be avoided. To deal with this issue, motion has to be directly considered in the reconstruction process. A technique called time-resolved CT or 4D-CT takes into account when a certain image was taken and together with an external signal it can improve image quality.

4D-CT was first implemented to improve the heart visualization in cardiac imaging (Kachelriess (b) et al. 2000) and was later extended to other anatomical areas. The idea behind 4D-CT consists of oversampling the data acquisition at a given couch position. This data is originated from the same

coordinates in space, but it differs in the temporal coordinate. For sequential scanning the oversampling can be made with the cine mode protocol, whereby the couch remains for a longer time than required at each couch position. For spiral CT the oversampling is controlled with a low pitch value.

Now the value of the pitch must be carefully selected to avoid 4D-CT undersampling, which is the situation where there is not enough information for each breathing cycle. When this happens, the CT images will contain anatomy gaps and/or image artefacts.

To avoid undersampling, the patient's respiration has to be considered on the CT-protocol. To ensure that each part of the patient's anatomy is scanned for a full breathing cycle ( $T_{cycle}$ ) meaning an inspiration and an exhalation, the CT-table velocity cannot be faster than

$$v \leq v_{Max} = \frac{M \cdot S}{T_{cycle}} \quad (1.15)$$

where  $M \cdot S$  is the total slice collimation, but also the distance covered in the Z-direction. Replacing the last equation into equation 1.14 results in

$$p \leq \frac{T_{rot}}{T_{cycle}} \quad (1.16)$$

showing that to avoid undersampling, the pitch for a given CT rotation time, must be selected accordingly to the patient's actual full breathing cycle.

Now for image reconstruction, each point of the volume of interest must be sampled at least by 2 rays separated by  $180^\circ$ . Taking in consideration the cone-beam geometry, this means that the X-ray tube located at angle  $\theta$  must turn another  $180^\circ$  plus beam angle. For a beam angle of  $60^\circ$  and considering that modern CTs can rotate their X-ray tube in 0.5 seconds, an image will integrate the projections taken in a time span of 333 ms. Therefore the temporal resolution of a 4D-CT scan depends on the CT rotation time and due to this limitation some residual motion may still persist, but it will be greatly reduced in comparison of not using the 4D-CT technique at all.

Now the oversampled data projections must be sorted to include the temporal component. This is done with help of an external signal, which registers when certain event happened (e.g. the lungs were fully inflated).

Let us say that such event was recorded at the times  $T[i]$ . The CT then searches for a projection  $P[t]$  that was acquired at a time  $t = T[0]$  and selects this projection and all the surrounding projections required to complete an image. Then again the same process is repeated, but for  $T[i + 1]$  and so on, until the whole volume is sorted under the event condition.

Repeating this procedure on the oversampled data every time such an event is detected will create different CT-volumes; each one with the special characteristic that it will only represent the volume at the chosen event.

Since external signals can be described by their phase or amplitude, an event can be labelled by one of these parameters. CT-projections selection (or sorting), have being made either by their phase (Ford et al. 2003; Vedam et al. 2003; Keall et al. 2004) or by their amplitude (Low et al. 2003; Wink et al. 2005; Lu et al. 2006). As CT-data must be available beforehand, the projections are sorted retrospectively (Guckenberger et al. 2007). The external signal is referred as surrogate signal and it has to correlate with the motion of the tumour.

Normally to take into account hysteresis of the tumour trajectory (figure 1.4) the surrogate signal is split up into an inspiration and an exhalation part (figure 1.8). CTs reconstructed at a specific event will not be directly named after the phase or amplitude chosen, but after to the percentage of the signal they represent (e.g. 70% inspiration, 50% exhalation, etc.).

Usually several CTs are obtained from the 4D-CT data. Each individual CT can be regarded as a “snapshot” of the anatomy at a given time point. The number of reconstructed CTs varies depending on local clinical protocols, but one main goal is to determine the tumour trajectory and to use this information for the definition of the target volume in treatment planning.

For this, the ICRU 62 report (1999) provides the following concept: A gross tumour volume (GTV) is delineated around the visible tumour. A margin is added to it to create the clinical target volume (CTV), which encompasses the GTV plus the suspected microscopic spread. Variations in the size and position of the CTV are taken into account in the internal target volume (ITV). Finally, the

planning target volume PTV includes all the previously mentioned volumes together with an additional margin for geometrical uncertainties in the treatment delivery. As breathing influences the volume of the ITV (and hence also that of the PTV), modern radiotherapy approaches aim to either determine the ITV accurately or even to reduce its volume by adaptive techniques using 4D-CTs.

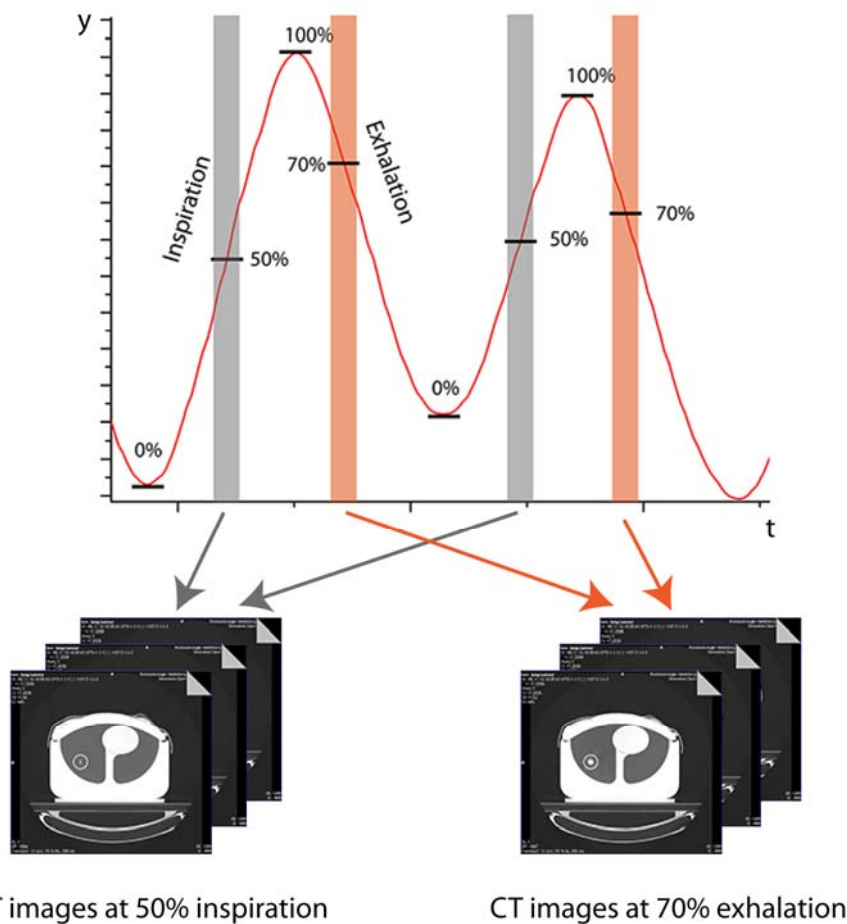


**Figure 1.8:** Image formation from oversampled data into several CT datasets sorted by a local amplitude algorithm. In this example, projections from the 50% inspiration amplitude are taken to form one 3D-CT set of images. The same is done for 70% exhalation.

For a safe clinical application of this technique, it is essential to know the uncertainty of the reconstructed tumour position in the 4D-CT. This uncertainty originates mainly from two sources: the uncertainty of the system under ideal correlation conditions (i.e. for a 100% correlation between the surrogate signal and tumour motion), and the additional uncertainty added, when this correlation is distorted.

## 1.5 Thesis objective and structure

The objective of this thesis was to develop a new phantom, necessary for testing new equipment for motion-compensated imaging and radiotherapy. As proof of principle the phantom was used to test two commercial external breathing monitoring systems used in 4D-CT imaging. This work also presents the troubleshooting encountered interfacing the investigated optical breathing monitor system with a Siemens CT-scanner.

Following this introduction, chapter 2 will start with a brief summary of the types of external breathing monitors used in imaging and radiation therapy, followed by a more detailed description of both system used in this study and the first comparison between them. Chapter 3 will present a short review of the phantoms used in previous publications together with the technical data and full description of the phantom features constructed for this work. Finally the phantom capabilities in imitating human breathing are tested. The first part of chapter 4 starts showing the methods and parameters used to compare the effect that the signals, obtained from the breathing monitoring systems, have in 4D-CT imaging. The final part of this chapter shows the incompatibilities found between the optical monitor system and the CT and how they were solved. Chapter 5 contains the discussion of the results obtained throughout this work. A short summary and suggestions for future work are given in chapter 6.

## *External breathing monitoring systems*

As mentioned in subsection (1.4.5) additional information for imaging is required to compensate tumour motion and motion related artefacts, especially in free-breathing conditions. The optimal situation would be to have information about each organ trajectory, but technology is far from achieving such a challenge. For the time being an acceptable approach is to obtain information about the thorax expansion or the abdominal motion due to respiration. By using an external breathing monitoring system (EBMS), a signal that represents the phase and amount of movement of a patient's breathing cycle can be obtained.

Several EBMSs have been proposed to be used in conjunction with imaging, which were first used in gated radiotherapy. Thermocouples positioned in front of the face of patients can be used to measure the temperature of the air inhaled (at room temperature) and exhaled (close to 36°C) (Wolthaus et al. 2005; Kubo and Hill 1996). Another approach is the use of a spirometer to measure the volume of air going in and out of the lungs (Low et al. 2003). In this case the patient must bite on a mouthpiece and a clip is fitted in the patient's nose to ensure that the air will only flow through the mouth. A more widely used device is the Real-Time Position Management system (RPM, Varian Medical Systems, Palo Alto, CA, USA). The RPM system consists of an infrared camera and a block with reflective markers. The block is positioned on the patient's abdomen and the camera tracks the marker as it moves with the patient respiration (Vedam et al. 2001).

Also strain gauges (Wink et al. 2005) around the patient's waist have been used as well as optical cameras, which track the patient's movement as they breathe (Glide-Hurst et al. 2011).

The two last types of EBMS are of great interest, as they are unnoticed by patients, providing a higher comfort. Examples for the last types are the AZ-733V and the GateCT systems, respectively. The first was chosen, because it is currently (at the time of writing) the gold standard at the

Radiological University Clinic of Heidelberg. The latter is a promising device and has interesting features that make it a suitable system for 4D-imaging and radiotherapy, worth investigating.

More detailed information of both systems will be given in sections 2.2 and 2.3. It will be shown that the recollected breathing information must be in compliance with a specific format dictated by the CT used in this study. This format will be explained in section 2.4. Finally section 2.5 will present and compare the data acquired with the two EBMSs from a healthy volunteer.

## 2.1 AZ-733V

The first system is the Respiration Gating System AZ-733V (Anzai Medical Co. Ltd, Tokyo, Japan). In our institution, this device is the current standard that provides the required respiration signal for 4D-CTs. Under this brand name two systems can be found in the literature, one that uses a laser to measure distance changes (Berbeco et al. 2005) and another that uses a pressure sensor. This study is focused only in the system using the pressure sensor.

The sensor consists of a pressure-cell, containing a piezoelectric material, which is placed inside a pocket of an elastic belt. The belt can be fastened around the waist and when the patient inhales, the elastic belt tightens and the sensor is compressed. As the patient exhales the pressure exerted to the sensor decreases. This process provides a signal related to the respiration of the patient, where the signal gets stronger with inhalation and weaker with exhalation. The amplitude of the signal is recorded with a fixed sampling rate of 40 Hz. After a learning period a predictive algorithm anticipates the future shape of the curve and the corresponding “tags”. The tags are labels introduced by the software, which indicates extreme values (maximum or minimum). The tag prediction feature is most useful for prospective phase gating, but this method was not investigated in this study.

The system comprises several components (figure 2.1): there are two pressure-cells that differ in their sensibility to the pressure and are labelled “high” and “low” (only the first one was used). The cell is connected to the “Sensor-Port”, which amplifies and transmits an analogue signal to the next component of the system; the “Wave-Deck”. The Wave-Deck converts the analogue signal into a digital one and manages three input/outputs signals: Beam Status, Gating and Interlock.



**Figure 2.1:** The AZ-733V system's components. One of the pressure-cells (top left) is introduced in the elastic belt (top right) and its signal is amplified by the Sensor Port (bottom right). The signal is converted to a digital one by the Wave-Deck and finally the notebook displays the signal in stand-alone mode (bottom left). Images were obtained from <http://www.anzai-med.co.jp/>



**Figure 2.2:** Through this adapter the Wave-Deck sends (and receives) three different signals: Beam Status, Gating and Interlock signals.

The Beam Status signal is the name for the Transistor–Transistor Logic (TTL)-signal produced by the CT (or treatment machine) and indicates if it is currently delivering any X-rays. The Gating-signal is sent by the Wave-Deck to discontinue radiation delivery based on some previously selected thresholds and finally the Interlock is the signal, which ultimately stops any X-ray delivery if irregular breathing or coughing is detected. The Gating and Interlock features were not used in this study.

When the system is connected directly to the CT the breathing signal is displayed only at the CT-console (see section 4.1.1). This case will be later referred as “using the proprietary CT interface”. Alternatively, the AZ-733V system can also be used in a stand-alone mode, where it still receives the beam on/off TTL signal from the connection to the CT, but the signal is displayed only on the system’s notebook (figure 2.3).

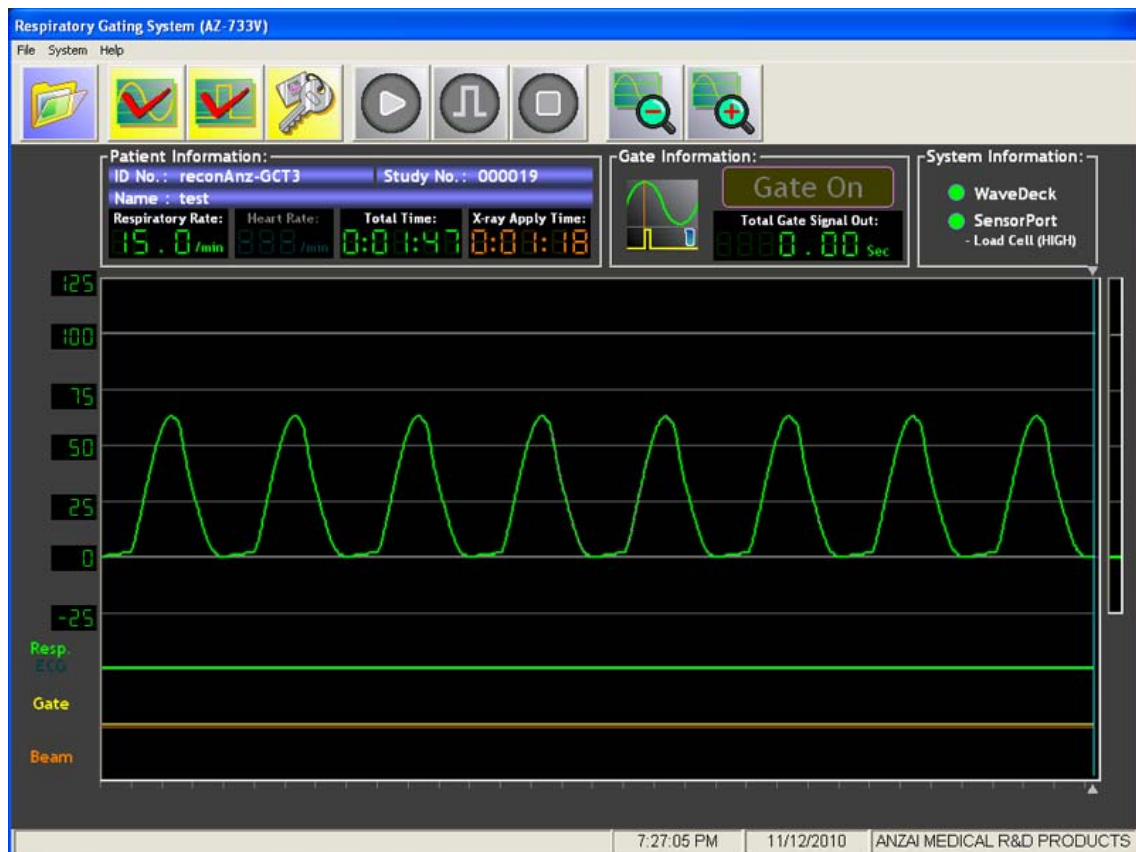


**Figure 2.3:** An example of the displayed information by the software on the notebook from the AZ-733V system.

To obtain a good signal from the pressure-sensor, the belt must be neither too tight nor too loose. The sensor port provides visual aids to find a proper strain level. The fine-tuning takes place at

software level. The peak-to-peak amplitude can be amplified or reduced and the baseline can also be corrected, either automatically or manually. When the notebook is used, measurements can be stored as an ASCII-file (.DAF) on the notebook's hard disk. Then, if a retrospective 4D-CT is going to be reconstructed the ASCII file can be imported to the CT-scanner through an "open interface", which allows the use of third vendor EBMSs. To use this interface, the file header and breathing information must first be converted into a specific format (see section 2.3).

## 2.2 GateCT

The second system is the stereoscopic camera system VisionRT (VisionRT Ltd., London, U.K.) which has been installed at the CT (Somatom Sensation Open, Siemens AG, Erlangen, Germany) as well as at a linear accelerator (Artiste, Siemens AG, Erlangen, Germany) at our clinic. The system's hardware acquires a 3D-surface model of the patient and depending on the software used, three different tasks can be done with this surface. Patient setup correction is available through the software AlignRT, (Bert et al. 2005; Schöffel et al. 2007). Real-time tracking (sampling rate between 8 to 16 Hz) of the surface regions is possible with the software GateCT. The software generates a signal, which can be used for the retrospective sorting of 4D-CTs projections. Even gating of a linear accelerator (linac) is possible (software GateRT). In this study, only the middle camera installed at the CT was used together with the GateCT software (figure 2.4).

The stereoscopic principle of the VisionRT-system exploits the parallax produced by the separation between two CCD cameras. Just as the human eyes, this subtle difference allows to infer the distance of the observed object. An object in space ( $O$ ) will be observed in a different location at each CCD's plane (figure 2.5) and when comparing both planes, the result will produce a discrepancy. This discrepancy increases as the object  $O$  is located further away of the convergence point  $C$  of both cameras. If the camera-system-geometry is known, then by processing the discrepancies the depth of each point can be determined.



**Figure 2.4:** The middle camera is used for the GateCT system, whereas the AlignRT software is run on the two other cameras installed on the ceiling of the CT-room. For this study only the GateCT system was used.

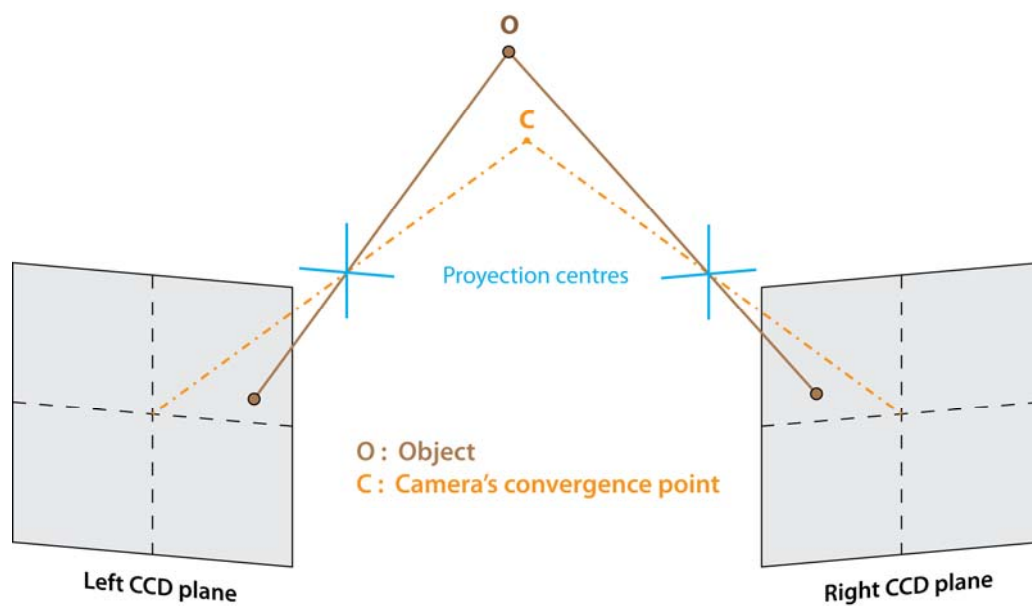


**Figure 2.5:** Schematic view of the stereoscopic principle. The same object (O) will be seen at different locations in each CCD camera plane. This difference increases as the objects moves away of the convergence point (C).

The imaging technique used, namely stereo optic photogrammetry (for more information please refer to (Siebert and Marshall 2000; Sjö Dahl and Synnergren 1999), can process the whole surface in one single shot. Subsections of the images taken by one of the cameras are selected and then the corresponding match is searched in the image produced by the second camera. Yet sometimes it is rather difficult to find a match between the subsections obtained by each camera, especially due to the lack of landmarks or representative features. The absence of enough information to individualise a subsection can lead to a mismatch. To solve this problem the system projects a pseudo-random pattern (figures 2.6 left), which provides a unique set of speckles for each subsection.

As mentioned before, the camera-system geometry must be known beforehand. For this reason, a calibration process has to be performed. A white plate with black circles spatially separated by a fix distance is positioned on the CT-Isocenter (figure 2.6 right). Four different circles with a known distance between each other must be selected by the user in the calibration software. Then the system automatically detects the remaining circles in the plate and the calibration is completed.

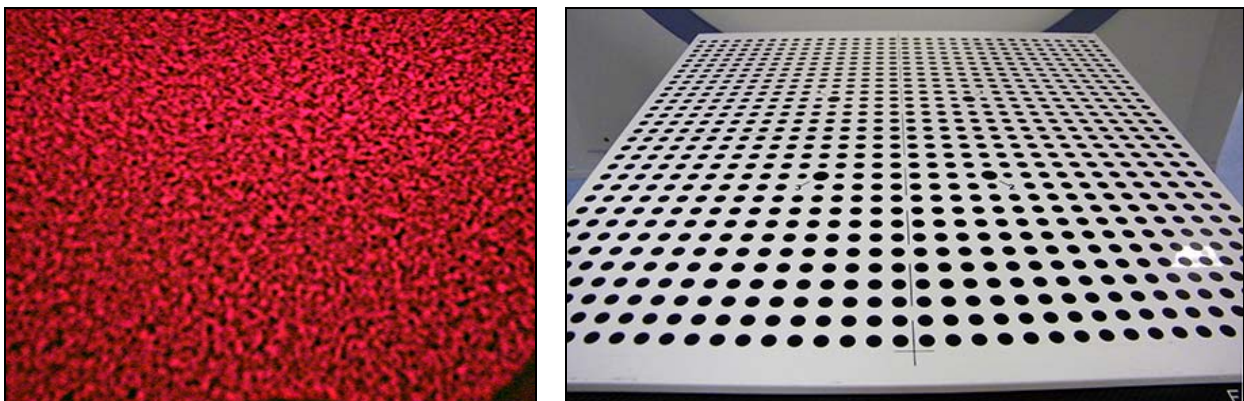


**Figure 2.6:** Pseudo-random speckle pattern used to enhance image matching between CCD cameras (left) and the calibration plate used to determine distances by the GateCT system (right).

For the CT-application as shown in figure 2.7, a pod containing two CCD cameras, a speckle projector (used to project the pseudo-random pattern), a speckle- and a normal flash units (to illuminate the speckle pattern and the texture acquisition) and a texture camera (not used by the GateCT software) is mounted at the ceiling in-line with the couch with view into the bore of the CT.

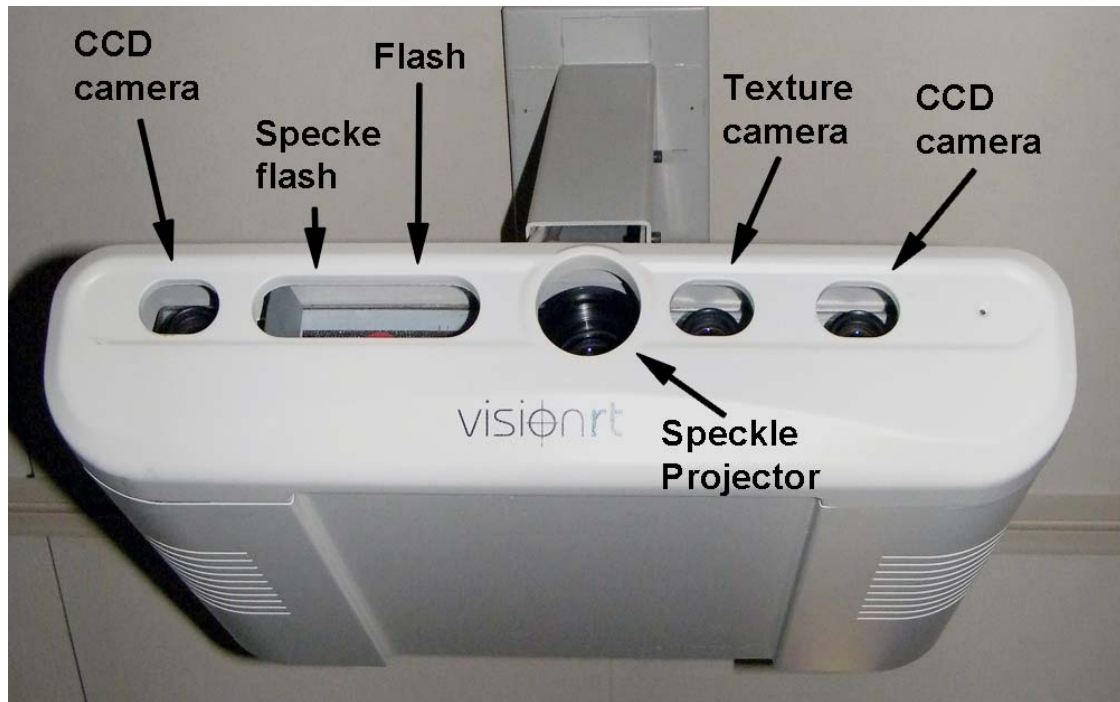


**Figure 2.7:** Detailed view of the VisionRT hardware. Each pod contains a pair of CCD cameras, which are located at both ends to enhance the parallax.

Prior to the 4D-CT acquisition, a static 3D-model of the patient surface is acquired in which a small region of interest (ROI) is selected to be tracked. During 4D-CT acquisition, the anterior-posterior movement of the selected ROI is recorded and used as surrogate of the respiratory motion. If needed, a second ROI may be chosen in a stable area, such as a bony surface, to detect unintended patient movements.

Both spiral and axial CT-modalities require moving the couch through the CT-bore (figure 2.8). This movement has to be removed from the detected tracked ROI. To cope with this, the GateCT software calculates the velocity of the couch following the equation 1.14. The necessary parameters, obtained from the CT-protocol, are typed in by the user. Then, GateCT offers the possibility to “wait for CT”, meaning that it will take into account the calculated velocity in the 3D-surface movement, only when the X-Ray On signal is detected. During operation, the millimetre-amplitudes of the signal are displayed as a function of time in the GateCT-software (figure 2.9) and the tags marking the position of the minimum and maximum amplitudes are generated in real-time.

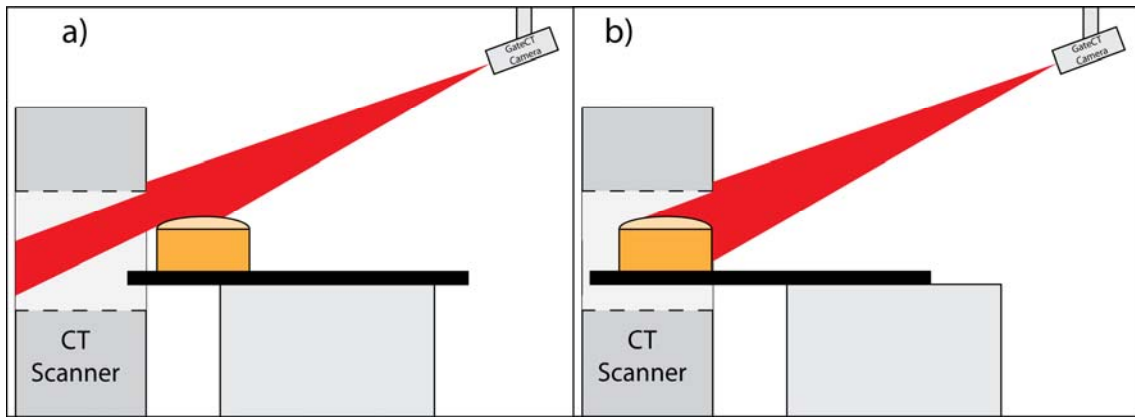


**Figure 2.8:** A schematic view of the GateCT system operating before a) and during a CT scan b). The translation of the couch is taken into account and removed from the tracked signal.

After the CT-scan, the respiratory signal can be reviewed and the tags can be edited retrospectively either manually, in the “Review Mode”, or automatically by means of a “reprocess button”, where the phase values are recalculated, and the tags are relocated if necessary. Following the vendor’s recommendation, for this work all GateCT-tags were automatically reprocessed. The workflow used in a GateCT acquisition is summarised in figure 2.10.

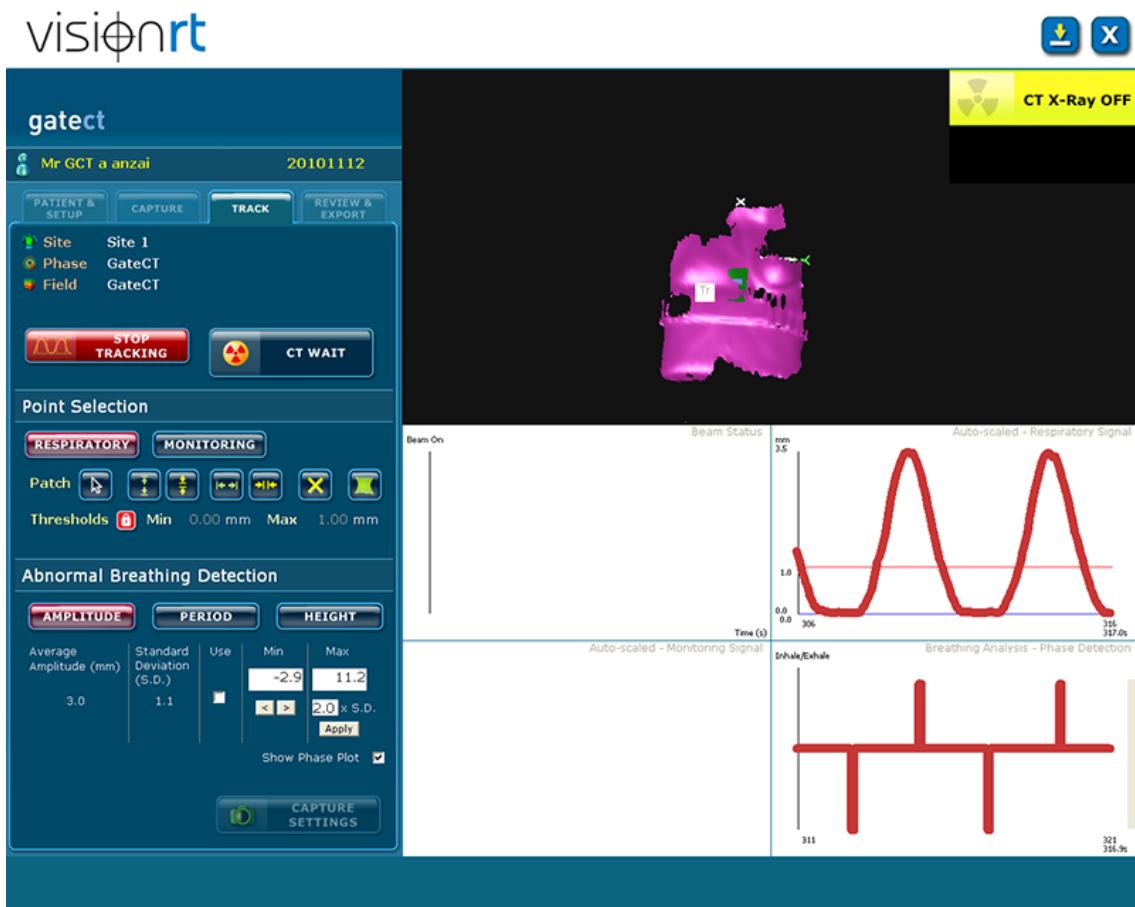


**Figure 2.9:** An example of the information displayed by the GateCT software. The surface of the phantom (upper right), the breathing signal (middle right) and the automatic tag detection (bottom right).

To transfer the GateCT signal to the CT, a proprietary or an open interface may be used. In the first, the breathing signal is displayed only in the CT-console (section 4.1.1). In the latter, the breathing curve is only displayed in the GateCT-software and when the scan is over, the breathing curve is stored as an ASCII-file and then imported into the CT-console.

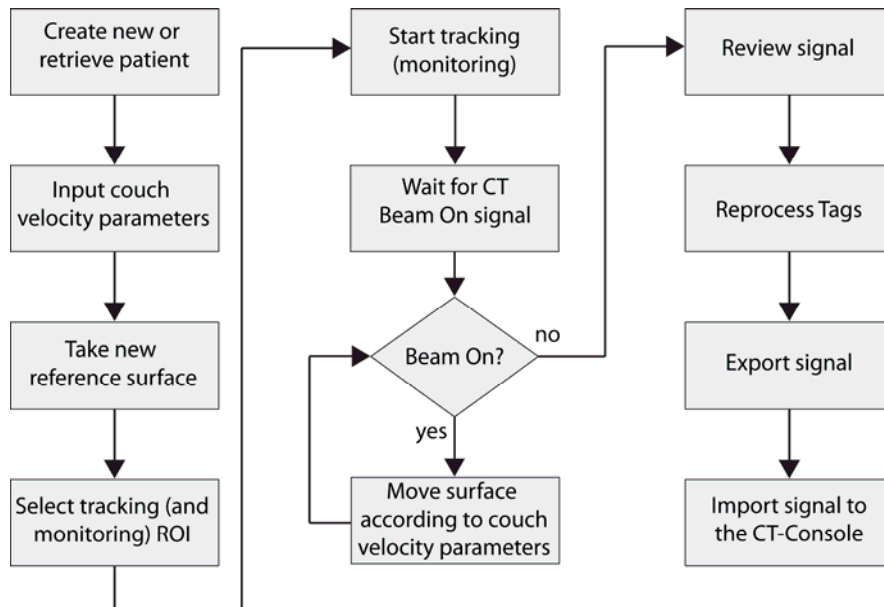


**Figure 2.10:** Workflow of a breathing signal acquisition for 4D-CT imaging using the GateCT-system.



**Figure 2.11:** Geiger-Müller detector provides the CT-beam status signal.

The hardware interface between the GateCT-system and the beam on/off information is provided by the “Gate-Controller”. The beam on/off information is obtained either directly from the CT or from a radiation detector. Since in most measurements the CT-connection was required by the AZ-733V hardware, a Geiger-Müller detector (GM-10, Black Cat Systems, Westminster, MD, USA) was

used to provide this information to the Gate-Controller and therefore to the GateCT-system (figure 2.11).

## 2.3 Breathing data files format

When a retrospective 4DCT is been reconstructed, a signal with the information about the breathing is required. In the case of the open interface of the CT-console this information is given as an ASCII file with determined format specifications, based on the files produced by the RPM system from Varian (personal communication, Florian Wesse, 06.10.2008, Siemens AG, Erlangen, Germany).

**GateCT File**

```

[Header]
CRC=0
Version=1.6
Data_layout=amplitude,phase,timestamp,validflag,ttlin,mark,ttlout
Patient_ID=20110110
Date=01-10-2011
Total_study_time=89.543
Samples_per_second=14 ← Sampling rate value in Hertz
Scale_factor=1
[Data]
2.5897,0.0000,2140,0,1,,0
2.3929,0.0000,2230,0,1,,0
2.1042,0.0000,2280,0,1,,0
1.8424,0.0000,2349,0,1,,0
1.5775,0.0000,2419,0,1,,0
1.2462,0.0000,2489,0,1,,0
0.9892,0.0000,2558,0,1,,0
0.7315,0.0000,2629,0,1,,0
0.5193,0.0000,2698,0,1,,0
0.3209,0.0000,2768,0,1,,0
0.1872,0.0000,2838,0,1,,0
0.1095,0.0000,2907,0,1,,0
0.0000,0.0000,2977,0,1,,0
0.0421,0.0000,3047,0,1,Z,0 ← 'Z' = Peak Tag
.....
.....

```

**Figure 2.12:** Example of the format of a VXP ASCII file. The header specifies patient, date, hour, data type and sampling rate information. The rows below the header store the detected breathing data. Header nominal sampling rate and the first tag detected are highlighted.

The files include a header and 7 columns of comma separated values (figure 2.12). The 2<sup>nd</sup> row of the header stores the Cyclic Redundancy Check (CRC), which is an error control value. The next row indicates the Version used in the exported file. The 4<sup>th</sup> row specifies how the data is going to be presented. Then, the patient is referenced through his or her Identification Digit (ID).

Afterwards, the date of the study is shown and how long the X-Beam On signal was detected in rows 6<sup>th</sup> and 7<sup>th</sup>, respectively. The 8<sup>th</sup> row is of great importance, because it contains the mean sampling rate value, which indicates how often the tracking ROI is measured per second. Finally the scale factor indicates if the data is in millimetres ( value = 1 ) or in centimetres ( value = 10 ).

As mentioned before, the comma separated values containing the breathing data is separated into 7 columns, which will be now explained in detail:

The 1<sup>st</sup> column contains the amplitude values. The 2<sup>nd</sup> column stores the signal's angular phase. The increment of this value is a fix amount and it is determined by two adjacent maximal amplitudes. Given that the system writes a phase value equal to zero at each detected maximum, the values between these maxima are interpolated a posteriori (from 0 to  $2\pi$  ). The 3<sup>rd</sup> column contains the time stamps of the measurement in milliseconds. The 4<sup>th</sup> column is a binary flag set by GateCT to indicate if the stored data is valid (zero) or not (one). This is used in cases where the patient moves or coughs during the CT-scan and allows discarding those projections taken at those precise moments, diminishing possible artefacts in the reconstructed images. The 5<sup>th</sup> column indicates the presence of the beam on signal with a 1 (or zero for lack-of). The user has to take into account that some CT-softwares may have an opposite convention for this value. The 6<sup>th</sup> column stores the tag values. These values indicate a peak (e.g. lungs full with air) or a valley (end of exhalation) with the letters "Z" and "P", respectively and it is left empty for any other amplitude. The location of the tags is highly important for phase-based 4D-CT, as they are used to determine the phase written in the 2<sup>nd</sup> column. For amplitude-based 4D-CTs, the tags are used to separate the curve in two parts, the inhalation (from a valley to a peak) and the exhalation (from a peak to a valley). Finally the 7<sup>th</sup> column stores the flag indicating if the beam was gated by the GateCT system (one) or not (zero). This value is used for prospective gating, which was not the case for this study.

Figure 2.13 presents a typical DAF-ASCII file from the AZ-733V system. This file contains all the necessary information to be used in a 4D-CT reconstruction, but the format in which it is written does not comply with the format (Varian) required by the open interface. To be able to use this file, an in-house developed C++ software was written to convert the format, while leaving the data of the breathing signal unaffected.

**Anzai File**

```
"AZ733V";Version 2.2G      "  
"Date:";2011/01/10"  
"Start(hh:mm:ss);";17:24:08"  
"End(hh:mm:ss);";17:25:39"  
"Length(hh:mm:ss);";0:01:31"  
"X_Apply(sec);";55.025 "  
"GatingModeNumber;";1  
"ECGUse;";0  
"GateTotal;";0  
"RespAve(sec);";3.938044  
"HeartAve(sec);";0  
"DataPosi;";104  
"DataMagn;";671  
"Sample;";3623  
"Comment;"; "  
"Data Time(msec);";25  
"Sweep Point;";In: 50"  
"Start Point;";In-Peak"  
"Gate Width(msec);";200"  
"All Gate time(sec);";0.00"  
"  
"  
"  
"  
"  
"  
"  
"  
"  
"***DataNo., RespLevel, RespPhase, RespGate, EcgLevel, EcgPeak, EcgGate, GateOut, BeamIn, Error Message(Inter Lock)***"  
"***Data start***"  
0,0,0,0,0,0,0,0," (0)"  
1,-30,3,0,0,0,0,1," (0)"  
2,-22,3,0,0,0,0,1," (0)"  
3,-14,3,0,0,0,0,1," (0)"  
4,-6,3,0,0,0,0,1," (0)"  
5,1,3,0,0,0,0,1," (0)"  
6,1,3,0,0,0,0,1," (0)"  
.....  
.....
```

**Figure 2.13:** Example of the format of the ASCII file produced by the AZ-733V system. The file contains all the required breathing data, but before it can be used for 4D-CT reconstruction it must be converted into the VXP format.

## 2.4 Comparison of breathing monitor systems

The AZ-733V and the GateCT systems differ on how they physically record the human breathing . For this reason it was necessary to evaluate their performance in acquiring the respiration of human subject under a common reference. The following section will provide a comparison between the EBMSs, where shape, baseline drift, extrema value synchronization and tagging precision will be analyzed.

### 2.4.1 Materials and Methods

Two breathing patterns from a healthy male volunteer were recorded with the GateCT- and the AZ-733V systems running simultaneously. For the first pattern, the volunteer, who was lying on the CT-couch, was asked to breathe regularly, while for the second pattern, the volunteer was asked to suddenly inhale deeply and to continue breathing with a higher frequency. This sudden change was done to simulate an irregular breathing curve.

The AZ-733V was located around the waist of the volunteer half-way between the xyphoid process and the umbilicus. The pocket to accommodate the pressure sensor in the belt was located slightly to the right side of the patient. At the GateCT-software the tracking ROI was placed on the sternum. For radiation safety reasons, the CT-source remained off at all times. Accordingly, no CT-couch movement took place during this measurement. Due to the lack of the X-ray on signal, synchronization of both signals was achieved, by manually matching one of the extreme values.

For both systems, the precision of the tag positioning, meaning the amount of time between the time stamp of a tag (e.g.,  $t_{\text{tag-peak}}$ ) and the time stamp of the real extreme value (e.g.,  $t_{\text{peak}}$ ) was studied. A smaller difference between these values will indicate a better tagging precision. The time stamp of the tag was obtained directly from each ASCII-file and the one of the real extreme value was calculated using a local maxima (minima) detection algorithm using the “OriginPro 8.5. Academic” software (OriginLab Corporation, One Roundhouse Plaza, Northampton, MA, USA).

## 2.4.2 Results

The breathing curves of the volunteer as recorded by both EBMSs are presented in figure 2.14. Even though the synchronization was not optimal and it was done manually using just one extreme value, the normalised breathing curves agreed well, showing that all other peaks and valleys occur synchronously both in the regular and irregular case. Had both curves used not been synchronous, then the extreme values would have presented temporal shifts.

On the other hand some difference can be observed, when comparing the amplitude, especially for the irregular breathing curve, where after the biggest inhalation the baseline of the signal recorded by AZ-733V remained more or less stable, whereas the signal of the GateCT system shows a change of relative amplitudes. The differences observed can be explained by the anatomical position difference that both systems have. The AZ-733V measures the abdominal expansion motion, whilst GateCT the thorax movement in the anterior-posterior direction.

The tagging precision for peaks and valleys for both monitoring systems is shown in Table 2.1. In both regular and irregular curves, GateCT presents a more precise tagging. This is a direct result of the reprocessing made by GateCT retrospectively. It was also noticed that the AZ-733V system detected extra tags, where no extreme value was actually located.

**Table 2.1:** Precision of tagging in the voluntary breathing signals for both investigated systems and both breathing cases. A smaller difference indicates a better tagging precision.

Breathing curve	AZ-733V (ms)		GateCT (ms)	
	mean value (range)		mean value (range)	
	$t_{\text{tag-peak}} - t_{\text{peak}}$	$t_{\text{tag-valley}} - t_{\text{valley}}$	$t_{\text{tag-peak}} - t_{\text{peak}}$	$t_{\text{tag-valley}} - t_{\text{valley}}$
<b>Regular</b>	70 (-1500 to 1800)	-140 (-770 to 120)	20 (-240 to 280)	-70 (-600 to 260)
<b>Irregular</b>	-80 (-1200 to 100)	-100 (-1200 to 200)	60 (-200 to 340)	60 (-200 to 270)

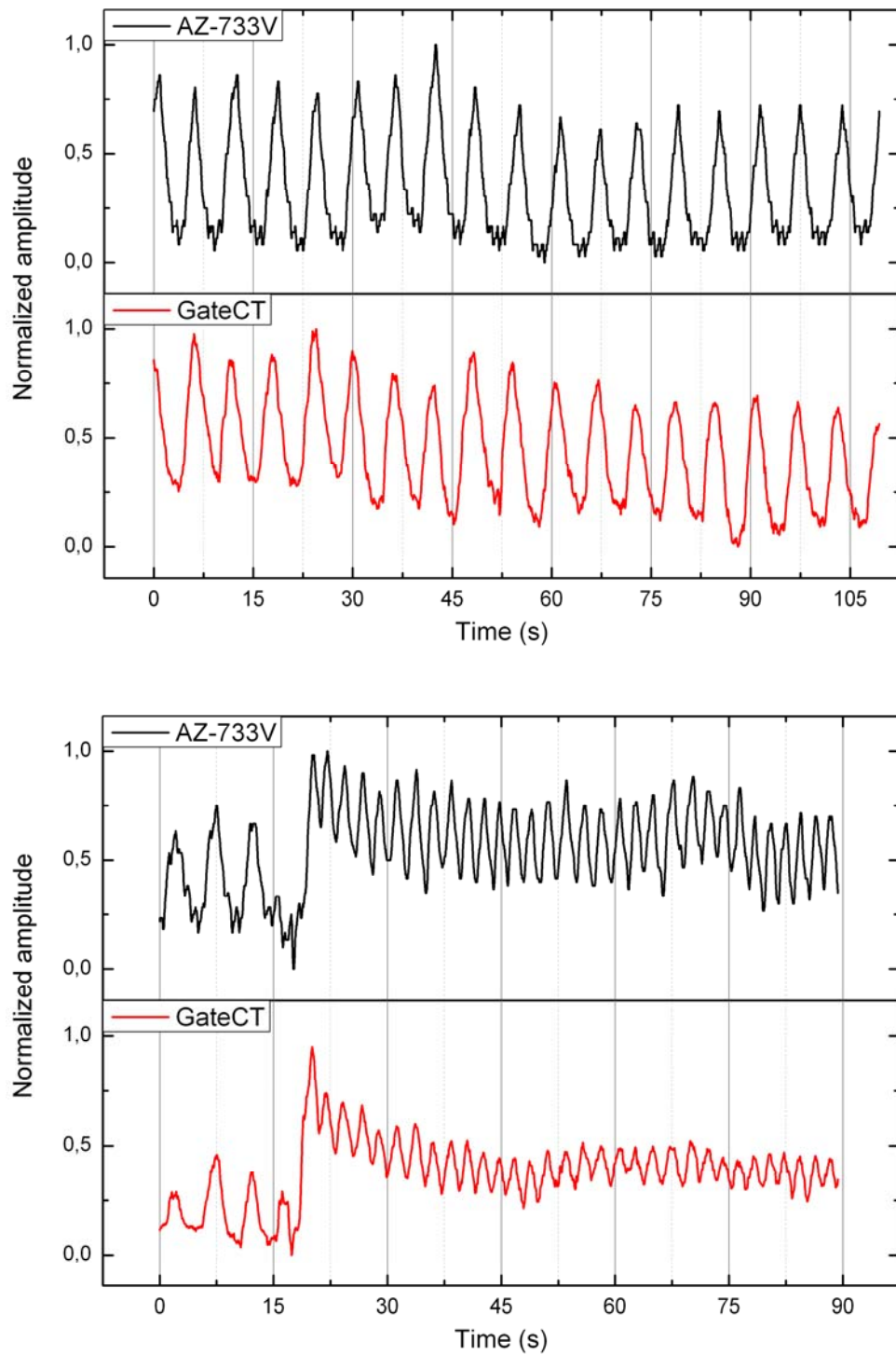


**Figure 2.14:** Normalised amplitude registered by both AZ-733V (black line) and GateCT (red line) from a volunteer breathing freely and regularly (upper graph) and irregularly (bottom graph).

# 3

## *Phantom development*

In imaging and radiotherapy, a phantom is an object, which replaces living tissue and provides a known geometry, as well as the dosimetric properties required for testing and analysing several machine parameters. In research, phantoms are used for evaluation of new technologies, and in the clinical practice as Quality Assurance tools to ensure patient safety and the correct functioning of machinery and the techniques used.

For example in imaging a phantom can help to test quantities, such as spatial image resolution, noise, artefacts, and dose, among others. In radiation therapy, phantoms are mostly used for measurements to verify dose calculations in inhomogeneous media.

Phantoms can be as simple as plates and cylinders made of plastic or as a cube filled with water. But they can also be quite sophisticated equipment, with moving and interchangeable parts, with different materials and with a complex geometry or even with an anthropomorphic shape. Phantoms are always designed and constructed to fulfil specific tasks in research and quality assurance procedures, where reproducibility and precision have high standards.

Several techniques developed to include or even compensate breathing motion can only be tested with help of phantoms with one or more movable parts. In imaging, some authors used simple, but effective phantoms with moving spheres (Ford et al. 2003; Rietzel et al. 2005), while others moved the whole phantom with help of a platform (D'Souza et al. 2005; Li et al. 2005).

With the years more sophisticated dynamic phantoms (from now on, breathing phantoms) have been developed by several groups (Nioutsikou et al. 2006; Malinowski et al. 2007; Serban et al. 2008; Vinogradskiy et al. 2009; Court et al. 2010; Szegedi et al. 2010)

Some breathing phantoms are also available in the market, such as the *Dynamic breathing phantom*, from Radiology Support Devices Inc., (Long Beach, CA, USA), the *Quasar*, from Modus Medical Devices Inc., (London, Canada) or the *Dynamic Thorax Phantom*, from CIRS, (Norfolk, VA, USA).

Dosimetrical studies can be performed on most of the mentioned phantoms and almost all provide the means to generate a respiration signal from a EBMS, but only a few are compatible with two monitoring systems working simultaneously and only the last one (after some upgrade and solving some practical issues) could have the capability of providing a movable surface needed for testing an optical breathing monitoring system, yet this phantom is focused only on lung tumours.

Therefore in this work, a newly developed anthropomorphic breathing phantom is presented, which was specially constructed for testing simultaneously two different breathing monitoring systems (a pressure sensor and an optical camera system) and it is focused on two different tumour regions.

Section 3.1 will give detailed information about the phantom design and construction, section 3.2 will explain how the phantom breathing is generated, section 3.3 will show how the phantom can operate two moving parts simultaneously, section 3.4 will provide information about how dosimetrical studies can be performed using the phantom and finally section 3.5 will present the capabilities of the phantom to imitate human breathing.

### **3.1 Design and construction**

To investigate the 4D-CT reconstructions obtained with different respiration monitoring systems, an anthropomorphic breathing phantom representing the torso of a human was developed (figure 3.1). The phantom is designed for simulation of motion of lung and breast tumours for which respiratory motion plays a significant role in imaging and radiotherapy treatment.

The phantom is shaped as a rigid thorax and it is built in slabs of different materials. Special care was taken in the construction of the parts which will be involved in dosimetric measurements. For this reason only tissue equivalent materials were used for the main tissue types in the target regions. The surface of the phantom was adopted from a commercially available cardiopulmonary

resuscitation training (CPR) manikin (“Little Anne”, Laerdal Medical, Stavanger, Norway), from which only the flexible rubber skin was used as the outer contour of the phantom’s chest wall. Anatomically, the phantom possesses two target regions: a lung tumour and the left breast. Also two lungs and a heart are present as the main organs at risk (figure 3.2 right).

For stability reasons, the outer contour of the phantom was made of PMMA, which is nearly tissue-equivalent. The lungs were made of polyurethane (Obomodulan, OBO, Stadthagen, Germany), which has similar density and absorption properties as real lung tissue. The heart was made of white polystyrene (RW3, PTW-Freiburg, Freiburg, Germany) to show density contrast to the neighbouring PMMA-structures in the CT-images. Several cavities were added for the inclusion of radiation detectors (figure 3.2 left) and as the phantom consist of several slabs stacked, films can be positioned between them.

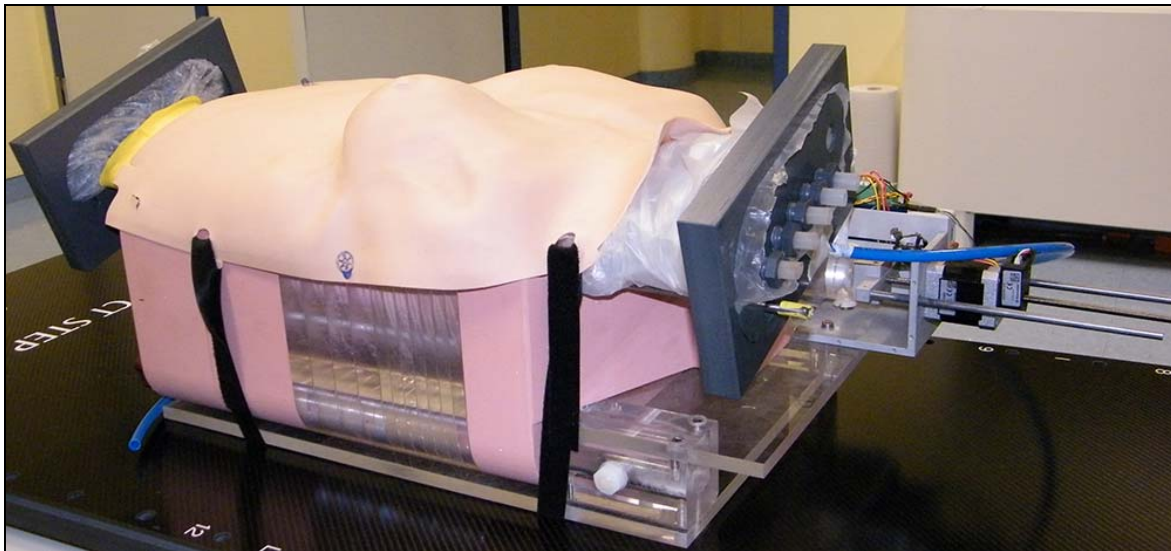


**Figure 3.1:** Phantom lying on the CT-couch seen from its left “shoulder”.

As the rubber skin taken from the CPR manikin represented an adult male, to simulate the female anatomy, the zone around the left breast was expanded and modified. The left breast was selected because of its proximity to the heart, which makes the latter an organ at risk (OAR). Since the CPR-skin is only 2.5 mm thick, it does not provide enough photon attenuation. Therefore the thickness of the chest wall was increased with a layer agarose gel (Agarose HEEO Ultra-Qualität, Carl Roth GmbH & Co. KG, Karlsruhe, Germany). Agarose is an organic compound [ $C_{24}H_{38}O_{19}$ ] and a low concentration (1 g per 100 mL of water) was used to ensure dosimetrical water equivalence. The agarose gel used is flexible, yet hard enough to withstand time and movement. At the time of writing, the gel layer was one year old and still conserved its flexibility and stiffness. To ensure a

better fitting the gel chest wall was casted using as negatives the CPR-skin as outer and the ventral side of the rigid thorax as the inner side of the cast. The CT-values of the phantom materials were measured with a commercial software and are presented in table 3.1.

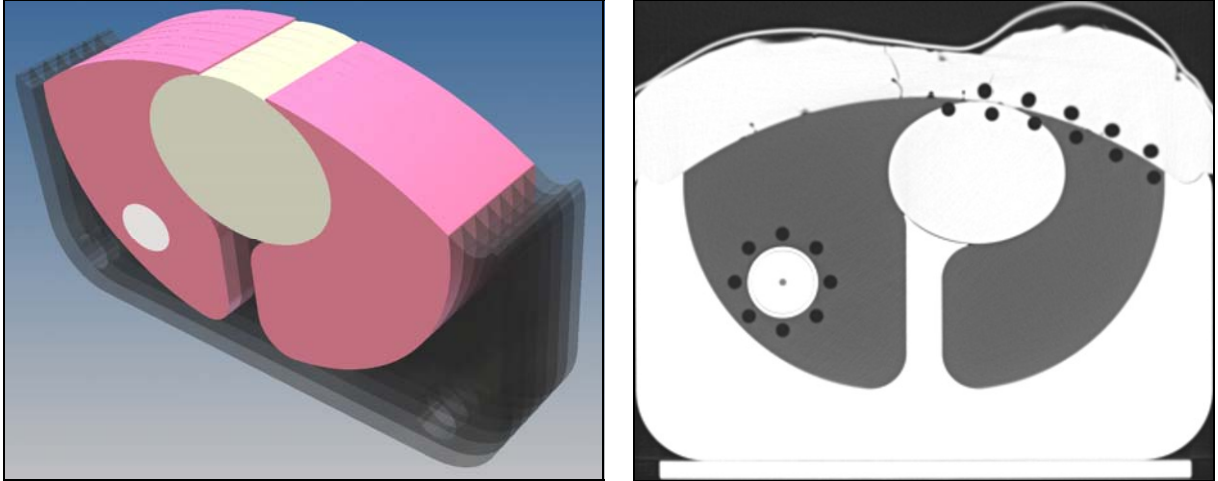


**Figure 3.2:** On the left, a schematic view of the central part of the phantom stack showing the PMMA frame (black), the lung material (pink), the heart (beige) and the lung tumour (white). On the right, an axial CT-scan image of the phantom showing the bores, where ionization chambers can be inserted for dosimetric studies.

**Table 3.1:** CT-values of materials used to build the phantom in Hounsfield-Units (HU)

"Tissue"	Material	HU
		(mean $\pm$ SD)
Lung	Polyurethane	-700.1 $\pm$ 8.5
Heart	White polystyrene	-3.1 $\pm$ 19.0
Soft	Agarose gel	-6.3 $\pm$ 14.7
Bone	PMMA	118.7 $\pm$ 19.9

The lung tumour is located at the right lung and it is designed as a PMMA-sphere with a diameter of 35.5 mm and it moves in the superior-inferior direction together with a surrounding PMMA-tube (with a wall diameter of 2.1 mm). The adjacent regions cranial and caudal to the tumour are filled with lung material, which moves together with the tumour and the PMMA-tube. In this way, there are no air cavities around the tumour. Any material or machinery, such as the motors (see next section) that could cause any imaging artefact were carefully positioned outside of the area of the targets.

## 3.2 Breathing motion

The movements of the tumour and the skin surface are produced by means of two stepping motors (figure 3.3 and 3.4), which can be programmed to follow arbitrary motion patterns.

The first motor operates a piston (Festo AG & Co. KG, Esslingen, Germany), which inflates and deflates a bag located between the rigid thorax and the inner flexible chest wall and thereby expands the chest wall imitating human respiration. As the air is pumped through a hose, the motor can be positioned far from the radiation field. The second motor is attached to the “shoulder” of the phantom and directly controls the movement of the lung tumour in the cranio-caudal direction.

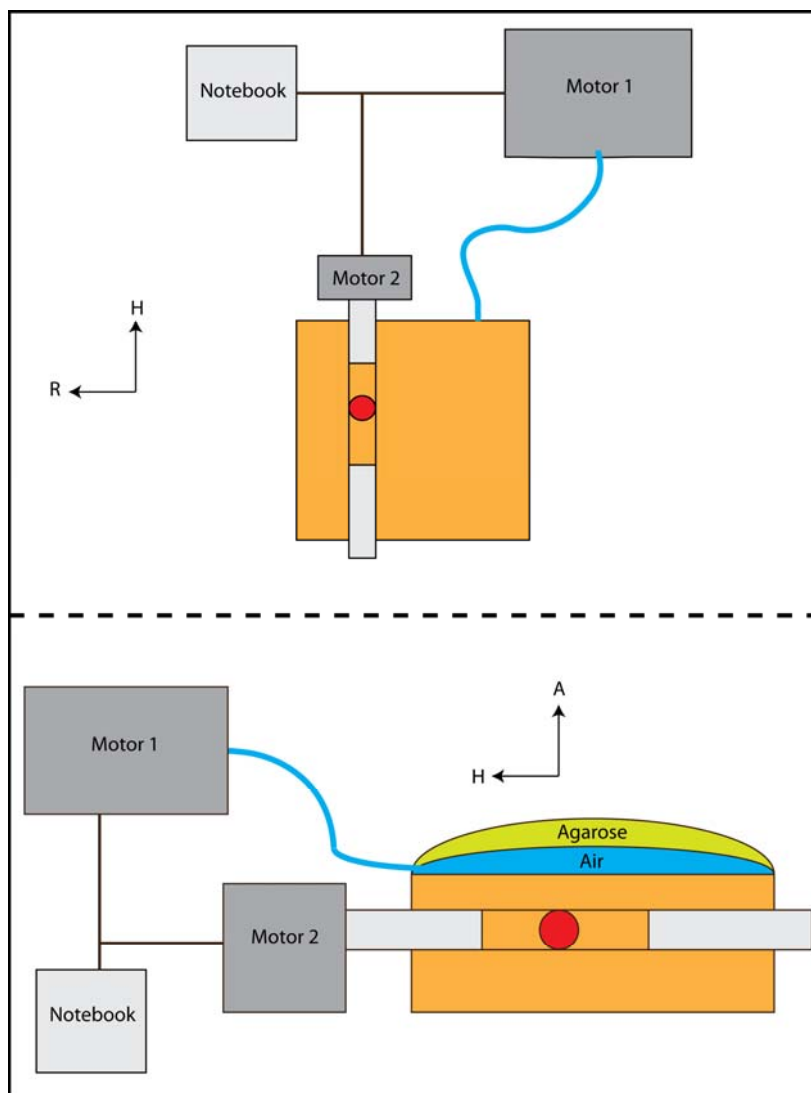


**Figure 3.3:** Schematic view of the motor connections and functionality. The tumour is depicted in red and the air cavity between the rigid thorax and the agarose gel in blue.

The design of the phantom had to take into consideration that any materials such as metals, or material containing high-Z atoms, which produce imaging artefacts, and electronics sensitive to radiation damage, had to be left outside of the volume of interest.

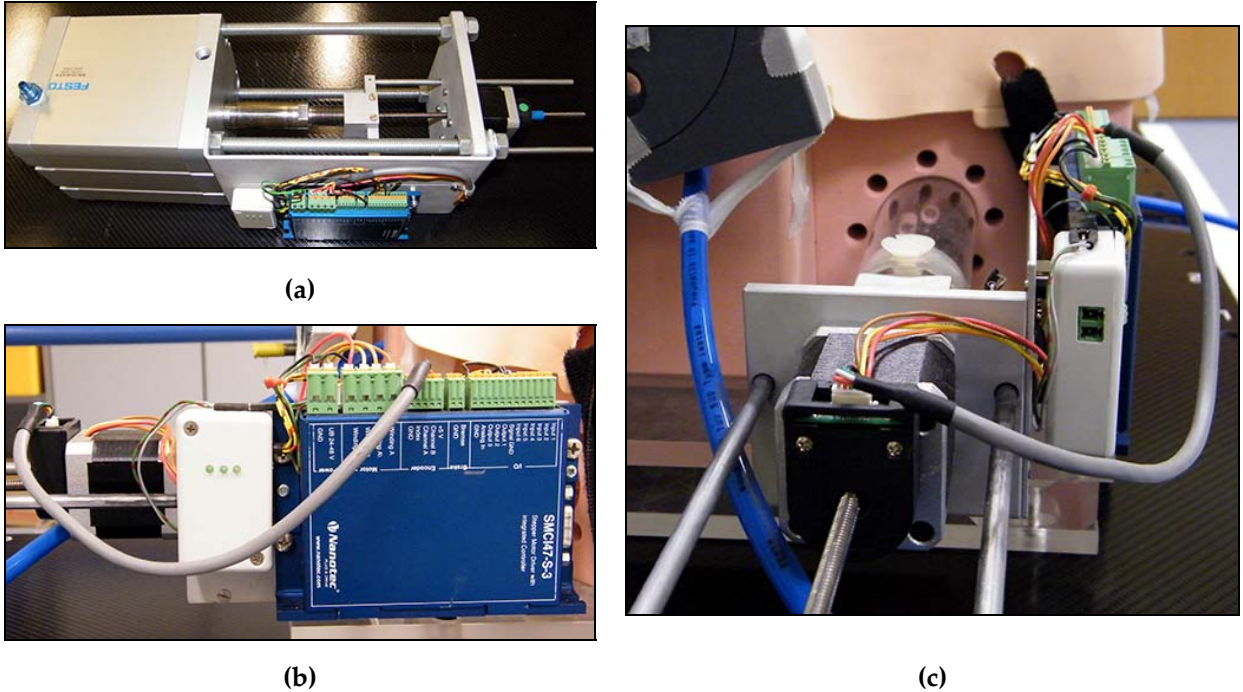


**Figure 3.4:** A single unit contains the stepping motor and the piston for pumping air (a). Lung tumour motor is attached to the right “shoulder” of the phantom (b). A more detailed picture of the motor’s controller (c).

The motor’s axis rotation is translated into linear displacement with help of a lead screw. In a single revolution, the lead screw advances 5 millimetres and this corresponds to 2000 motor steps. This results in a step resolution of 0.025 mm. The range of movement is 6 cm and ca. 9 cm, for motor 1 (air pump) and for motor 2 (lung tumour), respectively, covering the most extreme movements registered in patients (Table I, Keall et al. 2006 ).

### 3.3 Motion-control software

Both motors are controlled with an in-house C++ written software, which includes the CANopen Master Application Programming Interface (IXXAT Automation GmbH, Weingarten, Germany) libraries and it was developed with Microsoft Visual C++ 2008 Express Edition. The software is run on a notebook with MS Windows 7 Professional and is connected to the phantom via a cable of 1.5 m length.

When the motors are turned on, the software makes a full hardware check and initialises the network, adding any motors attached, sending pre-defined parameters to their local memories and including a protocol specifying how the data is going to be sent and received. The functionality and connection integrity is checked continuously during runtime.

The software enables the motors to reproduce from simple periodic movements to very complex aperiodic movements (e.g., obtained from patients). During runtime the user can choose from one of these sources.

For the periodic movement, the parameters; peak-to-peak amplitude, period, starting offset position and the number of repetitions of the curve are introduced by the user.

If patient data is chosen, it must be first imported and translated into motor's axis positions. Breathing paths can be converted from Varian / VisionRT (VXP-file, version 1.6.) and Anzai (DAF-file, version 2.2G) formats (see section 2.4). As each motor's hardware is an independent unit, the same or different curves can be run in each motor. This allows e.g., to reproduce real lung tumour motion with one motor and with the other the thoracic breathing motion of patients, therefore enabling the study of breathing influence on imaging and radiotherapy under conditions close to reality.

Once the user has specified, which trajectories are going to be run, both motors start executing a reference sequence, in which a specific physical position is found and set as the zero position. This procedure ensures that when a measurement is repeated, the given curves will always start with the same offset.

It is highly likely that the first position of the loaded curve is not the same position as the reference position and therefore the motor's axis must be moved manually to the first curve position. Then, the automatic motor's controller can be activated and the whole process of sending and receiving data proceeds without the user's intervention.

A motor position is packed in the Process Data Object (PDO), which can contain messages of up-to 8 bytes. The content of the data is already known by the sender and the receiver(s), as it was previously defined at initialization of the network. This type of communication does not require a confirmation of the message's arrival back to the transmitter, as some other transmission protocols

require. Therefore PDOs can be processed as soon as they arrive to destination and adding the feature that PDOs can be broadcasted after a high priority event is detected, real-time communication is possible. To achieve an optimal coordination between both motors, the event used to trigger the PDOs was a synchronization signal (Synch).

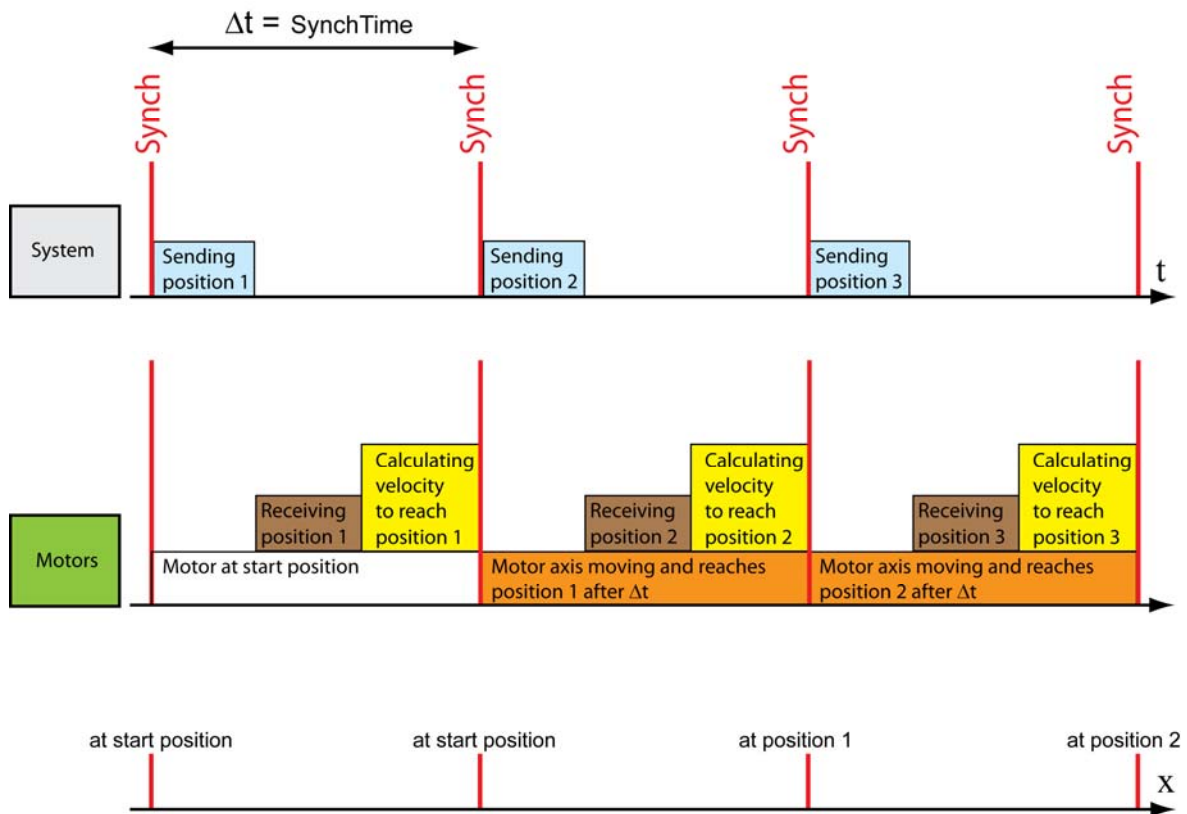


**Figure 3.5:** Schematic of the protocol for motors' synchronization. The upper line shows the system's activity and the Synch-event times (red lines). The middle line shows each motor's perspective and the processes done in a SynchTime period. Bottom line shows the motor position at each Synch event.

For each Synch, the next motor position is sent to the motors and the hardware calculates, through linear interpolation, the velocity needed to reach that position within two Synchs (SynchTime). Only when the next Synch arrives, the motors will start to move to their previously received position. This protocol ensures a smooth transition between positions by eliminating any delay produced by circuit jitter and system latency. As the motors are connected in parallel, this protocol also ensures a proper synchronization between the movements of the lead-screws. Given that linear interpolation requires the actual and the next position, a time delay of twice the SynchTime occurs between sending the position and the axis actually reaching it (figure 3.5).

### 3.4 Dosimetry in the phantom

For irradiation experiments, the phantom can be equipped with several dosimetrical instruments. The target region of the thorax consists of slabs where radiochromic films (Martisíková, et al. 2008) can be axially inserted. As the tumour is surrounded by the PMMA-tube which runs through the phantom cranio-caudally, the films have to contain a hole at this location. The tumour, which is made of two hemispheres, may also carry a circular shaped piece of film. Films are especially useful for Intensity Modulated Radiation Therapy (IMRT) given the high spatial resolution, adequate for investigating step dose gradients.

In addition, the phantom contains several bores (or Polyethylene-tubes in the case of chest wall) in which pin-point ionization chambers (ICs, TM31009/31015, PTW Freiburg, Germany) can be installed. The ICs have sensitive volume of  $0.03 \text{ cm}^3$  and provide a high spatial resolution. The absolute dosimetry is simpler in ICs than in films. The tips of the ICs can be embedded in tissue equivalent material to avoid air gaps near the IC cavities. There are 12 IC positions for each target region as seen in figure 3.2 (left). For breast cancer treatment dosimetry, a group 5 ICs can be located within the chest wall. When the motor is pumping air into the cavity between the chest wall and the thorax, the ionization chambers are displaced accordingly, in a roughly anterior-posterior direction. A second group of 6 chambers can be inserted within the rigid thorax, directly opposing the previously 5 mentioned ICs. These detectors are positioned there to investigate doses delivered to the heart and the upper section of the left lung, which are the main organs at risk for breast cancer radiotherapy. The distance between these two groups of chambers will vary while the phantom operates. An additional IC will be inserted at the centre of the breast and will be used to measure the dose at the centre of the target volume.

For the lung tumour, 2 ICs are located within the tumour and another 2 cranio-caudally in the neighbouring lung tissue (figure 3.6). As the tumour moves these four chambers will be integrating the dose of several positions. These will be in opposition with the additional 8 ICs, which are positioned around the tumour and are fixed in their location. Dose blurring effects can therefore be studied with this configuration. The exact cranio-caudal position of the ICs outside the target regions can be adjusted by means of rods inserted from the opposing side.

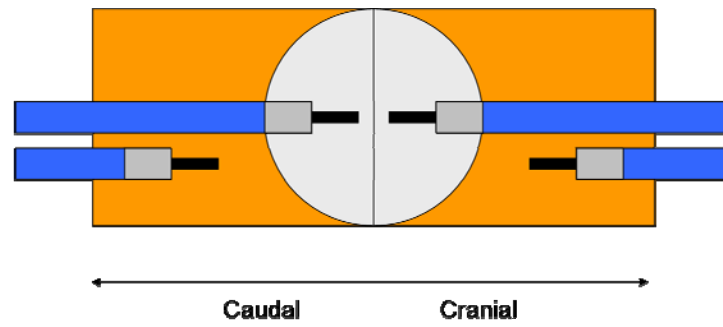


Figure 3.6: Configuration of the ionization chambers located within the lung tumour.

### 3.5 Imitating human breathing

The development of the phantom included more than just being an anthropomorphic phantom with motion capabilities. The goal of the design and construction was to provide a tool capable of reproducing the human surface motion as exactly as possible. To achieve this, a calibration process was performed and then the phantom capabilities were tested to emulate the breathing of a healthy volunteer, as will be explained in the following subsections.

#### 3.5.1 Materials and Methods

While the millimetre-amplitude of the tumour motion in the phantom can be directly controlled by the stepping motor, this is not the case for the respiratory motion of the phantom's surface since this motion amplitude depends on air volume pumped by the piston into the phantom's cavity. To imitate the millimetre-amplitude skin motions of the volunteer using the phantom, a calibration was performed by correlating the position of the piston with the position of the exterior rubber skin using the GateCT-system. This relation turned out to be linear with only a minor offset at small amplitudes (figure 3.7).

The previously obtained GateCT files from the volunteer (subsection 2.4.2) were used as input by the phantom's control software. The software transformed the amplitude signals to axis positions and took into account the calibration curve in the case of the air pump motor. The phantom motors executed the instructions of the software and the skin displacement of the phantom was tracked with the GateCT-system. This new curve was exported as a new file. The comparisons of the input and the new files were performed for both free and irregular breathing curves.

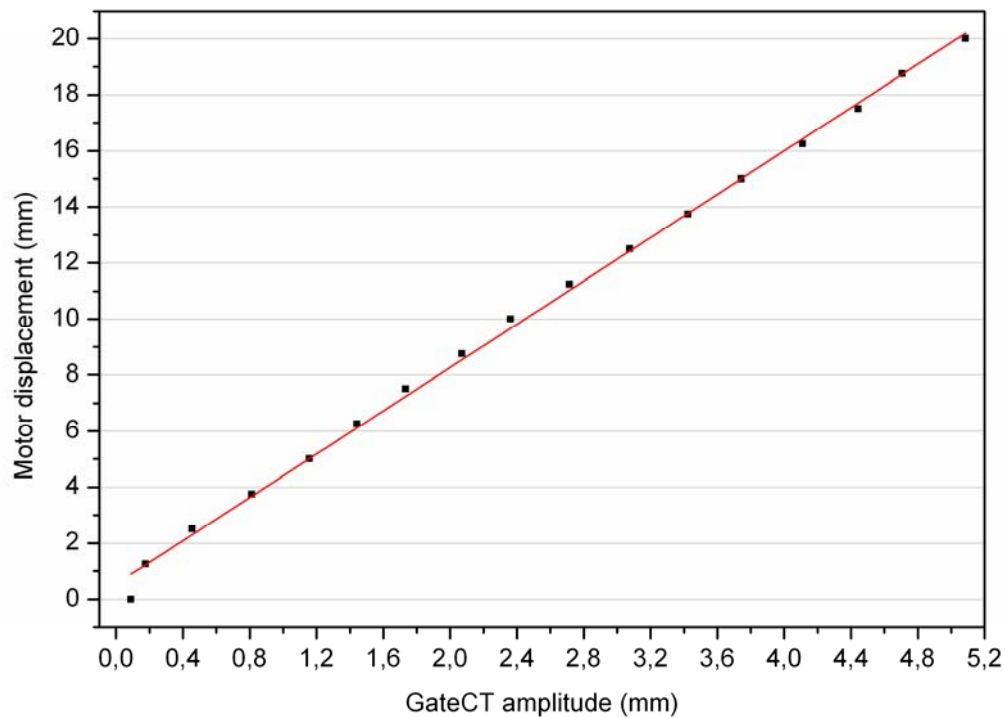


**Figure 3.7:** Calibration of the piston position to the millimetre-amplitude measured with the GateCT system. The regression line was used to find the correct motor positions to imitate the respective amplitude of the volunteer.

### 3.5.2 Results

The breathing motions of the volunteer were reproduced by the phantom with a high accuracy as shown in figure 3.8. This is demonstrated by the high Pearson's coefficient value  $r=0.994$  and  $0.991$  for regular and irregular breathing, respectively (figures 3.9) indicating a strong linear dependence between the input and reproduced curves. A strong sign that the calibration curve used delivered reliable results can be found in figure 3.10, where the difference between the motion amplitude of the volunteer and the motion reproduced by phantom was always less than  $\pm 0.4$  mm for both regular and irregular patterns. Also shown by the figures, is a small but growing tendency of the difference to increase with time. This is indicated by the linear fits of the data and it was found that a small air leakage in the air pump system was the cause. The air leak was slightly bigger in the case of irregular breathing, where higher amplitudes and therefore higher air pressures were used.

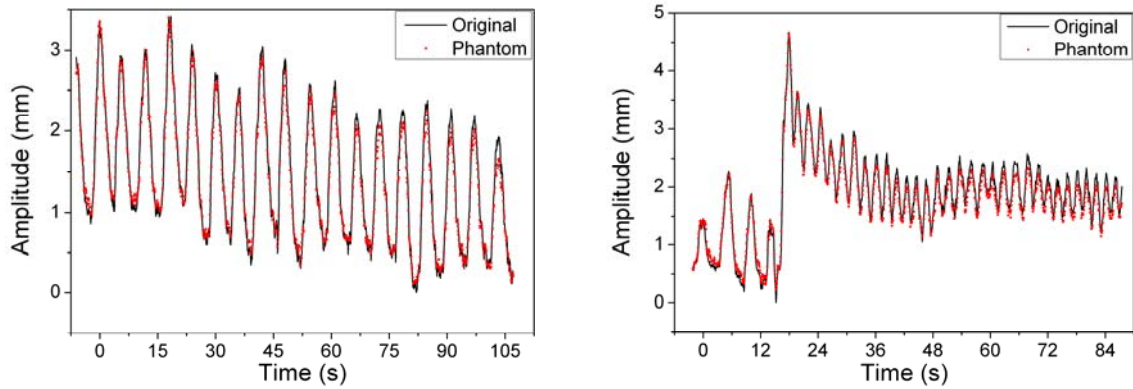


**Figure 3.8:** The original breathing signal of the volunteer (black line) compared with the breathing signal of the phantom (red squares) for a regular (left) and a faster irregular (right) breathing pattern.

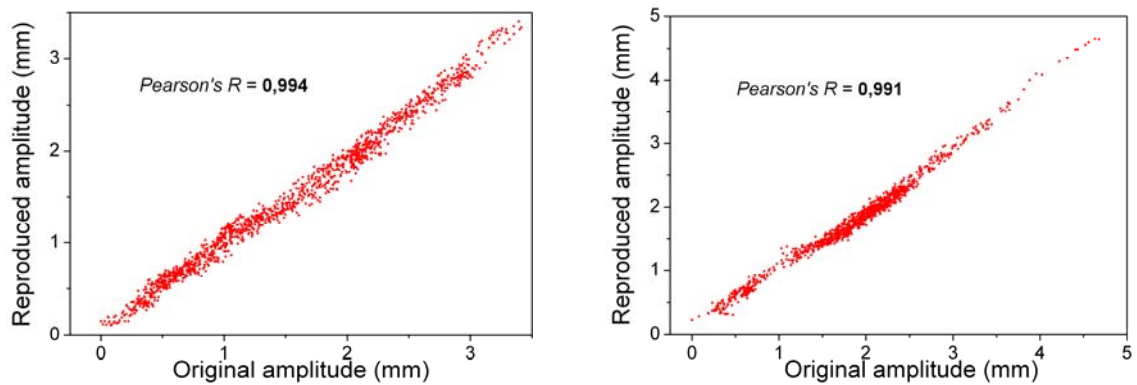


**Figure 3.9:** Correlation between the volunteer's original and the simulated breathing reproduced by the phantom for both a steady (left) and an irregular respiration pattern (right). Both coefficients were quite high.

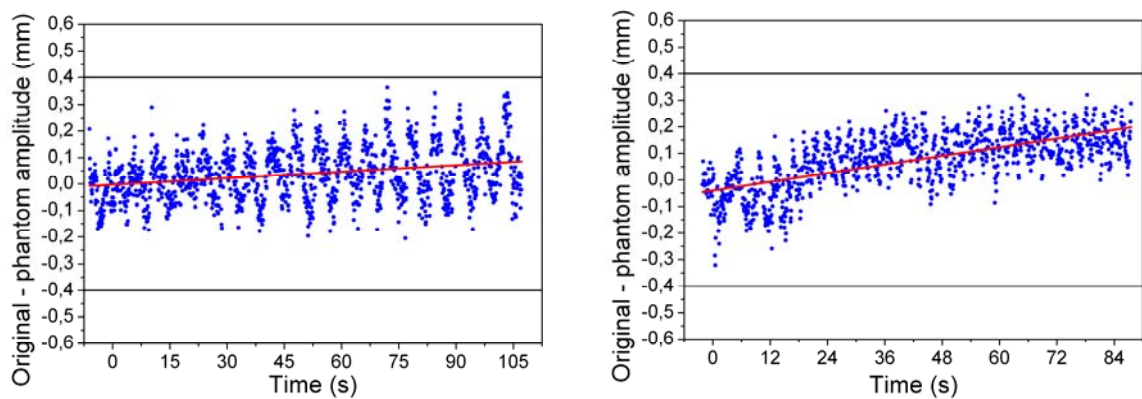


**Figure 3.10:** Difference between original (volunteer) and phantom signal was less than  $\pm 0.4$  mm for a regular (upper graph) and an irregular breathing pattern (bottom graph). Linear fits to the data reveal a minor air leak of the air pump system.

## *Generating 4D-CT images*

Several tests around the CT and the 4D-CT technique were carried out. They included the use of the CT-console to incorporate the breathing information into the CT. Also the feasibility of using GateCT system to produce a breathing signal for 4D-CTs was tested. Once this was done, the EBMS signals were again compared (as in section 2.4), but this time a periodical motion was used instead and some additional breathing file parameters were reviewed. An analysis of the sampling behaviour and stability of each system is shown, followed by an evaluation of the stability of the couch movement as it travels into the CT scanner. Finally there is a subsection dedicated to the 4D-CTs produced by each EBMS signals. In there, the trajectory of the tumour is analysed with help of the CT images reconstructed and also the influence of different breathing file parameters in the CT-images is addressed.

### **4.1 Materials and methods**

#### **4.1.1 Including the EBMS signal**

The inclusion of breathing information for 4D-CT imaging is done through the CT-console. The console also allows the management of the CT-parameters, as well as the reconstruction and data transfer protocols.

The Siemens CT-console running the commercial software (Somaris/5 Syngo CT 2007S, Sensation Open VB30B) obtains a third vendor breathing signal, directly through its proprietary interface. The signal is displayed in real-time only in the CT-console (figure 4.1). After the scanning process is over, the tags can be deleted, added or disabled (in the case e.g. of an irregular breathing pattern or when the patient coughs). The lower axis displays the time values, but the resolution is too small to allow a fine tuning of the tags. The breathing information remains stored at the reconstruction PC together with the raw data of the CT-acquisition.

For EBMS comparison, reconstructing the same CT-raw data, but with different breathing signals is possible. This can be achieved via the open interface of the CT which allows several reconstructions and importing different breathing files.

Image reconstruction is done with a local amplitude-based sorting algorithm (Wink et al. 2005), for which the breathing signals are divided into inspiration and exhalation parts with help of the tags. The acquired projections are then sorted according to a clinical protocol with eight different amplitudes percentages. These were: 20, 25, 50 and 75% of the inspiration and at 100, 70, 40 and 0% of exhalation phase.

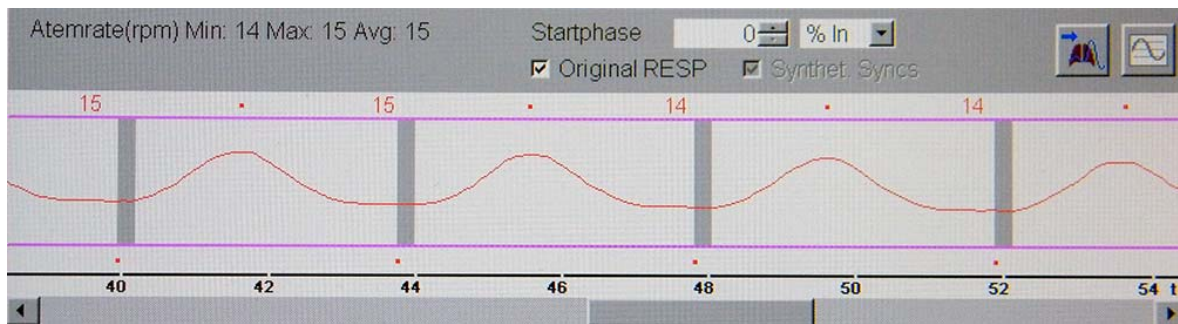


**Figure 4.1:** CT-console view of the breathing signal for a retrospective reconstruction. Tags are displayed as red dots. For each breathing cycle, the grey time window encloses the nearest point, which satisfies the selected amplitude percentage (in this case 0% inspiration).

#### 4.1.2 Testing GateCT

As the GateCT system was a new hardware at the clinic, some interfacing was required, at installation time. To ensure that the breathing signal provided had the necessary information required by the 4D-CT, the following test was performed. Three CT acquisitions were done as summarised in table 4.1: The first with a normal 3D-CT (no motion compensation) and with the phantom not moving (static). The second again, a normal 3D-CT, but this time, the phantom was moving. And finally a 4D-CT, while the phantom was moving. The CT parameters used are presented in table 4.2.. The idea behind this is that a good 4D-CT image should resemble an image of the 3D-CT without phantom motion and the artefacts presented in the 3D-CT with phantom motion should disappear (or at least be greatly diminished).

**Table 4.1:** Summary of the three studies compared. The 4D-CT was made with the GateCT system only.

Imaging technique	Phantom status
3D-CT	Static
3D-CT	Moving
4D-CT	Moving

**Table 4.2:** CT protocols' parameters used in this work. The 4D-CT parameters are also used in the studies made in subsection (4.1.6).

Parameter	Units	3D-CT	4D-CT
Voltage	kV	120	120
Effective current	mAs	300	330
Slice thickness	mm	5	3
Slice collimation	mm	1.2	1.2
Number of slices	–	24	24
Gantry rotation time	s	1.0	0.5
Pitch	–	0.85	0.1
Reconstruction kernel	–	B40s Mittel	B10f

### 4.1.3 Comparison of monitor signals

For the systematic study of both monitoring systems using the phantom, the following curve was run by the motor controlling the air pump as well as the motor moving the lung tumour motors:

$$z(t) = A \cdot \sin(\omega t)^{2n} + z(t_0) \quad \text{with } \omega = \pi/T \quad (4.1)$$

where  $z(t)$  and  $z(t_0)$  is the motor position at a given time  $t$  and  $t_0$ , respectively.  $A$  is the peak-to-peak amplitude, and  $T$  the duration of the breathing cycle. The parameter  $n$  describes the shape of the curve. Lujan *et al.* (1999) demonstrated that a curve like equation (4.1) represented the average phase and amplitude motion for a treatment with several fractions in the case of the liver. George *et al.* (2005) went a step further and proved the use of this motion to study lung patient breathing motions and found a high correlation between their results and the model, when the value  $n$  was equal to 1 or 2.

The parameters of the curve  $A$ ,  $T$  and  $z(t_0)$  are given by the user at runtime. To represent an “average” breathing cycle, the following values presented in table 4.3 were chosen. This selection of motor parameters took into consideration equation 1.16, to avoid undersampling and missing data projections at the CT-reconstruction.

**Table 4.3:** Parameters used to recreate a regular breathing movement in the phantom

Parameter	Motor air pump	Motor tumour
Breathing cycle duration (s)	4	4
Peak-to-Peak amplitude (mm)	15	15
Initial displacement $z(t_0)$ (mm)	2.5 or 7.5	2.5
Value “ $n$ ”	2	2

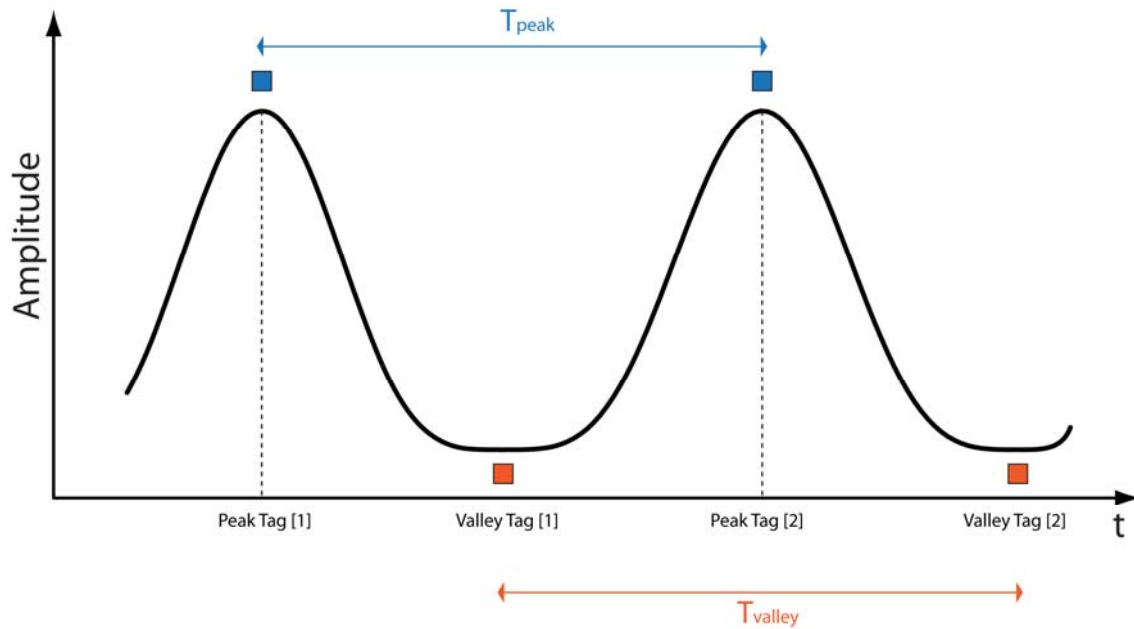


**Figure 4.2:** Peak and valley periods ( $T_{peak}$  and  $T_{valley}$ ) are calculated from the tags reported by each system.

While running this motion pattern, simultaneous measurements with both monitoring systems were performed. To compare the breathing curves from the two monitoring systems, a synchronization was performed using the beam On/Off signal stored in each ASCII-file. For each system the first amplitude value of the ASCII-file that possessed a beam-On sign was searched and its corresponding time was set to zero. Then all the remaining values were modified accordingly. Assuming that the radiation detectors worked perfectly and with negligible delay, only a small systematic error equal to or smaller than the monitor system’s sampling rate is expected.

For each monitoring system periods of time between two adjacent peak tags ( $T_{peak}$ ) and between two adjacent valley tags ( $T_{valley}$ ) were calculated from the breathing curves (figure 4.2).

In addition, a nominal position of the valley tag was defined as the middle point between two neighbouring peak tags or;

$$\text{Nominal Valley Tag } [i] = \frac{\text{Peak Tag } [i+1] + \text{Peak Tag } [i]}{2} \quad (4.2)$$

and it was used to calculate the temporal difference between the actual and the nominal valley tags, which was named as  $\Delta T_{valley}$  or;

$$\Delta T_{valley} [i] = \text{Valley Tag } [i] - \text{Nominal Valley Tag } [i] \quad (4.3)$$

which is a measure of how precise the valley detection is for both breathing systems. A  $\Delta T_{valley} = 0$  will indicate that the valley tag is located exactly between two peaks (as expected for a regular curve).

#### 4.1.4 Evaluation of sampling intervals and rates

The sampling interval or the time difference between two consecutive amplitude measurements,  $t[i+1] - t[i]$  can be a stable value or it can vary in one single measurement and this may have an influence on the reconstructed 4D-CT. Therefore, to visualise all sampling intervals at once, a histogram of such values registered during eight different CT-acquisitions will be calculated from both AZ-733V and GateCT breathing files. Given that the open interface is made under the specifications for the RPM system, a breathing file from this system was also analyzed as an example (original data kindly provided by C. Bert). A bin size of 1 millisecond was used for all histograms.

To characterise each system the mean of the sampling interval was calculated for each measurement as well as the mean sampling rate (which is the inverse value of the sampling

interval). The latter was compared with the nominal sampling rate written at the header of each EBMS ASCII-file.

#### 4.1.5 Influence of CT-couch movement on GateCT signal

Due to the small amplitude of the patient's external motions, any small additional source of movement may have considerable influence in the shape of the detected breathing signal. As a result, any tilting or sinking of the CT-couch may have a noticeable effect in the breathing signal detected by the GateCT-system. Due to the presence of a baseline shift in preliminary experiments with the GateCT-system, the displacement and tilt of the CT-couch, while moving into the CT-bore, was investigated.

The experimental setup included a laser-pointer fixed to the couch's surface. The couch angle plus the angle of the laser with the horizontal line, was named  $\alpha$  as shown in figure 4.3. A millimetre paper was posted on the opposite wall to the CT. The experiment consisted in displacing the couch a fixed distance step  $\Delta x$  and then to register the laser's dot coordinate  $\Delta y$  in the millimetre paper.

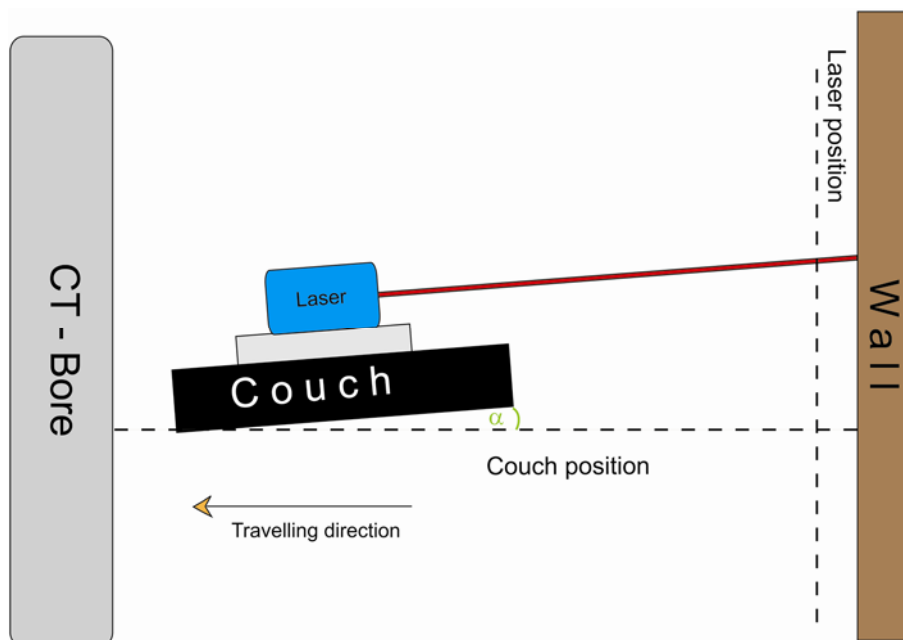


**Figure 4.3:** Setup to test, if the couch inclination varied, while travelling into the CT, with or without the phantom on it.

Three different outcomes can describe the laser's position, whilst moving the CT-couch:

1. The laser remains at the same spot all the time, meaning that the couch moves with an inclination of  $\alpha$  into the CT bore.
2. The laser's dot moves with fixed  $\Delta y$  intervals, following the trigonometric equation,

$$y = x \cdot \sin(\alpha) \quad (4.4)$$

meaning that the couch moves horizontally and the angle  $\alpha$  does not change.

3. The laser's dot moves with irregular  $\Delta y$  intervals, following a non linear curve, meaning that the angle  $\alpha$  varies.

As weight placed on the table may play a role, the experiment was carried out with and without the phantom on the couch. The phantom weighs about 20 kg. The fixed distance step  $\Delta x$  was 10 cm and total couch displacement was 160 cm. The whole experiment was repeated 3 times with each configuration and the mean  $\Delta y$  value was calculated.

#### **4.1.6 Comparison of 4D-CT reconstructions**

This subsection includes important results for this work as the EBMSs and the phantom (chapters 2 and 3, respectively) were tested thoroughly just to arrive to this experiment. The first part present the original state of the 4D-CTs produced by each EBMS and the last part shows how several changes to the signals parameters influence the final 4D-CT images.

##### **4.1.6.1 Analysis of tumour trajectory**

To compare the reconstructions made with the signal from the two breathing monitoring systems, sagittal images through the tumour centre were evaluated from 8 different 4D-CT scans, each one acquired on different days. A fiducial marker (X-Spot, Beekley Corporation, Bristol, CT, USA) with a diameter of 1.5 mm (figure 4.4) placed at the centre of the tumour was located in each reconstructed images from each of the eight percentage amplitudes defined by a clinical protocol (see 4.1.1).

The centroid coordinates of the pixels corresponding to the fiducial marker were determined with help of the image processing software ImageJ (National Institutes of Health, USA, “public domain”). All measurements were performed in a “bone window” (defined in table 1.1). As the marker is made of metal, it could be easily identified in the images. Motion artefact recognition on the other hand was performed with the lung window as more details of the tumour itself were available. For this part, the images used as representatives of the whole data set were those obtained at 0% amplitude of the exhalation part.



**Figure 4.4:** Fiducial marker made of metal, used to determine tumour trajectory.

The original CT-images are DICOM (Digital Imaging and Communications in Medicine) files and have 512 x 512 pixels, covering the 500 mm FOV meaning that each pixel covers about 0.98 mm. A file named DICOMDIR allows reading the files in the proper order. But as the ImageJ software could not open the DICOMDIR file an intermediate step was made using the software syngo-fastView (Siemens, Erlangen, Germany). This software allows a comprehensive view of the data, but it also adds extra information, thus forming a new bigger image and therefore changing the pixel to millimetre ratio. As the images were going to be analyzed with ImageJ, a new conversion value was calculated and the result, 1.7476 px/mm, was later used for all fiducial marker coordinates calculations.

The measured coordinates of the centroid of the fiducial marker of the 0% exhalation amplitude were set as zero and the coordinates from the other percentage amplitudes were adjusted accordingly. For the sake of completeness the 0% exhalation amplitude data will be plotted again, as a 9<sup>th</sup> point.

#### 4.1.6.2 Influence of monitor signal parameters

As the reconstructed coordinates of the fiducial were significantly different for both breathing monitoring systems, the influence of several breathing curve parameters on the reconstructed images were investigated. For this, the breathing curves were manipulated and after each manipulation, the 4D-CT reconstruction as well as the evaluation of the marker coordinates were repeated. The selection of the manipulated parameters was guided by the differences observed between the breathing curves from both monitoring systems. Roman numerals (i, ii, iii, etc.) are going to be used to differentiate each manipulation and will also be used afterwards to refer to the specific method.

The most obvious differences between the breathing curves of the AZ-733V- and the GateCT-system were: i) the baseline shift, ii) the higher noise level, and iii) higher variability of the valley tag position in the GateCT-system. To study the influence of these differences, the GateCT curve was manipulated by: **i)** removing the baseline drift, **ii)** smoothing of the curve, and **iii)** by correcting the valley tags' positions to their nominal values as explained in the next paragraphs:

*i. Removing baseline drift:*

Assuming that the amplitude of the peaks produced by the motion of the phantom's skin was always the same value, the main cause of different peak amplitudes would be the baseline drift. In an attempt to reduce the drift, a linear fit of the peak amplitude values was calculated. By subtracting the linear fit curve from the original breathing curve, the baseline drift can be removed or at least largely diminished.

*ii. Smoothing of the curve:*

The GateCT file was imported into OriginPro 8.5. Academic software and a Fast Fourier Transform (FFT) filter was applied to the signal. The FFT filter is an optimised algorithm based on the Discrete Fourier Transform, which is normally used for Spectral Analysis. The signal is separated in several frequencies and it is possible to eliminate certain frequencies higher than a given value, known as cut-off frequency. As the noise in a signal can be regarded as unwanted high frequencies, the use of a cut-off frequency can be considered as the process to eliminate noise or to smooth the input signal.

*iii. Improvement of valley tagging precision:*

Assuming that the peak tags written in the ASCII-file are correctly located close or exactly at the highest amplitude value detected by the GateCT-system, the nominal valley tag between them was calculated. The valley tags were then manually modified and rewritten to the closest timestamp available, which minimises the difference between the nominal and the new valley tags, according to equation 4.3.

Since the previously studied parameters did not explained the differences found between the reconstructed trajectories, the sampling interval regularity and the accuracy of the sampling rate value in the ASCII-header were also investigated. The following manipulations were made to these parameters both in the GateCT and AZ-733V files:

- iv. Linear interpolation of the curve to a regular or irregular sampling interval, and,*
- v. modifying the sampling rate in file header to the exact average sampling rate or to an approximated (but inaccurate) value.*

This was performed in the following way. Starting with the GateCT file, the manipulations were carried out in three steps, summarised in table 4.4:

In a 1<sup>st</sup> step, the original curve from GateCT was first interpolated to a regular sampling rate (i.e. to the average value obtained on this particular measurement), but the inaccurate value of the sampling rate in the ASCII file-header was left unchanged.

In a 2<sup>nd</sup> step, the original irregular sampling intervals were left unchanged, but the accurate mean sampling rate (12.17 Hz) for this measurement replaced the inaccurate original value written at the header.

Finally, in a 3<sup>rd</sup> step, both the originals sampling intervals and rate were changed for a regular and an accurate one.

**Table 4.4:** Summary of the modifications made to the GateCT-signal. The value of the interval used for interpolation and the value written into the header's nominal sampling rate are between parentheses.

<b>GateCT-signal</b>	<b>Sampling intervals (ms)</b>	<b>Sampling rate value (Hz)</b>
Original	Irregular	Inaccurate (13.00)
1 <sup>st</sup> step	Regular (82.19)	Inaccurate (13.00)
2 <sup>nd</sup> step	Irregular	Accurate (12.17)
3 <sup>rd</sup> step	Regular (82.19)	Accurate (12.17)

To confirm the dependence of the fiducial marker trajectories on these two parameters, a similar procedure was applied to the AZ-733V curve. These changes are summarised in table 4.5 and explained in the next three paragraphs:

*First*, to discard any effect from different temporal resolutions, the AZ-733V-curve was first linearly interpolated to the average sampling interval of the GateCT original measurement (82.19 ms) and the corresponding mean sampling rate (12.17 Hz) was written in the header.

Then, in a *second* step, the sampling intervals from AZ-733V were replaced by the sampling intervals from an original GateCT measurement, which were irregular distributed (see figure 4.9h) and the amplitudes were then linearly interpolated to these new time stamps. In this case, the sampling frequency in the ASCII-header was also set to the correct mean rate value.

In a *third* step, the interpolated AZ-733V-curve was maintained at a regular mean sampling rate (as in the *first* step), but the sampling frequency in the ASCII header was set to an inaccurate value (13 Hz).

**Table 4.5:** Summary of the modifications made to the AZ-733V-signal. The interval used for interpolation and the value written into the header's nominal sampling rate are between parentheses.

<b>AZ-733V-signal</b>	<b>Sampling intervals (ms)</b>	<b>Sampling rate value (Hz)</b>
Original	Regular (25.00)	Accurate (40.00)
<i>First</i> step	Regular (82.19)	Accurate (12.17)
<i>Second</i> step	Irregular	Accurate (12.17)
<i>Third</i> step	Regular (82.19)	Inaccurate (13.00)

Finally, the *vi) Influence of the magnitude of a fixed sampling rate* on the marker's trajectory was investigated. Interpolation was made with several sampling intervals as described in table 4.6 and special care was taken to have a correct header value in each ASCII-file. The deviation of the reconstructed trajectory to an ideal (or ground truth) trajectory was also addressed. Files number 2, 3 and 4 were generated by VisionRT Ltd. using an improved algorithm, developed on the basis of the previous results of this study.

**Table 4.6:** Fixed sampling rate values with their corresponding sampling intervals used to resample the original GateCT breathing signal.

#	Sampling rate (Hz)	Sampling interval (ms)
1	12.17	82.2
2	12.50	80.0
3	13.26	75.4
4	15.00	66.7

## 4.2 Results

### 4.2.1 Testing GateCT

An axial view of the reconstructed data through the centre of the tumour clearly shows the differences, when the tumour was static (figure 4.5a) and when it was moving (figure 4.5b), for the case of conventional 3DCTs. Typical motion artefacts appeared in the presence of tumour movement. The motion artefact was largely removed and the sharpness of the tumour was restored by the 4D-CT protocol (figure 4.5c), therefore proving the feasibility of using the GateCT system to produce 4D-CT.

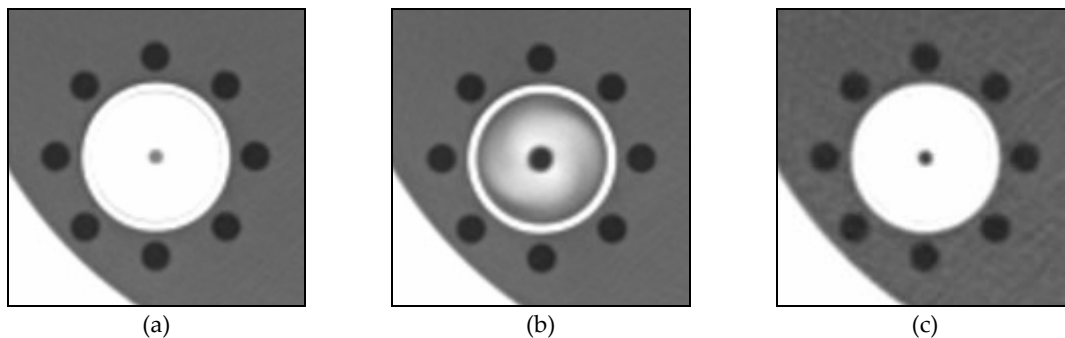


**Figure 4.5:** Tumour images for three different CT-scans: 3D-CT with phantom static (a) 3D-CT with phantom moving (b) and 4D-CT scan with phantom moving (c). The 4D-CT used the signal from the GateCT-system.

## 4.2.2 Comparison of monitor signals

Now that two surrogate respiratory systems are capable of delivering the information required for 4D-CT reconstruction, the next step was to analyse the respiration signals. Figure 5.6a compares the GateCT-amplitude signal with the pressure-signal of the AZ-733V-system and the original cosine-like curve given to the motors (equation 4.1), before the CT-scan procedure started. Both monitor signals were quite similar and reproduced the given curve nicely, however the AZ-733V-amplitude depended heavily on how tightly or loose the belt was fastened around the phantom and this was reflected in the shape of the curve (figure 5.6b). Correlation with the cosine-like curve was  $r=0.984$  for the AZ-733V and  $r=0.999$  for GateCT.

During the CT-acquisition, the respiratory signals remained in phase. On the other hand, one noticeable change is seen in figure 4.7, where the GateCT-signal in this particular example, shows a baseline drift of about 2 mm for a 20 cm length scan, while there is no drift for the AZ-733V system. Therefore as expected, the correlation of the GateCT signal with the motor curve decreased slightly, yet it continued to be very high ( $r=0.899$ ) and the AZ-733V correlation ( $r=0.986$ ) can be considered identical to its pre-scan value. To be able to compare both shapes, the AZ-733V-curve was normalised to the GateCT signal, using the maximum (minimum) value of GateCT registered just before the CT-Scan acquisition started.

The time stamps of the tags marking a signal peak were investigated and indicated that peak recognition was highly accurate and reproducible in both systems as shown for each CT-scan in table 4.7. The mean temporal difference for all scans between corresponding peaks of the GateCT and the AZ-733V-system was  $4 \pm 33$  ms and the maximum difference observed was only 77 ms.

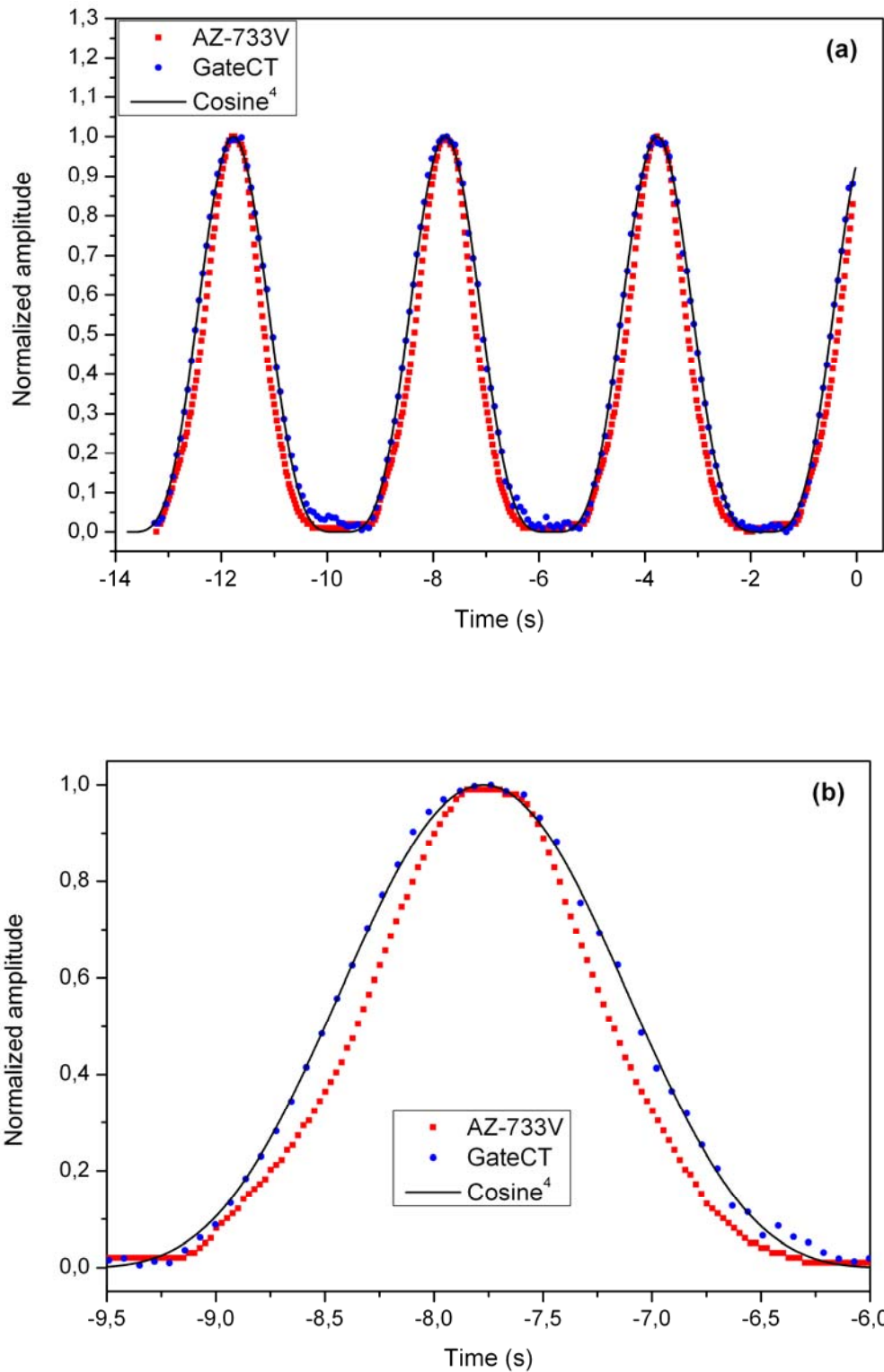


**Figure 4.6:** AZ-733V and GateCT curves (red and blue symbols, respectively) compared with the original curve given to the motors (black line) before the CT-scan started (a). The detailed view (b) shows that the AZ-733V system could not reproduce the cosine-like curve as well as the GateCT system.

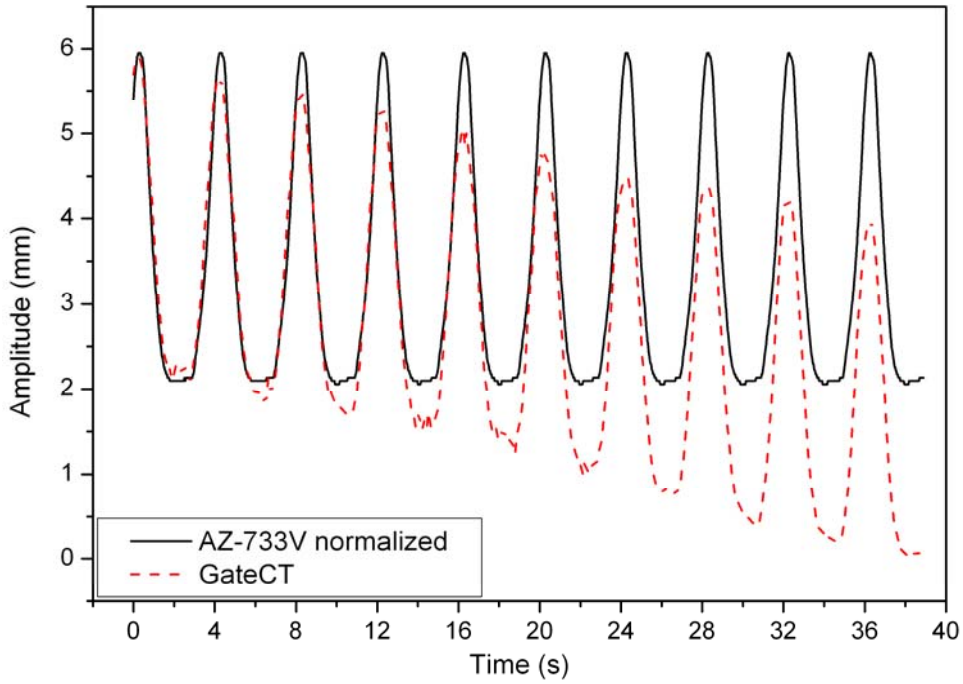


**Figure 4.7:** Breathing signals of the phantom recorded with both respiration monitoring systems during the CT-scan. A baseline drift can be seen on the GateCT signal. Note: To enhance viewing, the peak-to-peak amplitude of the AZ-733V system, which measures a pressure difference, was normalised to the GateCT peak-to-peak amplitude in millimetres.

**Table 4.7:** The low temporal peak detection difference between the GateCT and AZ-733V systems, measured for eight different scans indicates that both systems detects peaks at almost the same time.

Scan #	Tag peak difference mean $\pm$ SD (ms)
1	-31.71 $\pm$ 26.47
2	30.50 $\pm$ 27.32
3	12.63 $\pm$ 35.12
4	8.10 $\pm$ 32.81
5	-7.22 $\pm$ 33.43
6	17.50 $\pm$ 27.96
7	-7.44 $\pm$ 27.79
8	-0.22 $\pm$ 26.19

The Peak-to-peak tag period was highly regular on both systems as seen in table 4.8 ( $T_{peak}$ ) in the second and fourth columns. Valley recognition in the other hand was difficult for both systems,

given the flat shape of valley region, where several values share the minimum value. Nevertheless the time between two adjacent valley tags ( $T_{valley}$ ) was fairly regular for both systems. The difference between the time stamps of where the “minimum” was actually located and where the assigned valley tag position was written in the signal file is given in the  $\Delta T_{valley}$  columns. While the AZ-733V-system located the valley tags with a high regularity before the “minimum” value, the GateCT system located them afterwards and showed a larger standard deviation (SD).

The mean difference between the X-Ray ON time registered by GateCT and AZ-733V systems was  $10 \pm 29$  ms, meaning that both systems register the radiation at almost the same time.

**Table 4.8:** Mean time period between adjacent peaks and valley tag positions ( $T_{peak}$  and  $T_{valley}$  respectively). Valley tagging precision (time difference between actual and nominal valley tag position)  $\Delta T_{valley}$  is also shown for eight different scans.

#	AZ-733V mean $\pm$ SD (ms)			GateCT mean $\pm$ SD (ms)		
	$T_{peak}$	$T_{valley}$	$\Delta T_{valley}$	$T_{peak}$	$T_{valley}$	$\Delta T_{valley}$
1	$3996 \pm 10$	$3996 \pm 19$	$-295 \pm 10$	$3988 \pm 40$	$4015 \pm 294$	$332 \pm 152$
2	$4003 \pm 20$	$4000 \pm 0$	$-243 \pm 6$	$3999 \pm 45$	$4038 \pm 283$	$151 \pm 207$
3	$4000 \pm 0$	$4003 \pm 16$	$-244 \pm 11$	$3995 \pm 44$	$4012 \pm 182$	$225 \pm 125$
4	$4000 \pm 0$	$4000 \pm 18$	$-330 \pm 11$	$4000 \pm 49$	$4017 \pm 347$	$167 \pm 186$
5	$4000 \pm 0$	$4009 \pm 30$	$-461 \pm 25$	$4003 \pm 54$	$4053 \pm 73$	$227 \pm 134$
6	$4004 \pm 9$	$4000 \pm 0$	$-273 \pm 4$	$4004 \pm 47$	$3994 \pm 158$	$237 \pm 97$
7	$4000 \pm 0$	$4000 \pm 13$	$-322 \pm 8$	$4009 \pm 39$	$4000 \pm 122$	$199 \pm 83$
8	$4000 \pm 0$	$3996 \pm 9$	$-303 \pm 9$	$4004 \pm 46$	$4028 \pm 276$	$181 \pm 156$

### 4.2.3 Evaluation of sampling intervals and rates

The investigated histograms show variability in the sampling intervals between systems. On one hand, the histograms of the AZ-733V-system showed that the sampling interval was 25 ms for all measurements (e.g., figure 4.8a). The histograms from the RPM system showed a similar behaviour (e.g., figure 4.8b). Even though its values varied (mean sampling interval 33.4 ms), its standard deviation was quite low (1.9 ms), pointing out that both systems have a stable sampling rate, which was calculated as 40 and 30 Hz, for AZ-733V and RPM, respectively. These values matched exactly the ones written at each ASCII-file header.

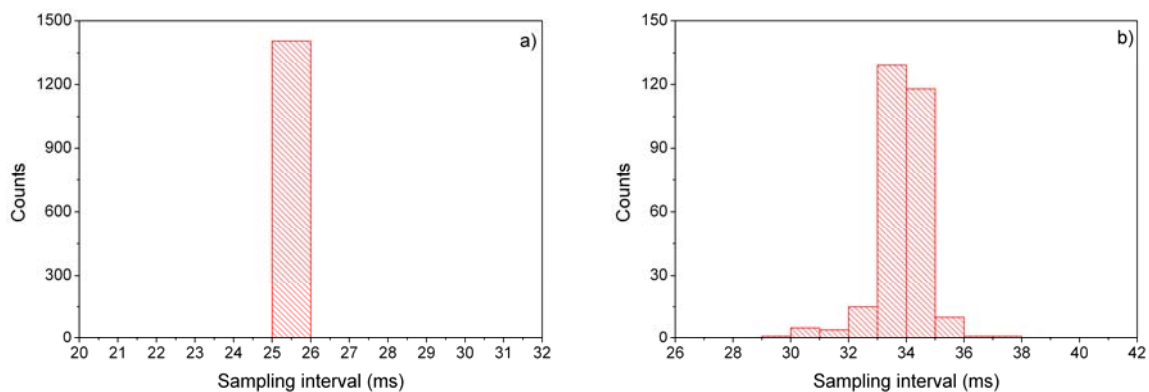


**Figure 4.8:** Distribution of the sampling intervals for AZ-733V (a) and RPM system (b).

On the other hand, the sampling intervals of the GateCT system varied heavily both intra and inter measurement as observed in figure 4.9. For example, the sampling intervals in figure 4.9 h) varied between 59.9 and 116.3 ms, meaning that sometimes the system required almost twice the fastest time achieved to process a new amplitude from the ROI. This high variability is clearly reflected on the shape of the histograms. Only figure 4.9 b), e) and f) present a better stability on the sampling interval.

The mean sampling interval together with the mean and nominal sampling rate for each GateCT measurement [from a) to h)] are presented in table 4.9. The magnitude of the mean sampling intervals was about three times higher than the values of the AZ-733V.

The nominal sampling rate written in the header by the GateCT software, unlike the cases of the AZ-733V and RPM systems, was only an approximation of the calculated mean sampling rate and in some cases [a), b), g) and f)] differed considerably.

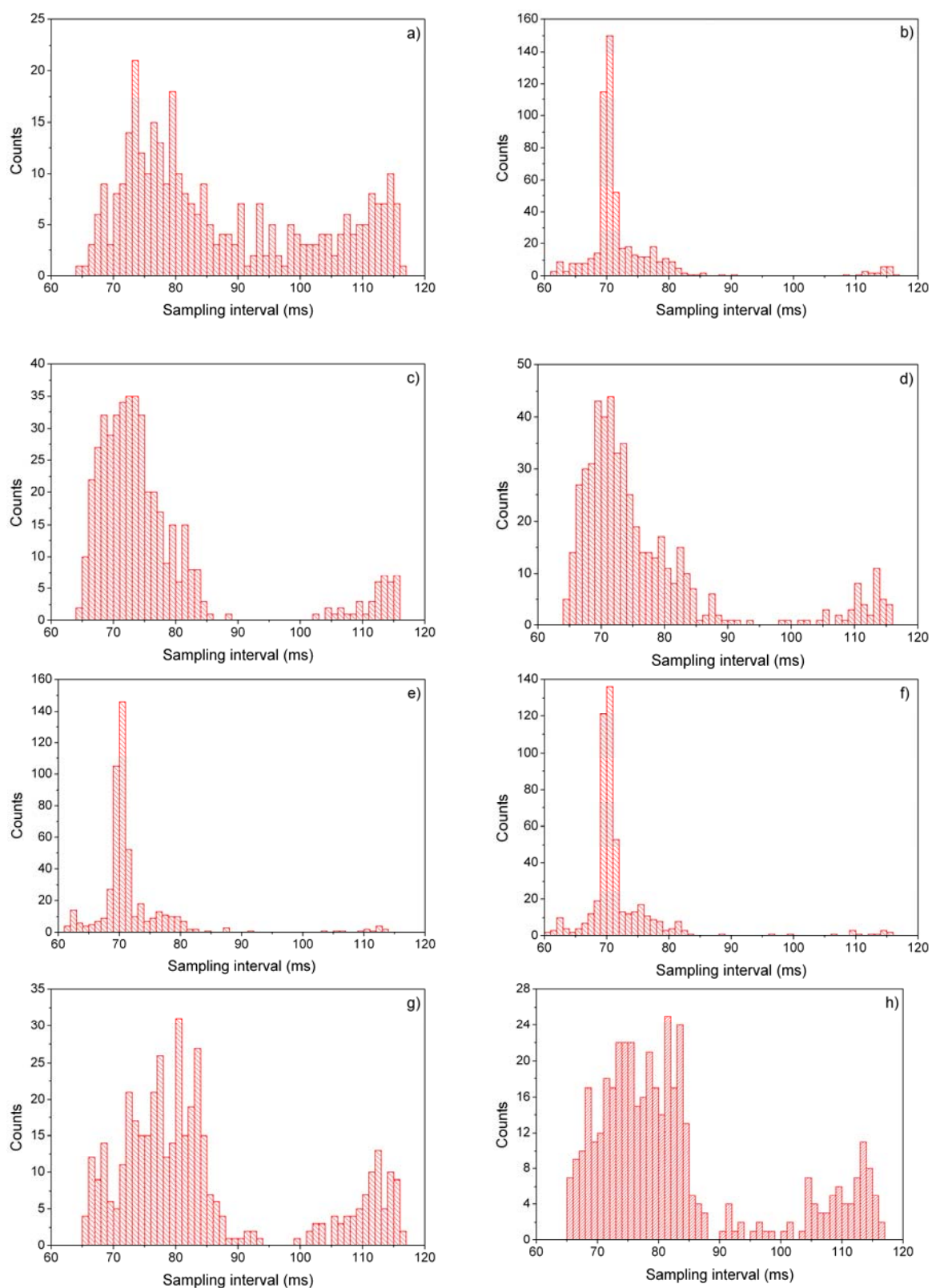


**Figure 4.9:** Distributions of the sampling intervals for the GateCT-system measurements. Values in the histogram (h) were selected as “worst case” for further studies.

**Table 4.9:** Mean sampling intervals and rates calculated from measurements (a) to (h) together with the header nominal sampling rate written in each ASCII file.

GateCT measurement:	(a)	(b)	(c)	(d)	(e)	(f)	(g)	(h)
Mean sampling interval (ms)	86.59	72.65	76.06	76.22	71.59	71.65	83.74	82.19
Mean sampling rate (Hz)	11.16	13.76	13.15	13.12	13.97	13.96	11.94	12.17
Header nominal sampling rate (Hz)	12.00	13.00	13.00	13.00	14.00	14.00	13.00	13.00

#### 4.2.4 Influence of CT-couch movement on GateCT signal

Figure 4.10 shows the difference between the laser position observed  $y_{laser}$  and the laser position calculated with a straight line (equation 4.4)  $y_{\sin\alpha}$ . The shape of the curves indicates that case 3 was the correct assumption. Had the couch had travelled horizontally as in case 2, the points in the graph would have followed horizontal lines. The experiment proves that the couch tilts as it travels into the CT-bore. The graph also states a clear difference between the CT-couch with or without weight, thus explaining the source of the baseline shift recorded by the GateCT system, presented previously in figure 4.7.

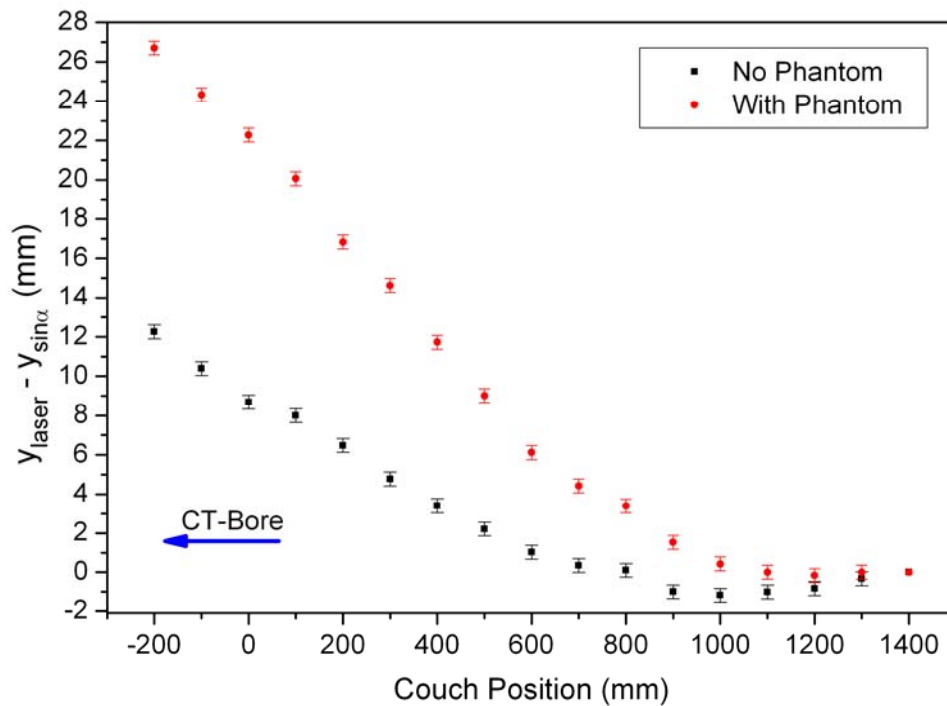


**Figure 4.10:** Difference of the measured and calculated laser positions as the couch travels into the CT-bore with- and without the phantom on it. It reveals a non linear dependence of the couch angle with the couch position.

## 4.2.5 Comparison of 4D-CT reconstructions

### 4.2.5.1 Analysis of tumour trajectory

The trajectory of the fiducial marker obtained from eight different amplitude percentages (the 9<sup>th</sup> point is the 0% exhalation point repeated) was analysed for both the 4D-CT reconstructed with the AZ-733V and the GateCT system. Figure 4.11 shows a typical result for this experiment.

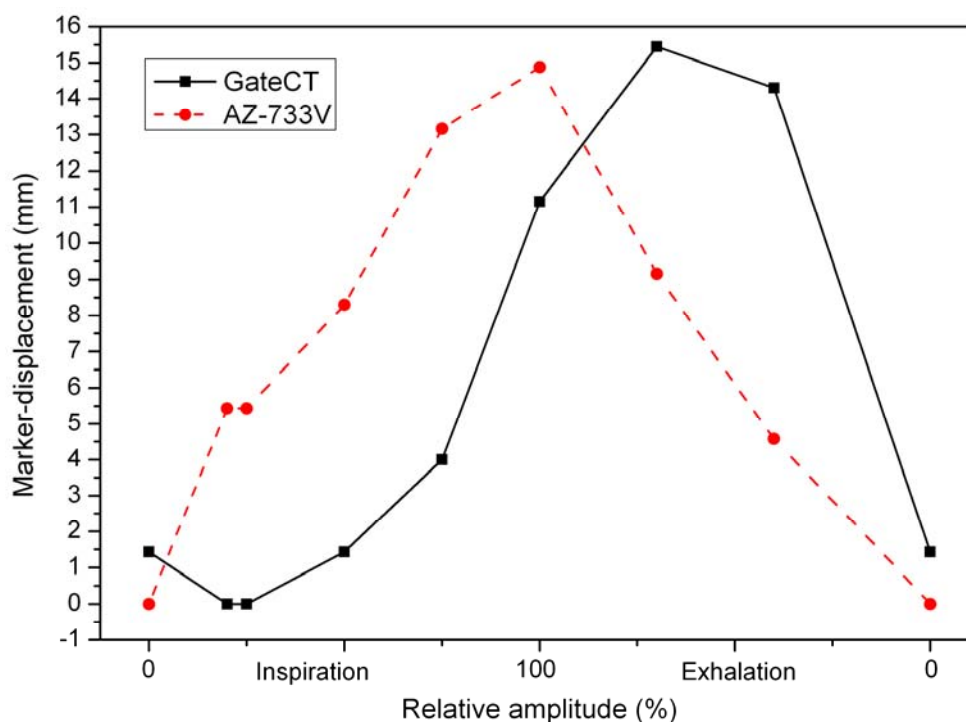


**Figure 4.11:** Example of the trajectory of the fiducial determined from the 4D-CT-reconstructions using the AZ-733V- or the GateCT-system, respectively.

It can be seen that for given breathing amplitude, large differences (up to 9.7 mm) in the fiducial centroid position were encountered, depending on the system used. Separate evaluation of the 4D-CTs, revealed a good image quality for the AZ-733V system (figure 4.12a) and only small motion artefacts, which can be attributed to a finite temporal resolution of the CT-scanner. On the other hand, the 4D-CTs reconstructed with GateCT showed a variable image quality from experiment to experiment and from amplitude to amplitude percentage. Some images reconstructed with the GateCT-system had considerable artefacts, making it more difficult to identify the exact position of the fiducial marker. In some images, distortions of the shape of the spherical lung tumour were also seen (figure 4.12b). Nevertheless the peak-to-peak amplitude (15 mm) was found to be correctly displayed in both 4D-CT reconstructions. The uncertainty in the determination of the fiducial position was  $\pm 0.6$  mm for all measurements.

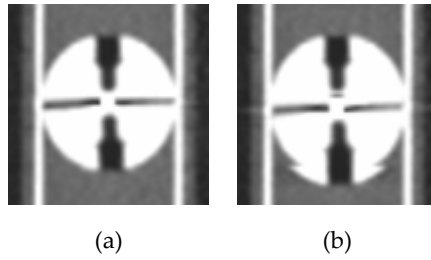


**Figure 4.12:** Images of the phantom's tumour reconstructed with the original AZ-733V (a) and GateCT(b) breathing signals. Motion artefacts are visible on the latter. To avoid manipulations, the actual picture size is shown.

#### 4.2.5.2 Signal's parameters modification

The effect of the baseline drift correction, the smoothing filter and the improvement of tagging on the GateCT signals are presented in figures 4.13, 4.14 and table 4.10, respectively. Drift correction maintained the shape of the curve to resemble the pre CT-acquisition breathing signal. The smoothing filter affected the lower amplitudes heavily, where the signal was noisier, as shown in the embedded graph, and the absolute tagging precision improved in one order of magnitude.

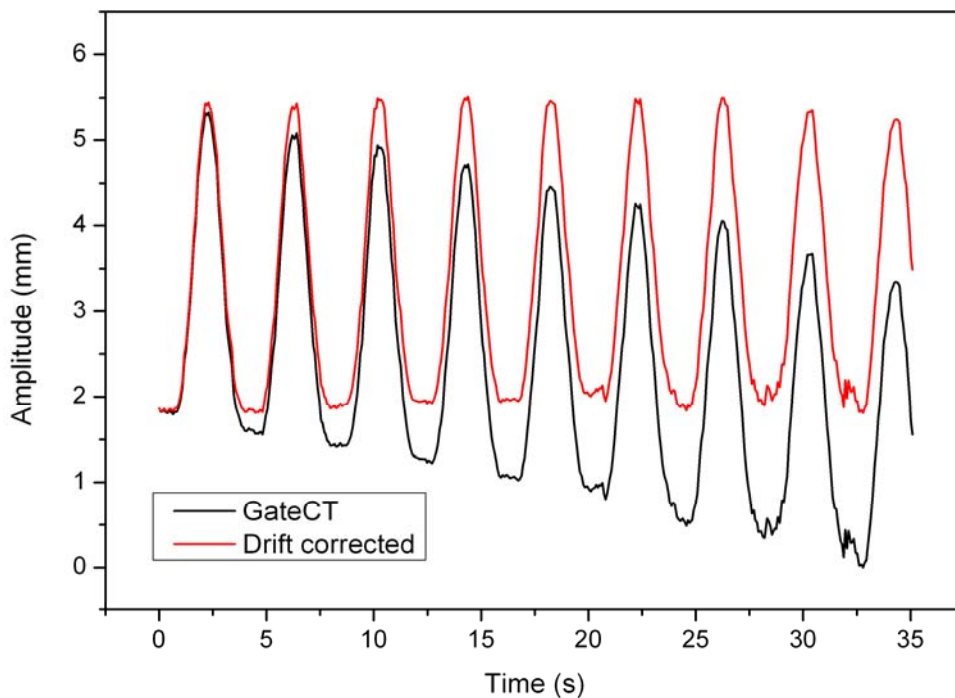


**Figure 4.13:** Original GateCT signal (black line) and the signal after baseline drift correction (red line).

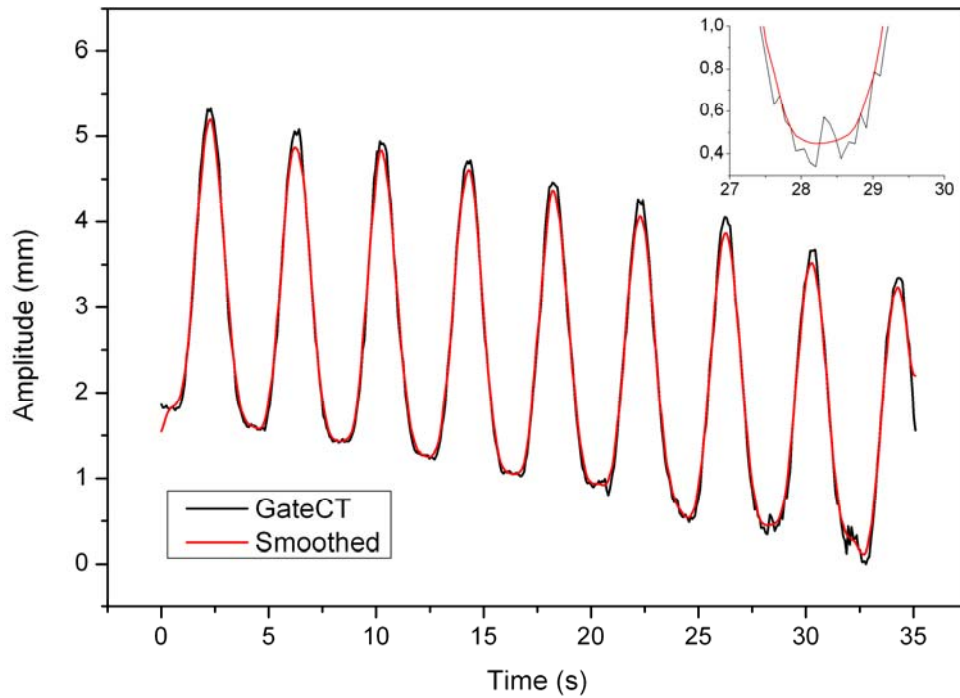


**Figure 4.14:** Original GateCT signal (black line) and the signal after FFT filtering. As seen in the zoomed graph, signal noise greatly reduced.

**Table 4.10:** Valley tagging precision for the GateCT-system, before and after valley tag correction.

GateCT curve	Mean $\Delta T_{valley} \pm SD$ (ms)
Original	181 $\pm$ 156
Valley tagging corrected	-16 $\pm$ 19

Even by, removing the baseline drift **(i)**, or smoothing **(ii)**, or correcting the valley tag positions to the “minimum” nominal value **(iii)** no significant change of the fiducial trajectory was observed, as seen in figure 4.15. The centroid coordinates were still showing the same significant differences encountered in the trajectory produced with the original GateCT and the images kept showing heavy motion artefacts. Only the images of the 0% amplitude of the exhalation part had minor improvements, when the smoothing filter was applied to the curve.

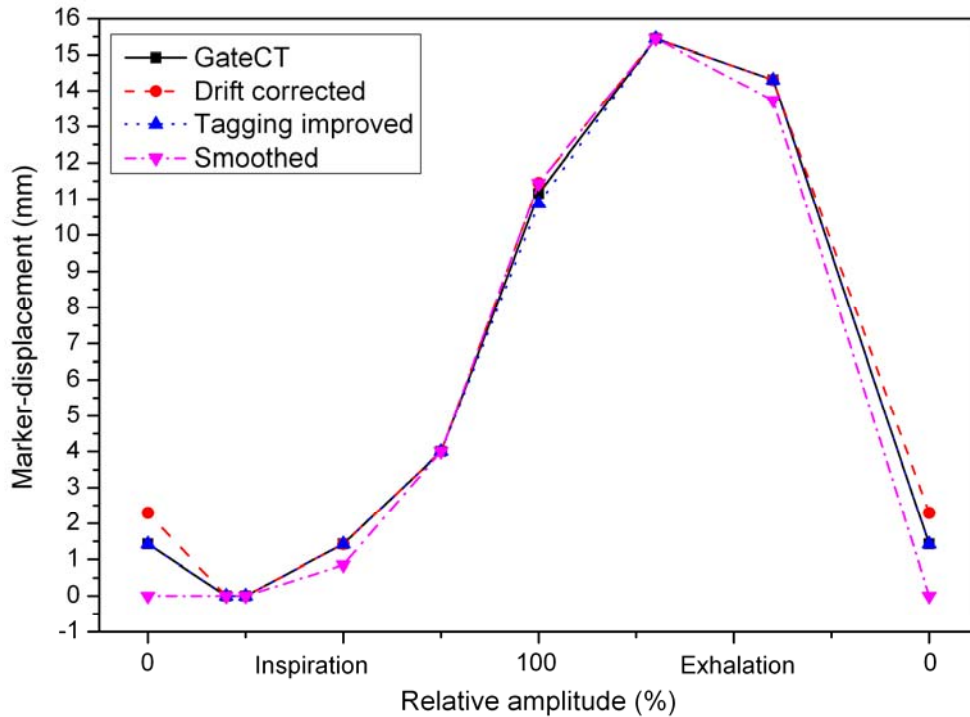


**Figure 4.15:** Influence of manipulations **i-iii)** of the GateCT-breathing curve on the positions of the fiducial marker. Other than at 0% amplitude exhalation with smoothing, no other significant influence was observed.

Once the influence of the most obvious parameters was already addressed, the attention turned to look into the time stamps, sampling rates and the ASCII-file headers and how their modification (as explained in methods **iv)** and **v)**) affected the trajectory of the fiducial in the 4D-CT.

Modifications of the GateCT file sampling intervals and rate showed to have a great impact on the fiducial trajectory. Here it was found that a great improvement was achieved when the sampling intervals were regular and the sampling rate was accurate. The trajectory of this GateCT modified this way agreed quite well with the AZ-733V-trajectory in almost all evaluated percentage amplitudes, as observed in figure 4.16.

When the AZ-733V file was manipulated instead, it was noticed that an interpolation to a lower frequency had no significant influence, while switching to irregular sampling intervals or to an inaccurate sampling rate in the ASCII-header severely distorted the positions of the fiducial marker and created artefacts in the reconstructed images. Figure 4.17 shows that the trajectory obtained with the modified AZ-733V file with irregular sampling intervals and inaccurate sampling rate resembles the trajectory obtained with the modified GateCT file under the same conditions.

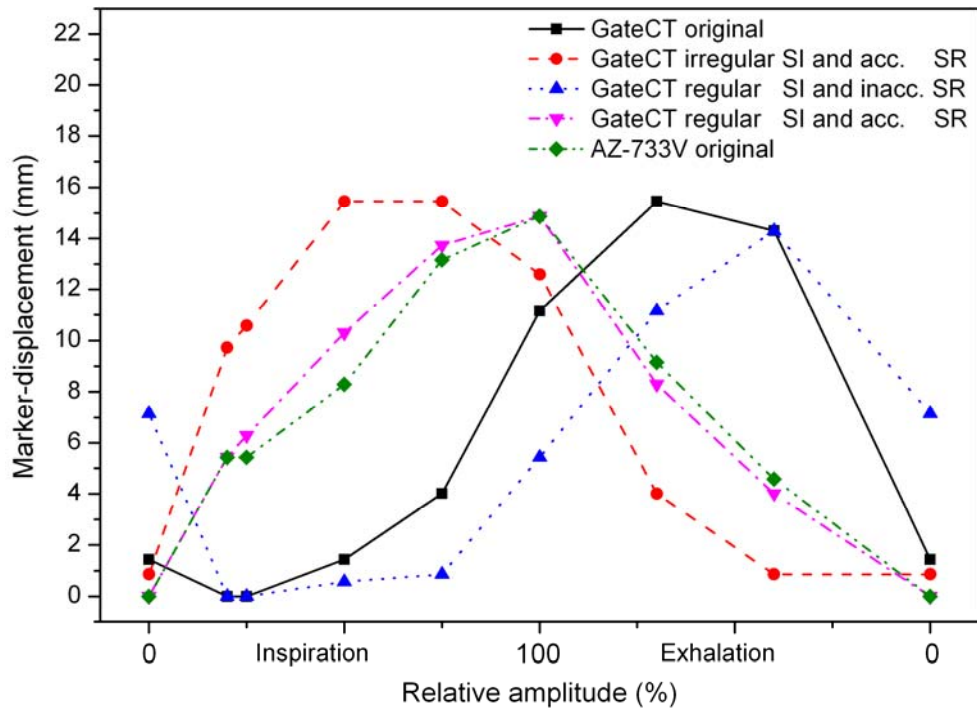


**Figure 4.16:** Influence of regularity of sampling intervals and accuracy of sampling rate in the ASCII-header of the GateCT system.

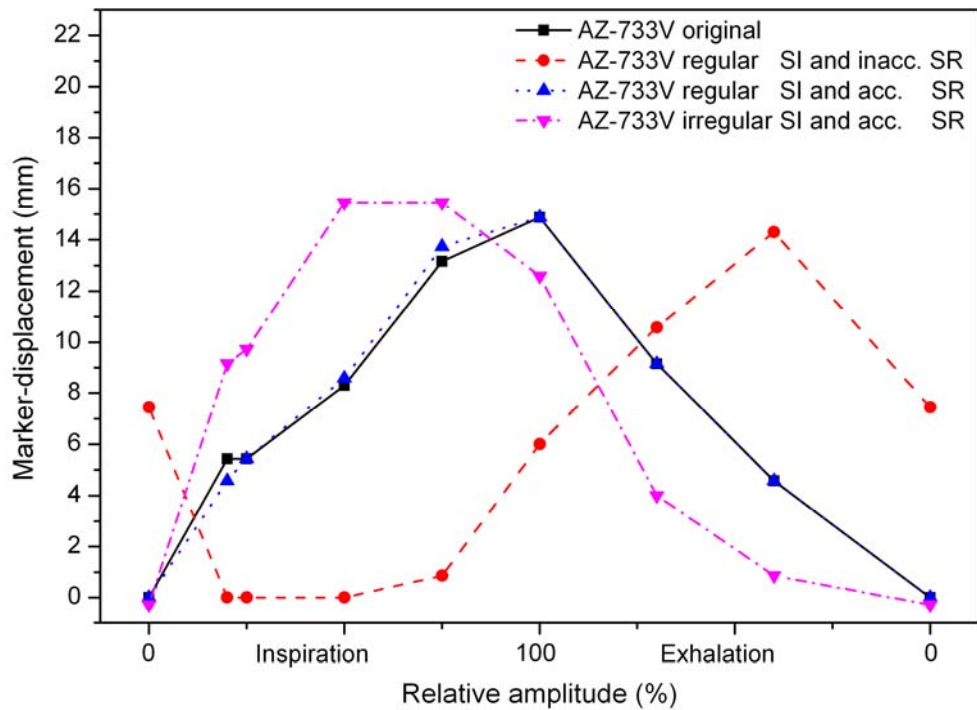


**Figure 4.17:** Influence of regularity of sampling intervals and accuracy of sampling rate in the ASCII-header of the AZ-733V system.

The corresponding CT-images also reflected the distortion encountered in the fiducial marker trajectories and some presented heavy artefacts. This was clearly visible when observing those images in a sagittal view with lung window (figure 4.18).

Some images presented a deformed tumour shape, where others presented a spherical tumour closer to reality, but still with shadows that did not belong to the phantom. The only image-sets free of artefacts were those that used the following files to reconstruct the 4D-CTs:

- 1) the original AZ-733V-curve (figure 4.18a),
- 2) the GateCT-curve with a interpolated regular sampling intervals and an accurate sampling rate in the ASCII-header (figure 4.18e),
- 3) and the GateCT-curve with all modifications mentioned from **i** to **v**) (figure 4.18f).

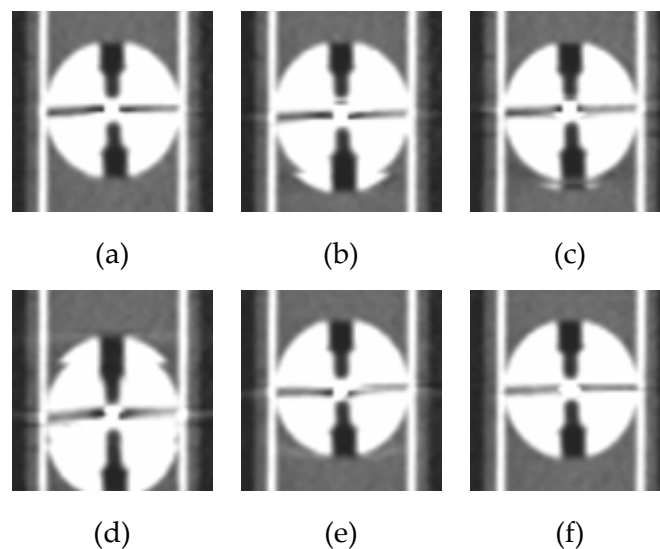


**Figure 4.18:** Reconstructed sagittal image through the centre of the tumour (lung window) at 0% exhalation for the original AZ-733V-curve (a), original GateCT-curve (b), smoothed GateCT-curve (c), AZ-733V-curve with irregular sampling intervals and inaccurate sampling rate in the ASCII-header (d), GateCT-curve interpolated to regular sampling intervals and with correct sampling rate in the ASCII-header (e) and the GateCT-curve with all improvement mentioned from **i** to **v**) (f). Images (a), (e) and (f) present the best image quality for all reconstructed percentage amplitudes. To avoid manipulations, the actual picture size is shown.

Finally, following subsection 4.1.6.2 vi), the results in figure 4.19 shows that different sampling rates do not significantly influence the trajectory of the marker observed in the 4DCTs. Lastly, this fact confirms that, as long as the sampling rate remains regular and complies with the sampling rate written on the ASCII-header, 4D-CTs reconstructions made with the GateCT can provide accurate information on moving targets, regardless if a higher (15.00 Hz) or lower (12.17 Hz) value was used.

This graph also shows that the reconstructed trajectory of the marker still differs somewhat from the ground truth (or ideal) reconstructed trajectory. In the case of the inspiration part, all the measured fiducial positions were systematically above this line, and for the exhalation part they were located below. Nevertheless for all the different sampling rates, the reconstructed trajectories agreed with the ideal trajectory within  $\pm 3.0$  mm, as seen in figure 4.20.

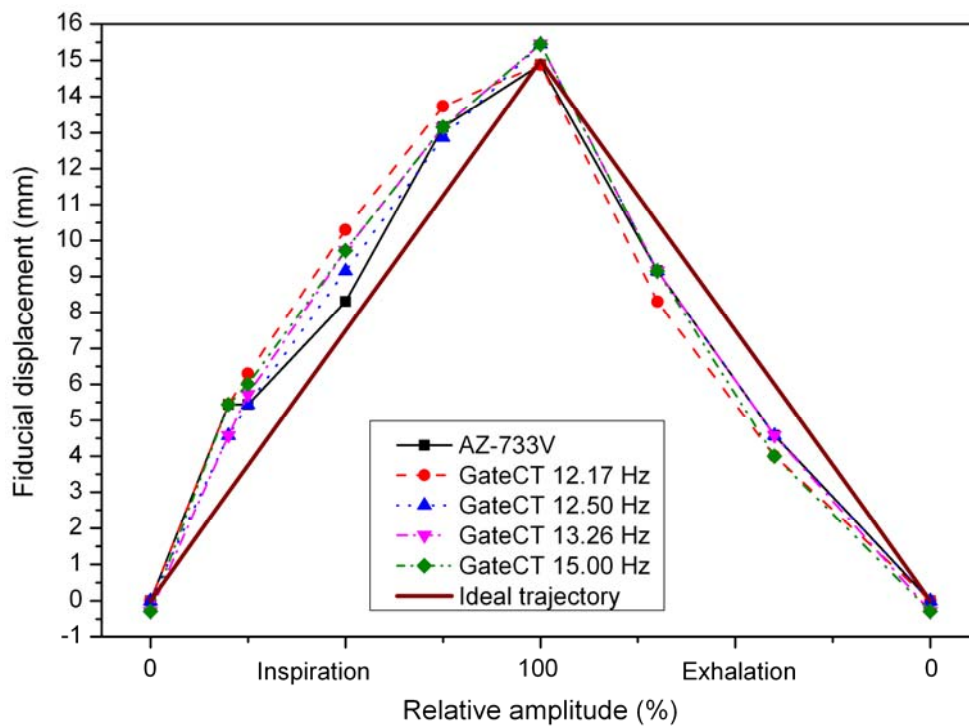


**Figure 4.19:** No significant influence on the fiducial trajectory was found when the value of the sampling rate was modified from 12.17 to 15.00 Hz. A systematic shift from the ideal trajectory is seen in the inspiration and exhalation parts.

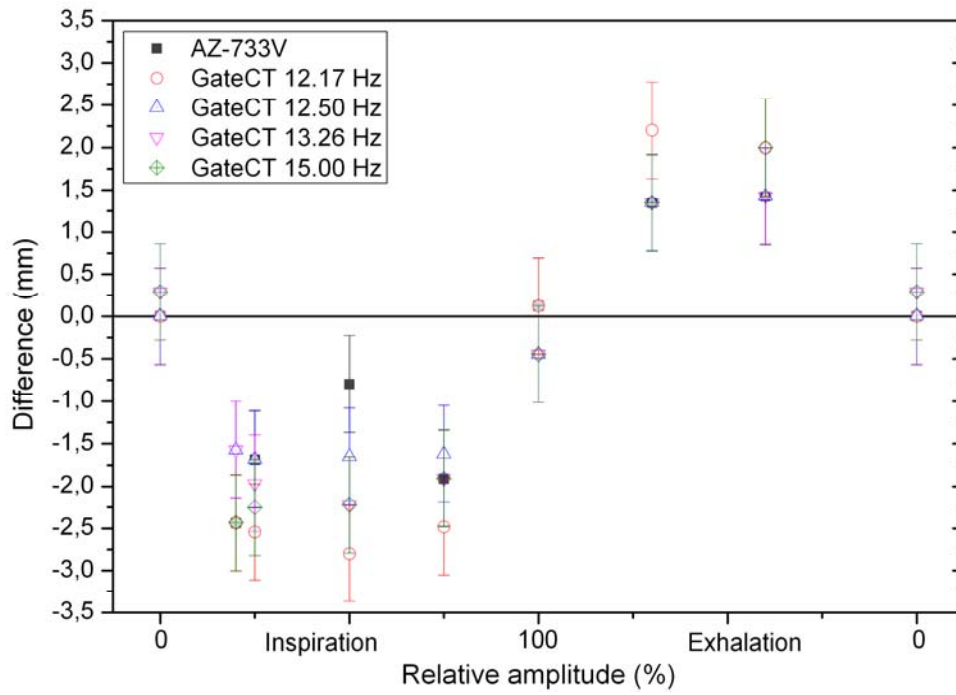


**Figure 4.20:** The deviation of each reconstructed centroid position of the fiducial marker to the ideal trajectory position was always less than 3 mm.

## *Discussion*

### **5.1 Comparison of external breathing monitoring systems**

In this study, we compared two external breathing monitoring systems (EBMS): the pressure sensor AZ-733V and the surface imaging system GateCT. These systems show contrasting results. On the one hand they register the respiration events synchronously but the curve shape differs. The AZ-733V signal depends heavily on how tight the belt is fastened and over which anatomical structure the pressure-sensor is located. This makes reproducibility difficult to achieve.

As for the tagging process, the GateCT system excels due to the reprocessing routine, which gives it a clear advantage over the AZ-733V, which does not have this feature. The tagging precision results obtained in this work agreed with those found by (Otani et al. 2010) in their investigation of tagging for the AZ-733V and RPM systems with patients. In their case, tagging was a quite important parameter given that their reconstruction CT algorithm and gating method was phase-rather than amplitude-based. They concluded that one should be consistent and only use one EBMS through imaging and treatment. This should be taken into account for future studies.

### **5.2 Phantom capabilities**

To test both EBMSs a new anthropomorphic breathing phantom was developed and tested. The high precision showed that reproducing both a periodic curve as well as the thorax displacement of a volunteer opens the door to imitating patient breathing curves. Given the tissue-equivalence of the phantom materials and the possibility of inserting ionization chambers and/or films into the phantom, it additionally offers the possibility to study the uncertainty in the dose delivery when moving targets are present. The phantom may be used for commissioning of motion compensated treatment techniques (Dieterich et al 2008) as well as for quality assurance tests for lung and breast cancer cases. The slight loss of air must be taken into account if longer breathing curves are

planned to be reproduced. The phantom was already tested for leaks and as none was found the easiest way to fix the loss would be by compensating it through the software controlling the phantom.

### **5.3 Testing GateCT for use in 4D-CT imaging**

Removal of motion artefacts in the CT image, when the GateCT signal was used to produce a 4D-CT, confirms the feasibility of this system for 4D-CT acquisitions. Further studies using a regular and periodical curve showed a high regularity of the period of tags with values agreeing well with the predefined period, if the limited sampling rate is taken into account.

### **5.4 Comparison of 4D-CT reconstructions**

The peaks tagging process and the X-ray On signal detection is excellent for both systems. As expected the extended valley plateau in the curve between peaks provoked some difficulties for the tagging of valleys in both systems, but it is not clear why the AZ-733V and GateCT valley tags were systematically located before and after the nominal valley tag, respectively. For the AZ-733V, it is possible that the implemented predictive algorithm establishes that an extreme value has been reached, when no amplitude change is detected after some time interval (smaller than the length of the plateau). This behaviour is also registered in the tagging precision values obtained from the volunteer. For the GateCT system, the presence of the baseline drift (result of the change of CT-couch inclination) may cause the minimum to be tagged at a later time than the nominal valley tag.

Looking into the stability of the sampling intervals, a clear difference between both systems was found. The AZ-733V measures continuously at a fix interval whereas the sampling intervals of the GateCT show large variation within and between measurements. Adding the inaccurate sampling rate value written in the GateCT file-header, probably produced by a rounding error of the GateCT software, and the unexpected result that although the breathing curves from both systems were very similar, the reconstructed fiducial marker trajectories of both systems differed significantly.. These differences were the motivation to study the influence of the different parameters of the EBMS on the 4D-CT images.

Baseline drift correction did not bring any significant improvement, probably because the amplitude-based sorting algorithm is not affected by it. By evaluating each breathing cycle locally the accumulated signal drift is diminished. The improvement of valley tagging did not have an effect either, but this was somehow expected as the local amplitude-based algorithm only uses the tags for splitting the curve into different breathing cycles. We already had highly precise peak tags and in spite of the fact that the valley tags were inaccurately located, the improvement only moved them in a section of the curve which varies quite slowly and therefore 0% amplitude selected by the CT was more or less always the same.

Noise removal however did have an effect, but only in the lowest percentage amplitude investigated (0% inspiration). This could be explained as follows: to form the image set at the lowest percentage amplitude, only the projections around the lowest point at each breathing cycle should be selected. Noise (especially in a flat region) can produce a “new” lowest point and therefore projections which do not correspond are used for image formation. By removing the noise a better correlation between the signal and the tumour motion is obtained, given that at those moments (0% inspiration) the tumour remains static and therefore the surrogate signal should also remain constant.

In this work, it was also shown that the differences in the reconstructed fiducial trajectory critically depends on the regularity of the sampling points as well as the accurate specification of the sampling rate in the header, rather than on differences in the shape of the breathing curve itself. This was confirmed by repeated reconstructions after the following procedures were done: first, correcting the GateCT-curves to regular sampling rates and an accurate sampling rate in the file header, second by distorting the respective parameters for the AZ-733V-curve, and last by studying the occurrence of image artefacts for these cases. Only images created with the original AZ-733V-curve and with the corrected GateCT-curve had a minimal amount of image artefacts. These tests showed consistently that the irregular sampling rate and the approximated sampling rate in the file header of the GateCT-system are responsible for the deviation from the AZ-733V system. Furthermore it was shown that the sampling rate magnitude did not have a significant impact on the marker trajectory.

As seen in figure 4.19, the reconstructed trajectories still differed from the predefined trajectory. This is due to partial projection artefacts caused by residual motion and tumour velocity changes during the CT-acquisition as explained by other authors. Rietzel et al. (2005) discussed that partial

projection artefacts, were a source of error in tumour localization. Later Nakamura et al. (2009) proved that the residual movements of the tumour were causing these artefacts and Lewis and Jiang (2009) showed that also the direction of tumour motion affects the mean tumour position in normal spiral CT under free breathing conditions. This effect is still visible even when the 4D-CT technique is used, due to the finite time required for the acquisition of the projections, which in our case is half a rotation time plus fan beam angle, meaning 333 ms. Finally Watkins et al. (2010) demonstrated that shorter rotation times will decrease this effect further. Altogether, the deviations of the best trajectories from the ideal trajectory were always smaller than one slice thickness ( $\pm 3.0$  mm), which can be regarded as the spatial resolution of the CT in the Z-direction. Therefore the 4D-CTs made with the mentioned EBMS signals delivered accurate reconstructions within the CT capabilities.

This work leads to four important conclusions:

- 1) The applied reconstruction algorithm of the used Siemens CT critically depends on parameters which are not visible in the shape of the breathing curve, but which are related to its data representation. Manipulations **iv)** and **v)** applied to both original AZ-733V and GateCT files clearly point out that the CT requires that the imported data from the breathing curves must be written with a fixed sampling rate.
- 2) Although the specification of the interface is not open to the user, there is an obvious discrepancy between expected and actually provided time stamps, which is detected neither by the CT nor by the GateCT-system.
- 3) This underlines the importance of commissioning tests prior to clinical application. For this reason, tools like the developed phantom have to be available to make simultaneous measurements. However, comparison of breathing curves alone would not have led to the discovery of the observed effect, and therefore the complete chain from data acquisition to image reconstruction and quantitative evaluation has to be investigated.
- 4) More generally, application of medical products from different manufacturers requires critical testing of their respective interface. The developed phantom can be used for this application applying the special feature that two breathing monitoring systems can be simultaneously operated.

It has to be noted that the findings are related to the combined application of GateCT with a Siemens-CT. As the observed effects probably are specific for the CT-interface, application with CTs from other manufacturers may reveal different results.

The actual reason for the irregular sampling rate of the GateCT-system is not clear. A potential reason could be limited hard- or software capabilities. In spite of the variation of the sampling intervals, however, correct time stamps were assigned to each surface image (and hence to each data point of the breathing curve), otherwise, the resulting breathing curve would not have agreed with the AZ-733V-curve.

The described problems might be solved either by a faster hardware or alternatively by interpolating the breathing curve to a regular sampling rate and by correcting the sampling rate in the header file. These findings were acknowledged by the manufacturer VisionRT and as a consequence, a revised version of the GateCT-software will be released. In this release, the breathing curve will be resampled using a fixed and regular sampling rate, which will be correctly reported in the header file (personal communication 04.06.2011, Martin Allen, VisionRT Ltd, London, UK).

## **5.5 Clinical implications**

Under the condition that the GateCT-measurement is performed with regular sampling intervals and that the sampling rate in the header file is accurate, the resulting fiducial trajectory agrees with that of the AZ-733V-system and they can be regarded to produce equivalent results. Therefore the selection of one or the other system in clinical practice may then be based on practical considerations, such as reliability, operability workflow, patient comfort and any extra features offered. The VisionRT system is especially interesting in this matter due its non-invasiveness and due to the fact that its platform also includes products for patient positioning and linear accelerator gating.

The use of the 4D-CT technique allows reducing the influence of tumour motion on the CT-reconstruction, i.e. it reduces image artefacts and improves tumour localisation accuracy. Nevertheless a residual motion of 3 mm (for the given slice thickness of 3 mm) was found and this uncertainty must be incorporated into the treatment planning process. As lung tumour motion

may exhibit peak-to-peak amplitudes of up to 50 mm (Chen et al 2001), the use of 4D-CTs may still significantly improve image quality and tumour localization.. In the simplest case, this information may be used for a proper definition of the target volume. In addition, more advanced motion compensation techniques such as gating or tracking (Kubo and Hill 1996, Tacke et al 2010) may be applied. While the first approach ensures only coverage of the target, the latter would significantly reduce the irradiated normal tissue volume, which would then allow either the reduction of normal tissue complications probability or the increase of prescribed dose.

## *Concluding remarks*

### **6.1 Summary**

4D-CTs using two different external breathing monitoring systems were compared with help of a newly developed breathing phantom. Differences found in the reconstructed 4D-CT resulted from a discrepancy in how the breathing information is interpreted by the CT. When this discrepancy was resolved, the 4D-CTs reconstructed with both respiration monitoring systems agreed well and the selection of one or the other system for 4D-CT-imaging may then be based on extra features offered. For the used CT-slice thickness of 3 mm, a comparison with the predefined trajectory revealed a residual uncertainty of up to 3 mm. This uncertainty has to be considered in the definition of the target volume. The results of this study underline the importance of testing new equipment thoroughly, especially if components of different manufacturers are combined. Using the newly developed phantom, clinical workflows can be tested and the functioning of the applied medical devices can be ensured.

### **6.2 Outlook**

This study shows that the phantom allows testing different settings used today in 4D-imaging and treatment planning. The optical camera system is an interesting new platform for the monitoring of breathing motion in imaging and radiotherapy delivery with promising perspectives, due to its capability to be used also as a positioning and a gating system with the identical hardware. Two studies, detailed in the next paragraphs, are suggested to be performed in the near future.

### **6.2.1 Gating a linear accelerator**

Now that the phantom can successfully imitate human breathing, the possibility of testing a gated treatment at a linear accelerator (linac) can be investigated. The phantom can reproduce both patient's surface motions as well as the lung tumour motion in cranio-caudal direction. A breathing curve for the surface could be obtained using the VisionRT system installed at a linac and the tumour information could be obtained through fluoroscopy. To avoid extra radiation dose to the patient, the fluoroscopic information should be limited to the field of view of the therapeutic beam and it should be recorded by an in-line electronic portal imaging device (EPID). In the next step, these two trajectories could be fed to the phantom and a treatment plan could be delivered. In this way the accumulated dose and geometrical distribution could be recorded by ICs or films (or both). Now this process could be repeated, this time using the GateRT system to gate the linac based on the surface displacement. Therefore, different gating windows could be investigated with phantom's measurements. Gating could also be tested for the case of breast tumours. A quantification of dose reduction to the organs at risk using this method and the moving phantom is feasible.

### **6.2.2 Correlation of external breathing monitoring systems and tumour motion**

Correlation studies between the external chest/abdomen motion and the internal tumour displacement could be performed using the stereoscopic camera system. In this work, it was shown that the VisionRT system can perfectly follow the displacement of a moving surface. This feature could be used to monitor patients under treatment delivery without extra imaging dose. Then the breathing curve from this measurement could be compared with the tumour motion (obtained through fluoroscopy). The same could be done with the AZ-733V system as external signal. Then the decision of gating (or tracking) treatments for patients with help of one or the other external breathing monitoring system could be taken.

# Bibliography

- Balter, J M, R K Ten Haken, T S Lawrence, K L Lam, and J M Robertson. 1996. "Uncertainties in CT-based radiation therapy treatment planning associated with patient breathing." *International journal of radiation oncology, biology, physics* **36**: 167-174.
- Bracewell, R N. 1956. "Strip integration in radio astronomy." *Australian journal of physics* **9**: 198-217.
- Berbeco, R I, S Nishioka, H Shirato, G T Y Chen, and S B Jiang. 2005. "Residual motion of lung tumours in gated radiotherapy with external respiratory surrogates." *Physics in medicine and biology* **50**: 3655-3667.
- Berson, A M, R Emery, L Rodriguez, G M Richards, T Ng, S Sanghavi, and J Barsa. 2004. "Clinical experience using respiratory gated radiation therapy: comparison of free-breathing and breath-hold techniques." *International journal of radiation oncology, biology, physics* **60**: 419-426.
- Bert, C, K G. Metheany, K Doppke, and G T. Y. Chen. 2005. "A phantom evaluation of a stereovision surface imaging system for radiotherapy patient setup." *Medical Physics* **32**: 2753-2762.
- Bert, C, N Saito, A Schmidt, N Chaudhri, D Schardt, and E Rietzel. 2007. "Target motion tracking with a scanned particle beam." *Medical Physics* **34**: 4768-4771.
- Bortfeld, T, S B Jiang, and E Rietzel. 2004. "Effects of motion on the total dose distribution." *Seminars in radiation oncology* **14**: 41-51.
- Chen Q S, M S Weinhaus, F C Deibel, J P Ciezki, and R M Macklis. 2001. "Fluoroscopic study of tumor motion due to breathing: Facilitating precise radiation therapy for lung cancer patients." *Medical Physics* **28**: 1850-1856
- Court, L E, X Lu, D Ionascu, B Winey, N Giakoumakis, M Aristophanous, R Berbeco, J Rottman, M Bogdanov, D Schofield, and T Lingos. 2010. "Use of a realistic breathing lung phantom to evaluate dose delivery errors." *Medical Physics* **37**: 5850-5857.
- Dieterich S, K Clearly, W D D'Souza, M Murphy, K H Wong and P Keall. 2008 "Locating and targeting moving tumors with radiation beams." *Medical Physics* **35**: 5684-5694.
- D'Souza, W D, Y Kwok, C Deyoung, N Zacharopoulos, M Pepelea, P Klahr, and C X Yu. 2005. "Gated CT imaging using a free-breathing respiration signal from flow-volume spirometry." *Medical Physics* **32**: 3641-3649.
- Feldkamp L A, Davis L C and Kress J W 1984 "Practical cone-beam algorithm" *Journal of the Optical Society of America A* **1** 612-619.
- Ferlay J, HR Shin, F Bray, D Forman, C Mathers and DM Parkin. "GLOBOCAN 2008 v1.2, Cancer Incidence and Mortality Worldwide: IARC CancerBase No. 10". Lyon, France: International Agency for Research on Cancer; 2010. <http://globocan.iarc.fr>, accessed on 02/08/2011.

- Ford, E C, G S Mageras, E Yorke, K E Rosenzweig, R Wagman, and C C Ling. 2002. "Evaluation of respiratory movement during gated radiotherapy using film and electronic portal imaging." *International journal of radiation oncology, biology, physics* **52**: 522-531.
- Ford, E C, G S Mageras, E Yorke, and C C Ling. 2003. "Respiration-correlated spiral CT: A method of measuring respiratory-induced anatomic motion for radiation treatment planning." *Medical Physics* **30**: 88-97.
- George, R, S S Vedam, T D Chung, V Ramakrishnan, and P J Keall. 2005. "The application of the sinusoidal model to lung cancer patient respiratory motion." *Medical Physics* **32**: 2850-2861.
- Glide-Hurst, C K, D Ionascu, R Berbeco, and D Yan. 2011. "Coupling surface cameras with on-board fluoroscopy: A feasibility study." *Medical Physics* **38**: 2937-2947.
- Guckenberger, M, M Weininger, J Wilbert, A Richter, K Baier, T Krieger, B Polat, and M Flentje. 2007. "Influence of retrospective sorting on image quality in respiratory correlated computed tomography." *Radiotherapy and oncology* **85**: 223-231.
- Hoisak, J D P, K E Sixel, R Tirona, P C F Cheung, and J-P Pignol. 2004. "Correlation of lung tumor motion with external surrogate indicators of respiration." *International journal of radiation oncology, biology, physics* **60**: 1298-1306.
- ICRU Report 62. Prescribing, Recording and Reporting Photon Beam Therapy (Supplement to ICRU Report 50) 1999 *International Commission on Radiation Units and Measurements*, Bethesda, MD.
- Kachelriess (a), M, S Schaller, and W A Kalender. 2000. "Advanced single-slice rebinning in cone-beam spiral CT." *Medical physics* **27**: 754-772.
- Kachelriess (b), M, S Ulzheimer, and W A Kalender. 2000. "ECG-correlated image reconstruction from subsecond multi-slice spiral CT scans of the heart." *Medical physics* **27**: 1881-1902.
- Kalender, W A. 2005 'Mathematical aspects of image reconstruction', *Computed Tomography* 2nd edn, Publicis Corporate Publishing, 245-268, Erlangen
- Kalender, W A. 2006. "X-ray computed tomography." *Physics in medicine and biology* **51**: R29-R43.
- Keall, P J, G Starkschall, H Shukla, K M Forster, V Ortiz, C W Stevens, S S Vedam, R George, T Guerrero, and R Mohan. 2004. "Acquiring 4D thoracic CT scans using a multislice helical method." *Physics in Medicine and Biology* **49**: 2053-2067.
- Keall, P J, G S Mageras, J M. Balter, R S Emery, K M Forster, S B Jiang, J M Kapatoes, D A Low, M J, B R Murray, C R Ramsey, M B Van Herk, S S Vedam, J W Wong, and E Yorke. 2006. "The management of respiratory motion in radiation oncology report of AAPM Task Group 76." *Medical Physics* **33**: 3874-3900.
- Korreman, S S, A N Pedersen, T J Nøttrup, L Specht, and H Nyström. 2005. "Breathing adapted radiotherapy for breast cancer: comparison of free breathing gating with the breath-hold technique." *Radiotherapy and oncology* **76**: 311-318.

- Korreman, S S, A N Pedersen, L R Aarup, T J Nøttrup, L Specht, and H Nyström. 2006. "Reduction of cardiac and pulmonary complication probabilities after breathing adapted radiotherapy for breast cancer." *International journal of radiation oncology, biology, physics* **65**: 1375-1380.
- Kubo, H D, and B C Hill. 1996. "Respiration gated radiotherapy treatment: a technical study." *Physics in medicine and biology* **41**: 83-91.
- Lagerwaard, F J, J R Van Sornsen de Koste, M R Nijssen-Visser, R H Schuchhard-Schipper, S S Oei, a Munne, and S Senan. 2001. "Multiple 'slow' CT scans for incorporating lung tumor mobility in radiotherapy planning." *International journal of radiation oncology, biology, physics* **51**: 932-937.
- Lewis, J H, and S B Jiang. 2009. "A theoretical model for respiratory motion artifacts in free-breathing CT scans." *Physics in medicine and biology* **54**: 745-755.
- Li, T, E Schreibmann, B Thorndyke, G Tillman, A Boyer, A Koong, K Goodman, and L Xing. 2005. "Radiation dose reduction in four-dimensional computed tomography." *Medical Physics* **32**: 3650-3660.
- Low, D A, M Nystrom, E Kalinin, P Parikh, J F Dempsey, J D Bradley, S Mutic, S H Wahab, T Islam, G Christensen, D G Polite and B R Whiting. 2003. "A method for the reconstruction of four-dimensional synchronized CT scans acquired during free breathing." *Medical Physics* **30**: 1254-1263.
- Lu, W, P J Parikh, J P Hubenschmidt, J D Bradley, and D A Low. 2006. "A comparison between amplitude sorting and phase-angle sorting using external respiratory measurement for 4D CT." *Medical Physics* **33**: 2964-2974.
- Lujan A, E W Larsen, J M Balter, and R K T Haken 1999. " A method for incorporating organ motion due to breathing into 3D dose calculations" *Medical Physics* **26**: 715-720.
- Malinowski K, C Noel, W Lu, K Lechleiter, J Hubenschmidt, D Low and P Parikh 2007 "Development of the 4D phantom for patient-specific end-to-end radiation therapy QA." *Proceedings SPIE* **6510** 65100E.
- Martisíková, M, B Ackermann, and O Jäkel. 2008. "Analysis of uncertainties in Gafchromic EBT film dosimetry of photon beams." *Physics in medicine and biology* **53**: 7013-7027.
- Murphy, M J 2004. "Tracking moving organs in real time." *Seminars in radiation oncology* **14**: 91-100.
- Nakamura, M, Y Narita, A Sawada, K Matsugi, M Nakata, Y Matsuo, T Mizowaki, and M Hiraoka. 2009. "Impact of motion velocity on four-dimensional target volumes: A phantom study." *Medical Physics* **36**: 1610-1617.
- Nioutsikou, E, J Richard N Symonds-Taylor, J L Bedford, and S Webb. 2006. "Quantifying the effect of respiratory motion on lung tumour dosimetry with the aid of a breathing phantom with deforming lungs." *Physics in medicine and biology* **51**: 3359-3374.
- Otani, Y, I Fukuda, N Tsukamoto, Y Kumazaki, H Sekine, E Imabayashi, O Kawaguchi, T Nose, T Teshima, and T Dokiya. 2010. "A comparison of the respiratory signals acquired by different respiratory" *Medical Physics* **37**: 6178-6186.

- Radon J 1917, "Über die Bestimmung von Funktionen durch ihre Integralwerte längs gewisser Mannigfaltigkeiten", *Berichte Sächsische Akademie der Wissenschaft* **69**: 262-277.
- Rau, A W, S Nill, R S Eidens, and U Oelfke. 2008. "Synchronized tumour tracking with electromagnetic transponders and kV x-ray imaging: evaluation based on a thorax phantom." *Physics in medicine and biology* **53**: 3789-3805.
- Rietzel, E, T Pan, and G T. Y. Chen. 2005. "Four-dimensional computed tomography: Image formation and clinical protocol." *Medical Physics* **32**: 874-889.
- Schöffel, P J, W Harms, G Sroka-Perez, W Schlegel, and C P Karger. 2007. "Accuracy of a commercial optical 3D surface imaging system for realignment of patients for radiotherapy of the thorax." *Physics in medicine and biology* **52**: 3949-3963.
- Seppenwoolde, Y, H Shirato, K Kitamura, S Shimizu, M van Herk, J V Lebesque, and K Miyasaka. 2002. "Precise and real-time measurement of 3D tumor motion in lung due to breathing and heartbeat, measured during radiotherapy." *International journal of radiation oncology, biology, physics* **53**: 822-834.
- Serban, M, E Heath, G Stroian, D L Collins, and J Seuntjens. 2008. "A deformable phantom for 4D radiotherapy verification: Design and image registration evaluation." *Medical Physics* **35**: 1094-1102.
- Siebert, J P, and S J Marshall. 2000. "Human body 3D imaging by speckle texture projection photogrammetry." *Sensor Review* **20**: 218-226.
- Sixel, K E, M C Aznar, and Y C Ung. 2001. "Deep inspiration breath hold to reduce irradiated heart volume in breast cancer patients." *International journal of radiation oncology, biology, physics* **49**: 199-204.
- Sjödahl M and P Synnergren, "Measurement of shape by using projected random patterns and temporal digital speckle photography," 1999 *Applied Optics* **38**: 1990-1997.
- Szegedi, M, P Rassiah-Szegedi, G Fullerton, B Wang, and B Salter. 2010. "A proto-type design of a real-tissue phantom for the validation of deformation algorithms and 4D dose calculations." *Physics in medicine and biology* **55**: 3685-3699.
- Tacke, M B., S Nill, A Krauss, and U Oelfke. 2010. "Real-time tumor tracking: Automatic compensation of target motion using the Siemens 160 MLC." *Medical Physics* **37**: 753-761.
- United Nations Department of Economic and Social Affairs, Population Division 2010. "World population aging 2009". ISBN 978-92-1-151468-1, Sales No. E.10.XIII.5.
- Vedam, S S, P J Keall, V R Kini, H Mostafavi, H P Shukla, and R Mohan. 2003. "Acquiring a four-dimensional computed tomography dataset using an external respiratory signal." *Physics in medicine and biology* **48**: 45-62.
- Vedam, S S, P J Keall, V R Kini, and R Mohan. 2001. "Determining parameters for respiration-gated radiotherapy." *Medical Physics* **28**: 2139-2146.

- Vinogradskiy, Y Y, P Balter, D S Followill, P E Alvarez, R A White, and G Starkschall. 2009. "Verification of four-dimensional photon dose calculations." *Medical Physics* **36**: 3438-3447.
- Watkins, W T, R Li, J Lewis, J C Park, A Sandhu, S B Jiang, and W Y Song. 2010. "Patient-specific motion artifacts in 4DCT." *Medical Physics* **37**: 2855-2861.
- Wink, N M, M F McNitt-Gray, and T D Solberg. 2005. "Optimization of multi-slice helical respiration-correlated CT: the effects of table speed and rotation time." *Physics in medicine and biology* **50**: 5717-5729.
- Wolthaus, J W H, M van Herk, S H Muller, J S A Belderbos, J V Lebesque, J A de Bois, M M G Rossi, and E M F Damen. 2005. "Fusion of respiration-correlated PET and CT scans: correlated lung tumour motion in anatomical and functional scans." *Physics in medicine and biology* **50**: 1569-1583.
- Wong, K H, S Dieterich, J Tang, and K Cleary. 2007. "Quantitative measurement of CyberKnife robotic arm steering." *Technology in cancer research and treatment* **6**: 589-594.

# List of figures

1.1	World incidence and mortality of cancer cases .....	1
1.2	World fertility rate and life expectancy .....	2
1.3	Lungs scheme .....	3
1.4	Lung tumour motion .....	4
1.5	X-ray attenuation .....	7
1.6	Tomographic principle .....	8
1.7	CT visualization planes .....	11
1.8	4D-CT image set formation .....	16
2.1	AZ-733V: Hardware components .....	20
2.2	AZ-733V: Wave-Deck signals' adapter .....	20
2.3	AZ-733V: Software view .....	21
2.4	GateCT: CT-room view of VisionRT cameras .....	23
2.5	GateCT: Schematic view of the stereoscopic principle .....	23
2.6	GateCT: Speckle pattern and calibration plate .....	24
2.7	GateCT: Detailed view of VisionRT hardware .....	25
2.8	GateCT: Movement during CT .....	26
2.9	GateCT: Software view .....	26
2.10	GateCT: Operation workflow .....	27
2.11	GateCT: Geiger-Müller detector .....	27
2.12	Data format: GateCT/Varian .....	28
2.13	Data format: AZ-733V .....	30
2.14	Comparison of EBMS signals obtained from a volunteer .....	33
3.1	Phantom: On couch .....	36
3.2	Phantom: Schematic and CT-view .....	37
3.3	Motors: Schematic view .....	38
3.4	Motors: Detailed photos .....	39
3.5	Software: Synchronization protocol .....	41
3.6	Location of ionization chambers in lung tumour .....	43
3.7	Phantom calibration curve .....	44
3.8	Breathing reproduced by phantom .....	45

3.9	Pearson's calculations .....	45
3.10	Amplitude difference of reproduced motion .....	45
4.1	CT-console view .....	47
4.2	Definition of peak and valley periods .....	49
4.3	Setup of couch inclination test .....	51
4.4	Fiducial marker .....	53
4.5	Tumour images with and without motion compensation .....	57
4.6	Comparing EBMS signals using a cosine-like curve .....	59
4.7	EBMS signals during CT-acquisition .....	60
4.8	AZ-733V and RPM sampling interval histograms .....	62
4.9	GateCT sampling interval histograms .....	63
4.10	Couch inclination test results .....	64
4.11	Comparison of fiducial trajectory using original EBMS signals .....	65
4.12	Lung tumour images with original EBMS signals .....	66
4.13	GateCT baseline drift corrected signal .....	66
4.14	GateCT noise reduced signal .....	67
4.15	Influence of modification i) to iii) on fiducial trajectory .....	68
4.16	Influence of modifications iv) and v) on fiducial trajectory for GateCT .....	69
4.17	Influence of modifications iv) and v) on fiducial trajectory for AZ-733V .....	69
4.18	Tumour images using different EBMS signals .....	70
4.19	Influence of sampling rate magnitude on fiducial trajectory .....	71
4.20	Deviations from ideal fiducial trajectory .....	72

# List of tables

1.1	CT values definition for bone and lung windows .....	11
2.1	Tagging precision of two EBMS signals obtained from a volunteer .....	32
3.1	CT values of phantom's materials .....	37
4.1	Summary of CT-scans to prove feasibility of the GateCT for 4D-CT .....	48
4.2	CT protocols' parameters .....	48
4.3	Phantom's breathing regular motion parameters .....	49
4.4	Summary of modifications iv) and v) made to the GateCT signal .....	56
4.5	Summary of modifications iv) and v) made to the AZ-733V signal .....	56
4.6	Fixed sampling rate values and intervals used for modification vi) .....	57
4.7	Temporal peak detection difference between EBMSs .....	60
4.8	Peak-valley tag periods and valley tagging precision for both EBMSs .....	61
4.9	GateCT mean sampling intervals and rates together with the header nominal sampling value .....	64
4.10	GateCT valley tagging precision, before and after correction .....	67

# Acknowledgements

During this period of my life, several persons and institutions have provided me with their help, knowledge and financial support and I will like to write a couple of lines to thank them properly.

First I would like to start thanking my supervisor Prof. Christian Karger for offering me the opportunity to work with his group and on this project. His guidance, constructive discussions and availability for every question were greatly appreciated. Also I want to thanks Prof. Wolfgang Schlegel for his support, advice and the great work ambient created by him as Head of the Department. To Prof. Uwe Oelfke I am greatly thankful for kindly accepting to be my first referee for my dissertation and to Prof. Oliver Jäkel and his group for supporting me the first month of my arrival to the DKFZ. All these people played a major role in my decision to pursuit a PhD in medical physics, as the idea was born, when I visited a summer course, which took place in Santiago de Chile in 2007.

Thank you to my current and former office partners: Paola, Ignacio, Pamela, Christine, Sonja, Torsten, Martina, Sarah, Christin, Maria, Carine and Edgardo, for always presenting a friendly environment and for giving me more than one cheerful memory. I would also like to thanks Julia Lohead for proofreading this work.

I would also like to thank the clinical staff of the department of Radiology of the University Hospital of Heidelberg, especially Mrs. Schenk and the medical physicists' team. I am thankful for their help and kind cooperation in teaching me the know-how and how to use the equipments.

I want to acknowledge the Deutscher Akademischer Austausch Dienst (DAAD), as well as the Comisión Nacional de Investigación Científica y Tecnológica (CONICYT) for their financial support. I also acknowledge the cooperation and technical support by VisionRT Ltd., London, UK. I would like to add that equipment used in this work was partially funded by Siemens AG (Erlangen, Germany).

I will like to thanks Prof. Dirk Dubbers and Prof. Dieter Gromes for agreeing to be part of my examination committee.

And finally the most important support I ever had came from my parents, brothers and dearest friends. Reaching this point of my life would have been impossible without your love, care and encouragement. Padre mío, mamma, muchas gracias por todo el cariño y por guiarme en esta vida. ¡Los quiero mucho!